2010

Experimental Studies Of Liquefaction And Densification Of Liquid Oxygen

Jonathan Koert Partridge
University of Central Florida

EXPERIMENTAL STUDIES OF LIQUEFACTION AND DENSIFICATION OF LIQUID OXYGEN

by

JONATHAN KOERT PARTRIDGE
B.S. Tennessee Technological University, 2003

A thesis submitted in partial fulfillment of the requirements
for the degree of Master of Science in Mechanical Engineering
in the Department of Mechanical, Materials, and Aerospace Engineering
in the College of Engineering and Computer Science
at the University of Central Florida
Orlando, Florida

Fall Term
2010

ABSTRACT

Rocketry employs cryogenic refrigeration to increase the density of propellants, such as oxygen, and stores the propellant as a liquid. In addition to propellant liquefaction, cryogenic refrigeration can also conserve propellant and provide propellant subcooling and densification. Previous studies analyzed vapor conditioning of a cryogenic propellant, which occurred by either a heat exchanger positioned in the vapor or by using the vapor as the working fluid in a refrigeration cycle. This study analyzes the refrigeration effects of a heat exchanger located beneath the vapor-liquid interface of liquid oxygen.

This study predicts the mass liquefaction rate and heat transfer coefficient for liquid oxygen using two different models, a Kinetic Theory Model and a Cold Plate Model, and compares both models to experimental data. The Kinetic Theory Model overestimated the liquefaction rate and heat transfer coefficient by five to six orders of magnitude, while the Cold Plate Model underestimated the liquefaction rate and heat transfer coefficient by one to two orders of magnitude. This study also suggested a model to predict the densification rate of liquid oxygen, while the system is maintained at constant pressure. The densification rate model is based on transient heat conduction analysis and provides reasonable results when compared to experimental data.

ACKNOWLEDGEMENTS

The author acknowledges Jeff Tuttle, Kevin Jumper, Brian Hunter, Matt Nugent, Walt Hatfield, Gary Wall, Jeff Wall, Mark Velasco, Phillip Dandreamatteo, Kevin "Bert" Cummings, Mike Guthrie, Bill Notardonato, and Wesley Johnson for their contributions to the design, operation, management, and consultation of IRAS data analysis and evaluation.

TABLE OF CONTENTS

LIST OF FIGURES

LIST OF TABLES

LIST OF ACRONYMS AND SYMBOLS

Acronyms

ARC	NASA – Ames Research Center
GN_2	Gaseous Nitrogen
GO_2	Gaseous Oxygen
IRAS	Integrated Refrigeration and Storage
KSC	NASA – Kennedy Space Center
LC	Launch Complex
LN_2	Liquid Nitrogen
LO_2	Liquid Oxygen
MAWP	Maximum Allowable Working Pressure
MRI	Magnetic Resonance Imaging
NASA	National Aeronautics and Space Administration
NASP	National Aerospace Plane
ZBO	Zero Boil-off

Equations

A	area (m^2)
	A_{CS} cross-sectional area of IRAS dewar (m^2)
	A_f surface area of a single fin (m^2)
	A_p corrected fin profile area – $A_p = L_c t$ (m^2)
	A_s surface of liquid in IRAS (m^2)
	A_t total surface area for a cylindrical finned heat exchanger (m^2)
a	ratio of overall speed to molecular characteristic velocity ( )
C	constant
	C_z constant for bubble velocity ( )
	C_D constant for flow through orifice ( )
c_p	specific heat capacity (J/kg·K)
D	diameter of tubing (m)
	D_n diameter of nozzle (m)
	D_d diameter of bubble at departure from nozzle (m)
	D(t) bubble radius as a function of time as the bubble rises to the surface (m)
f	friction factor ( )
f_b	bubble departure frequency (1/s)
Fo	Fourier number ( )
	Fo_0 Fourier number based on bubble departure diameter $Fo_0 = \frac{\alpha t}{D_d^2}$
G	mass flux (kg/m²·s)
	G_{COND} conduction mass flux (kg/m²·s)
g	gravitational constant (m/s^2)
	g_c (32.2 $lb_m \cdot ft/lb_f \cdot s^2$)
Gr	Grashoff number ( )
H	height (m)
h	convection heat transfer coefficient (W/m²·K)
	h_{CC} condensation convection heat transfer coefficient (W/m²·K)
	h_{EC} external convection heat transfer coefficient (W/m²·K)
	h_{IC} internal convection heat transfer coefficient (W/m²·K)

h_{mic} microscopic convective coefficient due to nucleate boiling (W/m²·K)
h_{mac} macroscopic convective coefficient due to bulk convection (W/m²·K)

h_{lv} latent heat (J/kg)
h'_{lv} modified latent heat (J/kg)

Ja Jakob number defined by $Ja = \frac{\rho_l c_p (T_{sat} - T_l)}{\rho_v h_{lv}}$ ( )

k thermal conductivity (W/m·K)
k_l liquid thermal conductivity (W/m·K)
k_{PTFE} thermal conductivity of polytetrafluorethylene (W/m·K)
k_{SS} thermal conductivity of stainless steel (W/m·K)
k_v vapor thermal conductivity (W/m·K)

L length of tube (m)
L_c corrected length – $L_c = L + t/2$ (m)

M molecular weight (kg/mol)

m mass (kg)
$m_{b,cond}$ mass of bubble that condenses when rising through subcooled liquid (kg)

$\dot{m}$ mass flow rate (kg/s)
$\dot{m}_{b,cond}$ mass condensation rate of bubble rising through subcooled liquid (kg/s)
$\dot{m}_{GO_2}$ mass flow rate of gaseous oxygen entering IRAS dewar (kg/s)

N number of fins ( )

n integer for use in summation ( )

Nu_D Nusselt number ( )

q heat transfer rate (W)
q_r radial heat transfer rate (W)
q_t heat transfer rate (W)

P pressure (Pa = kg/m²)
P_c critical pressure (Pa)
P_g pressure of gas (Pa)
P_{sat} saturated pressure as a function of a given temperature (Pa)
P_{ref} reference pressure equivalent to 1,000,000 Pa (Pa)
P_t triple point pressure (Pa)
P_v vapor pressure as a function of temperature (Pa)

Pr	Prandtl number ( )
R	thermal resistance (K/W) R_{tot} total thermal resistance (K/W)
r	radius (m) r_{2c} corrected fin radius – $r_{2c} = r_2 + t/2$, (m)
R_u	universal gas constant (J/mol·K)
Ra_D	Raleigh number ( )
Re	Reynolds number ( ) Re_{b0} Reynolds number based on bubble departure diameter $Re_{b0} = \frac{\rho_l u_b D_d}{\mu_l}$ Re_δ Reynolds number for condensate flowing down exterior tube wall ( ) Re_l liquid Reynolds number ( ) Re_{tp} two phase Reynolds number ( )
S	suppression factor ( )
T	temperature (K) T_c critical temperature (K) T_g temperature of gas (K) T_{sat} Saturation temperature (K) T_s Surface temperature (K) T_t triple point temperature (K) T_w wall temperature (K)
t	time (s) t_r time for bubble to rise from nozzle to liquid surface (s)
u	velocity (m/s) u_b bubble velocity (m/s)
V	volume (m^3)
v	specific volume (m^3/kg) v_{lv} difference in the specific volume of the liquid phase and vapor phase
X_{tt}	Martinelli parameter ( )

Equations – Greek Symbols

α	thermal diffusivity (m^2/s)
α	void fraction ( )
β	ratio of bubble diameter, D(t), to the bubble departure diameter, D_d, ( )
γ	specific heat ratio ( )
δ	film thickness layer (m)
$\Gamma(a)$	
η_f	single fin efficiency ( )
μ	viscosity (kg/m·s) μ_l liquid viscosity (kg/m·s)
θ_b	temperature difference between heat exchanger base and bulk fluid (K)
π	constant of circumference to diameter ratio of a circle – 3.14159
ρ	density (kg/m^3) ρ_f liquid density (kg/m^3) ρ_g vapor density (kg/m^3) ρ_{fg} difference in liquid density and vapor density (kg/m^3)
σ	condensation and evaporation coefficient ( ) σ_c condensation coefficient ( ) σ_e evaporation coefficient ( )
σ	surface tension (N/m)

Measurement Units

°C	Degrees Celsius
J	Joule
K	Kelvin
kg	kilogram
m	meter
mol	mole
N	Newton
Pa	Pascal Paa Pascal - atmosphere Pag Pascal - gauge
ppm	Parts per million
psi	Pound force per square inch psia pound force per square inch - atmosphere psig pound force per square inch - gauge
s	second
sLm	standard Liters per minute
W	Watt

CHAPTER ONE: INTRODUCTION

Cryogenic Background

Refrigeration is an important technology that sustains our society and economy. One of the initial uses of refrigeration preserved food, enabling the economic shipment of food from source to market. Today refrigeration provides many uses, ranging from conditioning the air within buildings and vehicles to cooling the magnets in medical instruments, such as the Magnetic Resonance Imaging (MRI). A special branch of refrigeration emerged in the nineteenth century known as cryogenics, defined as temperatures below -150°C.

Prior to the 1840s, mechanical refrigeration by compression and isenthalpic expansion could condense most elements and compounds; the remaining elements and compounds were termed "permanent gases". After 1875 refrigeration technology entered the cryogenic temperature range when scientists condensed air. Scientists condensed the remaining "permanent gases" one by one until Onnes finally condensed helium in 1908. Cryogenic refrigeration was confined to the bench top until the early 1900s when Linde developed an economic process on an industrial scale to purify oxygen by the cryogenic distillation of air [1]. Eventually rocketry would take advantage of the industrial scale production of liquid oxygen and other cryogenic propellants and pressurants.

In 1903 the early Russian rocket scientist, Tsiolkovsky, predicted the velocity needed to reach orbit about the Earth and suggested that liquid oxygen and liquid hydrogen offered optimum performance to achieve the orbital velocity [2]. The American, Goddard, launched the first liquid fueled rocket using the cryogenic oxidizer, liquid oxygen, with ethanol in 1926. The Americans also developed the first fully cryogenic rocket engine, powered by liquid oxygen and liquid hydrogen, in 1963 [3]. Today, the hydrogen-oxygen rocket engine remains a common propellant combination, used by the nations of Japan, Europe, India, China, Russia, and the United States [1]. Since the beginning of the space age, rocket scientists have looked to cryogenic refrigeration for efficient transport, thermal control, to increase the propellant density and conserve propellant. Figure 1 shows the cryogenic refrigeration for aerospace applications.

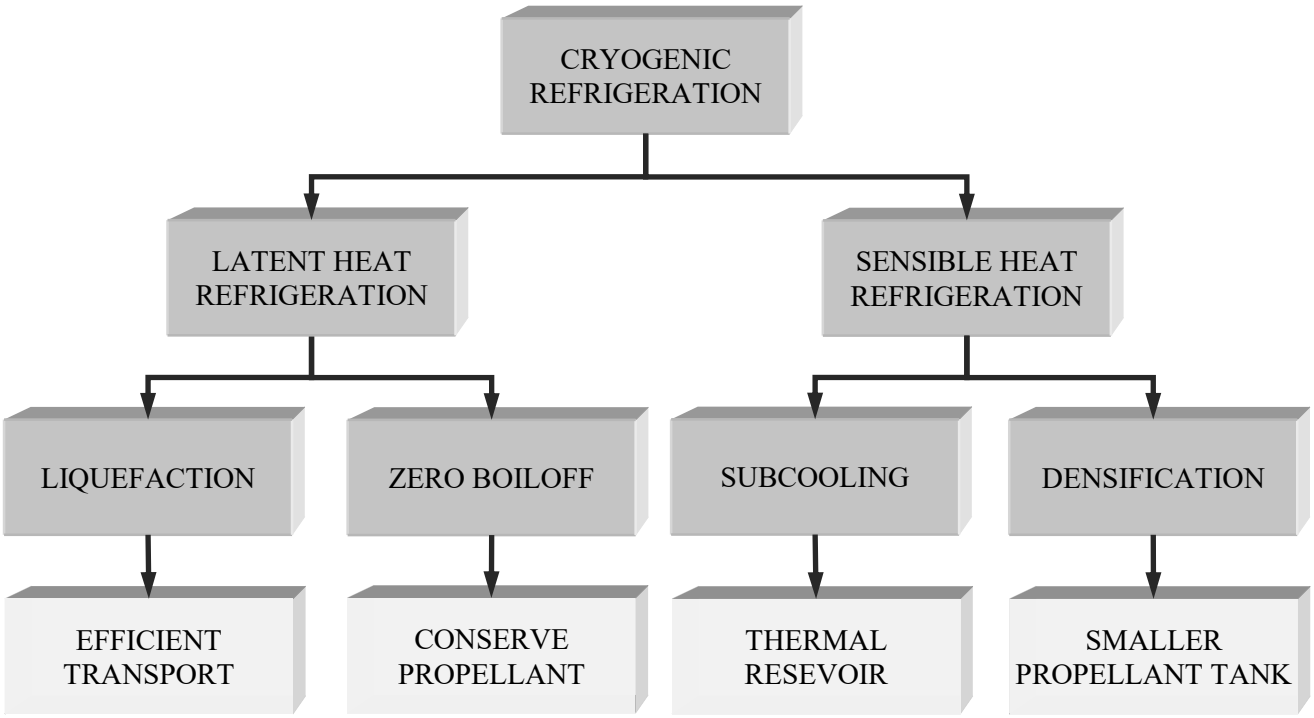

Figure 1: Cryogenic Refrigeration for Aerospace Applications

Liquefaction

Liquefaction of propellant gases typically occurs at the source plant and offers efficient storage and transportation of propellant gases. For instance, liquid oxygen is approximately five times denser than gaseous oxygen transported at the typical industrial pressure of 2400 psi. Accounting for the thicker walls of the pressure vessels on the compressed gas trailer when compared to a cryogenic vessel, six compressed gas trailers deliver the same amount of oxygen as a single delivery of liquid oxygen. Within the rocket, higher rocket efficiencies are gained with higher combustion chamber pressures, which require a pump-fed system. Rocket engines employ turbo pumps to pump liquid to the high pressure, offering better efficiencies than using gas compressors if gas were stored on the rocket as a gas.

A typical liquefier uses some variation of the Claude cycle, which compresses the fluid and subsequently expands the fluid both, isentropically and isenthalpically after removing the heat of compression. An expansion engine, such as a turbine, accomplishes isentropic expansion, while an expansion valve, also known as a Joules-Thomson valve, accomplishes isenthalpic expansion [4].

Currently, no liquefaction occurs at the launch pad of any United States launch facility, since the cryogenic propellant required for launch is delivered as a liquid to storage tanks near the launch pad. However, space missions to other surfaces with in-situ resource utilization, liquefaction at the launch site will be necessary. Proposed methods of propellant liquefaction on other planetary surfaces utilize the compression – heat rejection – expansion methods, such as the Sterling cycle refrigerator [5].

Zero Boil-off

Due to the temperature difference between the ambient temperature surrounding a cryogenic vessel and the temperature of the cryogen, heat transfers from the ambient to the cryogen and the cryogen eventually evaporates from the cryogenic vessel. Early cryogenic scientist/engineer, James Dewar, developed insulated cryogenic vessels, consisting of one glass flask inside of another glass flask. Dewar evacuated the annular space between the two glass flasks to inhibit conductive and convective heat transfer, and Dewar silvered the glass between the glass flasks to inhibit radiation heat transfer. Currently, stainless steel replaced the glass as the vessel material and perlite powder or multi-layer insulation replaced the silvering of vessel material. These vessels are termed dewars, named after James Dewar.

Insulation attempts to reduce heat entering the cryogenic vessel from the ambient, however, no insulation completely stops heat from entering the cryogenic vessel. Thus, heat removal from the dewar remains the only method to maintain the dewar contents at cryogenic temperature. Evaporation of the cryogen removes heat from the dewar through latent heat, but this method expends a portion of the cryogen in order to maintain the temperature. Active cooling employs refrigeration to remove the heat that enters the vessel and requires energy, but conserves the cryogen by prohibiting cryogen evaporation or zero boil-off (ZBO). Economic analysis determines the most beneficial type of insulation for ground support system, while space missions consider overall payload weight and length of service to determine insulation and active cooling requirements.

Zero Boil-off Benefits in Rocketry

Space missions consider ZBO concepts for propellant management and cryogenic coolant. Typically, hypergolic propellants are used on long-term or deep space missions due to the storability of the hypergolic propellants. Although cryogenic propellants offer higher performance than hypergolic engines, no cryogenic propellant will remain through the duration of the long-term mission unless the spacecraft employs a zero boil-off concept. Simple analysis shows that any mission longer than 60 days for liquid hydrogen or 10 days for liquid oxygen benefit from ZBO [6]. Some telescopic instruments aboard spacecraft use cryogens, such as liquid helium, to cool the instruments to reduce radiation noise, however, the mission typically lasts three months because the helium warms to a temperature that can no longer shield radiation noise.

Zero Boil-off Challenges in Rocketry

No technical challenges exist to employ ZBO concepts for ground storage tanks, however, two technical challenges exist for ZBO in space: heat rejection and fluid thermal stratification. A spacecraft relies on radiation heat transfer to reject any heat that an onboard cryogen (1) absorbs from other planetary or stellar bodies through radiation heat transfer or (2) absorbs because of spacecraft electrical power generation through conduction heat transfer. Microgravity, as experienced in space, limits natural convection. Without convection, a spacecraft's cryogenic vessel can experience localized heating leading to complete vaporization in the immediate vicinity of heating even though the mean bulk temperature may remain below the saturation temperature. Thus, other means of convection, such as fans, magnets, or artificial gravity,

provide the heat transfer needed to cool the cryogen evenly while in space. Numerous studies have addressed these issues [7] [8].

Zero Boil-off History in Rocketry

Earth Ground Systems

In the years prior to the Space Shuttle Program, NASA studied concepts to capture the evaporated hydrogen from the two liquid hydrogen storage tanks at Launch Complex 39 (LC-39) at the Kennedy Space Center. At that time approximately 400 gallons of liquid hydrogen evaporated from each of the KSC storage tanks every day. Two studies in the late 1970s suggested to place a cryocooler in the storage tank's existing manhole, located at the top of storage tank, to condense the ullage vapor, maintaining the storage tank at a constant pressure [9][10]. Later in the 2006, Ames Research Center (ARC) analyzed the LC-39 cryogenic tanks for use in the Constellation Program. ARC concluded that a refrigeration system on the LC-39 tanks would be technically viable, however, the study questioned the economic benefits [11].

Passive In-Space Zero Boil-off

While in space, heat is transferred to the cryogenic propellant tank by two modes, conduction and radiation. The Sun, planets, and other stellar bodies transfer heat by radiation to the spacecraft. Also, the spacecraft itself conducts heat, which it absorbs from stellar bodies and generates for spacecraft power, toward the cryogenic propellant tank. Although most spacecraft with cryogenics aboard employ radiation shields and insulation supports to protect the cryogenic propellant tanks from both modes of heat transfer, passive zero boil-off rely exclusively on radiation shields and insulation supports to conserve cryogenic propellant. Passive zero boil-off

is possible for missions beyond the orbit of Mars [12] and for special applications such as the James Webb Space Telescope, which will be deployed to the L2 point where Earth and Sun are aligned so that a single radiation shield can protect the telescope from both bodies [13].

Active In-Space Zero Boil-off

As mentioned above, most spacecraft employ insulation techniques to reduce heat transfer while in space. If the insulation is insufficient to negate the overall heat transfer to the cryogenic propellant tank, active cooling can be employed to offset the heat into the cryogenic propellant tank. In the past 20 years, approximately twenty cryocoolers have been launched aboard NASA satellites. The cryocoolers operated in a temperature range of 55K to 150K, with the exception of the 20K cryocooler aboard the Plank spacecraft. More recent cryocooler designs hope to achieve 6K operational temperatures [14].

Subcooling

Removing sensible heat from the liquid reduces the temperature of a liquid. Also, the vapor pressure of a liquid decreases as the liquid temperature decreases. The saturated temperature occurs at the temperature at which the liquid vapor pressure equals the system pressure. To subcool a liquid, the vapor pressure must be lowered below the system pressure, or stated another way; the temperature must be lowered below the saturated temperature. For further liquid subcooling, the liquid approaches the melting line. A propellant, at the melting line, can exist as a liquid, solid, or slush defined as a mixture of liquid and solid.

Subcooling Benefit in Rocketry

A subcooled propellant provides cooling, or a thermal sink, to a rocket with a small change in volume in the propellant. The amount of cooling a subcooled propellant can store depends on the specific heat of the propellant and the temperature difference between the subcooled liquid temperature and the saturation temperature.

Subcooling History in Rocketry

The National Aerospace Plane (NASP) intended to use slush hydrogen as a propellant. NASA designed the NASP to be capable of withstanding the extreme heat caused by hypersonic velocity. The slush hydrogen was intended to provide cooling to the plane structure prior to combustion.

Densification

As with subcooling, the removal of sensible heat from a liquid increases the density of the liquid. The liquid density depends on temperature alone since a liquid is considered incompressible. Liquid density continually increases from the critical point to triple point regardless of level of subcooling. Since NASA typically stores propellants as single component-two phase with the ullage and liquid at atmospheric pressure, the term densification is typically applied to any density increase above the normal boiling point density.

Density Benefit in Rocketry

Propellant comprises the majority of a rocket's weight just prior to launch; rocket engines, propellant tanks, and payload make up the remaining weight. In order to maximize the payload weight, rocket scientists attempt to minimize the propellant tank weight. Altering the tank material is one method of reducing the propellant tank weight. NASA reconfigured the Space Shuttle's External Tank three times throughout the history of the Space Shuttle Program to reduce weight. Propellant densification, or increasing the density of the propellant, offers another method of reducing the overall rocket weight by making the tank smaller.

Density Challenges in Rocketry

If the propellant refrigeration occurs on the earth's surface and the ullage is not pressurized with a non-condensable, the propellant tank pressure becomes sub-atmospheric, which produces two challenges: (1) structural integrity of the propellant tank as well as (2) possible atmospheric intrusion into the propellant tank. If the intent of refrigeration is to maintain a consistency of slush propellant, further difficulty arises as the liquid temperature approaches the propellant

melting line. Because refrigeration equipment would add weight to a launch vehicle, propellant densification occurs away from the launch vehicle. Difficulty arises when maintaining the propellant in a densified state during transfer from the refrigeration equipment to the launch vehicle due to the heat leak through the propellant transfer lines.

Densification History in Rocketry

The sub-orbital launch vehicle, X-15, from the 1960s utilized a passive system of liquid oxygen densification by replenishing the liquid oxygen from the B-52 carrier aircraft. As the B-52 and X-15 rose to altitude, the liquid oxygen boiling point reduced as the ambient pressure lowered, thus, the bulk liquid oxygen temperature decreased resulting in densified liquid oxygen. The X-33 was intended to use densified liquid oxygen and densified liquid hydrogen, to accomplish a single stage to orbit vehicle. Several ground support systems to provide propellant densification were proposed in the late 1990s to support X-33 flights. One used a sub-atmospheric liquid nitrogen as the working fluid [15] while another proposal bubbling liquid hydrogen through a liquid nitrogen working fluid [16]. The Space Shuttle Program studied densified propellants in the mid 1990s and identified the changes needed to launch the STS with densified propellants; the result was considered too expensive to retrofit the current infrastructure, but recommended looking at densified propellants for a new program [17].

Purpose of This Work

For ground systems, the argument for cryogenic refrigeration system becomes purely economic. The economic trade for propellant ZBO, propellant subcooling, and propellant densification depends on the cost of propellant and rocket specification and performance versus the operational and capital costs of a cryogenic refrigeration system. Propellant liquefaction may occur at the launch site on other planetary surfaces, but will probably occur away from the launch site for future NASA launch concepts from Earth.

Previous concepts use propellant ullage vapor as working fluid to produce refrigeration, which introduces the possibility of contaminating the propellant. Other concepts employed a heat exchanger or cold head within the ullage to control dewar pressure. This paper studies the effect of employing a heat exchanger or cold head beneath the liquid surface. Because the location of the heat exchanger or cold head is inside the tank, this type of configuration is intended for the ground storage tanks on Earth or other planetary surfaces. Specifically, this paper investigates the heat and mass transfer at the vapor-liquid interface as a result of cooling the liquid.

CHAPTER TWO: LITERATURE SEARCH

Condensation

Condensation occurs by four different methods – film condensation, dropwise condensation, homogeneous condensation and direct contact condensation. Film condensation and dropwise condensation occur at a solid surface and depend on surface conditions. Film condensation occurs on a surface that promotes liquid wetting, thus, a thin film of liquid covers the solid surface. Dropwise condensation occurs on a solid surface that inhibits liquid wetting, therefore drops or beads of liquid form over the solid surface. Homogeneous condensation occurs when vapor condenses in the gas phase and the condensation remains suspended in the gas phase. Direct contact condensation occurs when vapor condenses into a body of liquid. Vapor can come in direct contact with a liquid by either the vapor directly above a liquid or by vapor bubbles rising through a body of liquid. The type of condensation investigated in the IRAS experiment is direct contact condensation [18]. Models below predict mass liquefaction rates and heat transfer coefficient of both types of direct contact condensation.

Direct Contact Condensation Models

Direct Contact Condensation by Ullage Collapse

Due to safety concerns, vapor exists above a layer of cryogenic liquid, known as ullage. As the liquid achieves a subcooled state, the ullage pressure above the liquid decreases. In accordance with the gas laws, the decrease in ullage pressure can be attributed to a (a) decrease in ullage

temperature, (b) an increase in ullage volume due to liquid densification, or (c) a decrease in ullage mass due to ullage condensation. Direct Contact Condensation by Ullage Collapse refers to the ullage condensation on a liquid surface and is (a) modeled using kinetic theory and (b) modeled the liquid as a flat, horizontal, cold plate.

Kinetic Theory Model

Condensation heat transfer coefficient has been estimated with the use of kinetic theory. Kinetic theory characterizes the random motion of molecules using statistical mechanics. Equation (1) and Equation (2) are used to predict the mass condensation rate and heat transfer coefficient, respectively [19].

$$G_{COND} = \left(\frac{M}{2\pi R_u T}\right)^{\frac{1}{2}} \left[P_g - P_{sat}\right] \tag{1}$$

$$h = \left(\frac{M}{2\pi R_u T}\right)^{\frac{1}{2}} \frac{h_{lv}^2}{T\, v_{lv}} \tag{2}$$

Equation (1) was modified by applying correction factors to both individual condensation and evaporation mass flux equations. Both mass flux equations are combined into Equation (3), with supporting definitions provided by Equation (4) and Equation (5). No additional heat transfer coefficient is predicted using Equation (3) [19].

$$G_{COND} = \left(\frac{M}{2\pi R_u T}\right)^{\frac{1}{2}} \left[\Gamma(a)\sigma_c P_g - \sigma_e P_{sat}\right] \tag{3}$$

$$\Gamma(a) = \exp(-a^2) + a\sqrt{\pi}[1 + \mathrm{erf}(a)] \tag{4}$$

$$a = \frac{G_{COND}}{P_g}\sqrt{\frac{R\,T}{2\,M}} \tag{5}$$

Cold Plate Model

The cold plate model assumes the heat from the enthalpy of condensation is transferred though the liquid to the cold plate. The heat transferred through the liquid is by thermal conductance and neglects convective heat transfer. The thermal resistance increases with time because the height, or thickness, of the liquid increases as the ullage condenses. Equation (6) and Equation (7) give the mass condensation rate and the heat transfer coefficient, respectively, for the cold plate analysis, as derived in APPENDIX D.

$$G_{COND} = k_l(T_{sat} - T_s)\sqrt{\frac{\rho_l}{h_{lv}\left[2\,k_l\,(T_{sat} - T_s)\,t + \delta_i^2\,h_{lv}\,\rho_l\right]}} \tag{6}$$

$$h = k_l\sqrt{\frac{h_{lv}\,\rho_l}{2\,k_l\,(T_{sat} - T_s)\,t + \delta_i^2\,h_{lv}\,\rho_l}} \tag{7}$$

Direct Contact Condensation by Bubble Collapse

Direct contact condensation of a bubble rising through a layer of subcooled liquid is a complex subject. Typically, the bubbles are injected into the liquid by a nozzle and the bubble separates from the nozzle at a specific diameter, called the bubble departure diameter. Equation (8) estimates the bubble departure diameter [20].

$$D_{b,d} = \sqrt[3]{\frac{6\,\sigma\,D_n}{\rho_{lv}\,g}} \tag{8}$$

The diameter of the bubble continually decreases as the bubble rises through the subcooled liquid because of bubble vapor cooling. The vapor within the bubble cools as the bubble transfers heat to the subcooled liquid, which reduces the volume of the bubble according to the gas laws and ultimately condenses portions of the bubble. Equation (9) shows the rate at which the bubble diameter decreases as with time [21].

$$\beta = \frac{D_b(t)}{D_{b,d}} = \left(1 - \frac{3}{\sqrt{\pi}}\,\mathrm{Ja}\,\sqrt{\mathrm{Re}_{bo}}\,\mathrm{Pr}^{\frac{1}{3}}\,\mathrm{Fo}_o\right)^{\frac{2}{3}} \tag{9}$$

Although literature has suggested that a bubble rising through subcooled liquid goes through an acceleration and deceleration phase [22], this study assumes constant vertical velocity. Equation (10) calculates the vertical bubble velocity [23].

$$u_b = \frac{C_z}{1-\alpha}\left(\frac{g\,\sigma\,\rho_{lv}}{\rho_l^2}\right)^{\frac{1}{4}} \tag{10}$$

As mentioned above, the bubble collapses as it rises to the surface, partly due to condensation of the vapor within the bubble. The mass of the vapor that condenses while the bubble rises is dependent on the heat transfer rate and the residence time the bubble spends within the subcooled liquid. Given the above constant bubble rise velocity assumption, Equation (11) calculates the residence time of the bubble within the subcooled liquid.

$$t_r = \frac{H}{u_b} \tag{11}$$

Equation (12) calculates the mass that condenses from a single spherical bubble.

$$m_{b,cond} = \rho_v \frac{4\pi}{3}\left(\frac{D_{b,d}}{2}\right)^3 - \rho_v \frac{4\pi}{3}\left(\frac{D_{t_r}}{2}\right)^3 \tag{12}$$

However, during the proposed IRAS test matrix as outlined in the following chapter, a steady stream of bubbles departs from the nozzle instead of a single bubble. The frequency at which a bubble departs the nozzle depends on the mass flow rate of the gas flowing through the nozzle and the mass of the bubble at departure. Equation (13) and Equation (14) calculate the bubble departure frequency and mass condensation rate of the bubble. APPENDIX D shows the derivation for Equation (13) and Equation (14).

$$f_{b,d} = \frac{6\,\dot{m}_{GO_2}}{\pi\,\rho_v\,D_{b,d}^3} \tag{13}$$

$$\dot{m}_{b,cond} = \dot{m}_{GO_2}\left(1 - \beta_{t_r}{}^3\right) \tag{14}$$

Densification Rate Models

The densification of liquid oxygen occurs during the cooling of liquid oxygen, however, the rate at which liquid oxygen densifies is important. Transient heat conduction analysis is used to predict the densification rate of liquid oxygen in the IRAS dewar. Equation (15) is used to predict the position-temperature profile of the liquid above the heat exchanger, while Equation (16) is used to predict the position-temperature profile of the liquid below the heat exchanger. APPENDIX D derives the Equation (15) and Equation (16).

$$T(y,t) = \theta(y,t) + T_s = \frac{\theta_i}{H} y + \sum_{n=1}^{\infty} \frac{2\theta_i}{n\pi} \sin\left(\frac{n\pi y}{H}\right) e^{-\alpha\left(\frac{n\pi}{H}\right)^2 t} + T_s \qquad (15)$$

$$T(y,t) = \theta(y,t) + T_s = \sum_{n=1}^{\infty} \frac{4\theta_i}{(2n-1)\pi} \sin\left(\frac{(2n-1)\pi\, y}{2\, H}\right) e^{-\alpha\left[\left(\frac{2n-1}{2}\right)\frac{\pi}{H}\right]^2 t} + T_s \qquad (16)$$

Previous IRAS Work

The Integrated Refrigeration and Storage (IRAS) system is a dewar with a large flanged connection at the top of the dewar. The large flanged connection allows instrumentation cables and fluid connections pass from the inside of the dewar to the outside. The fluid connections are intended for liquid nitrogen coolant to flow through a heat exchanger, which is intended to simulate the cold head of a Brayton cycle cryocooler. The flange connection allows cold head height to be altered. The following chapter provides additional details of the IRAS system and supporting equipment.

Eden Cryogenics delivered the IRAS to KSC in the summer of 2008. Over the next nine months, the IRAS was cleaned to oxygen cleanliness specifications, integrated with the rest of the test apparatus, and functionally tested with liquid nitrogen. The liquid nitrogen functional test determined the heat transferred to the IRAS wall from the ambient as 17.5W [25].

Following the liquid nitrogen functional test, ZBO experimentation began with liquid oxygen. Liquid oxygen filled the IRAS dewar to approximately 70% of full capacity. The heat exchanger was placed at the 10%, 40%, and 60% locations inside the IRAS dewar, and ZBO runs occurred at an IRAS dewar pressure of 3 psig, 5 psig, and 7 psig. Results from these experimental testing showed that the optimum heat exchanger location was at the 40% level [26].

CHAPTER THREE: METHODOLOGY

Experimental Setup

The Integrated Refrigeration and Storage (IRAS) dewar comprises the main test article for this study and is complimented by a liquid nitrogen supply, a gaseous oxygen supply, a nitrogen subcooler, numerous analyzers and sensors, and a data acquisition system. Figure 2 shows the simplified schematic of the experimental setup, while Table 1 shows the component legend. APPENDIX B provides the detailed schematic and component specification list.

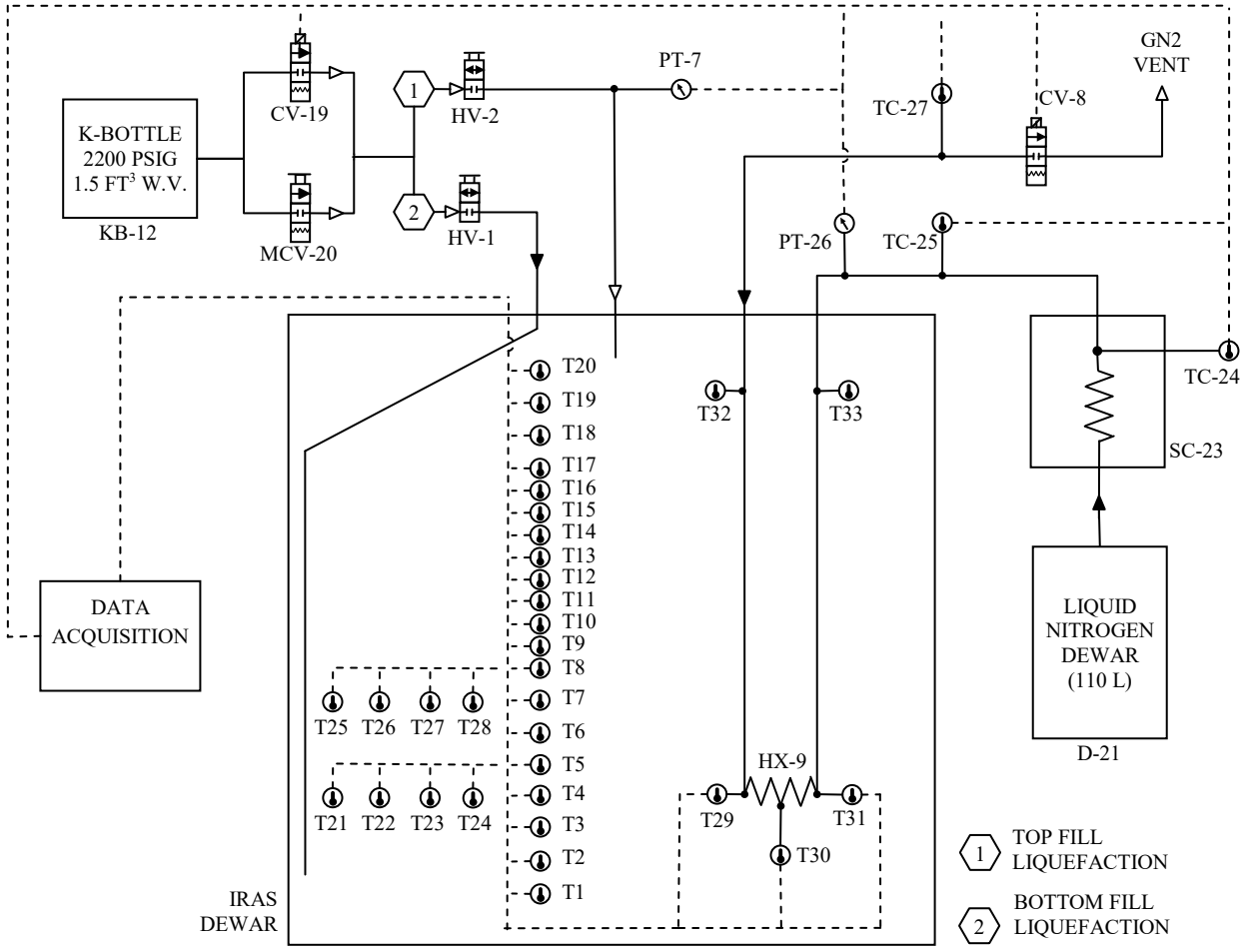

Figure 2: Experimental Setup - Simplified Process and Instrumentation Diagram

Table 1: Experimental Setup - Simplified Process and Instrumentation Diagram Legend

REFERENCE DESIGNATOR	DESCRIPTION
HV-1	IRAS Dewar Inlet Valve
HV-2	IRAS Dewar Exit Valve
PT-7	IRAS Dewar Pressure Transducer
CV-8	IRAS Heat Exchanger Mass Flow Control Valve
HX-9	IRAS Heat Exchanger
HX-10	Coolant Ambient Heat Exchanger
KB-12	Gaseous Oxygen K-Bottle
CV-19	Mass Flow Control Valve (GO2)
MCV-20	Manual Mass Flow Control Valve (GO2)
D-21	Liquid Nitrogen Supply Dewar
SC-22	Subcooler
TC-24	Subcooler Cooling Fluid Exit Temperature Sensor
TC-25	Subcooler Process Fluid Exit Temperature Sensor
PT-26	Subcooler Process Fluid Exit Pressure Transducer

IRAS

The IRAS was custom built, consisting of a 400 liter dewar and a male bayonet. Both components were constructed of 304 stainless steel and double walled with a nominal vacuum of five microns of mercury within the annular space. The IRAS dewar has an inner diameter of 30 inches with F&D ASME heads. Figure 3 shows a cross-sectional view of the IRAS.

Male Bayonet

The male bayonet connects to the IRAS dewar by a ten inch flange and all sensor and nitrogen fluid connections route through the male bayonet. Non-vacuum jacketed nitrogen fluid lines extend approximately one foot below the male bayonet and terminate with threaded fittings. Stainless steel tubing connects the terminated nitrogen fluid fitting to a copper heat exchanger. The copper heat exchanger is in the shape of a “U” and has annular fins. The stainless steel

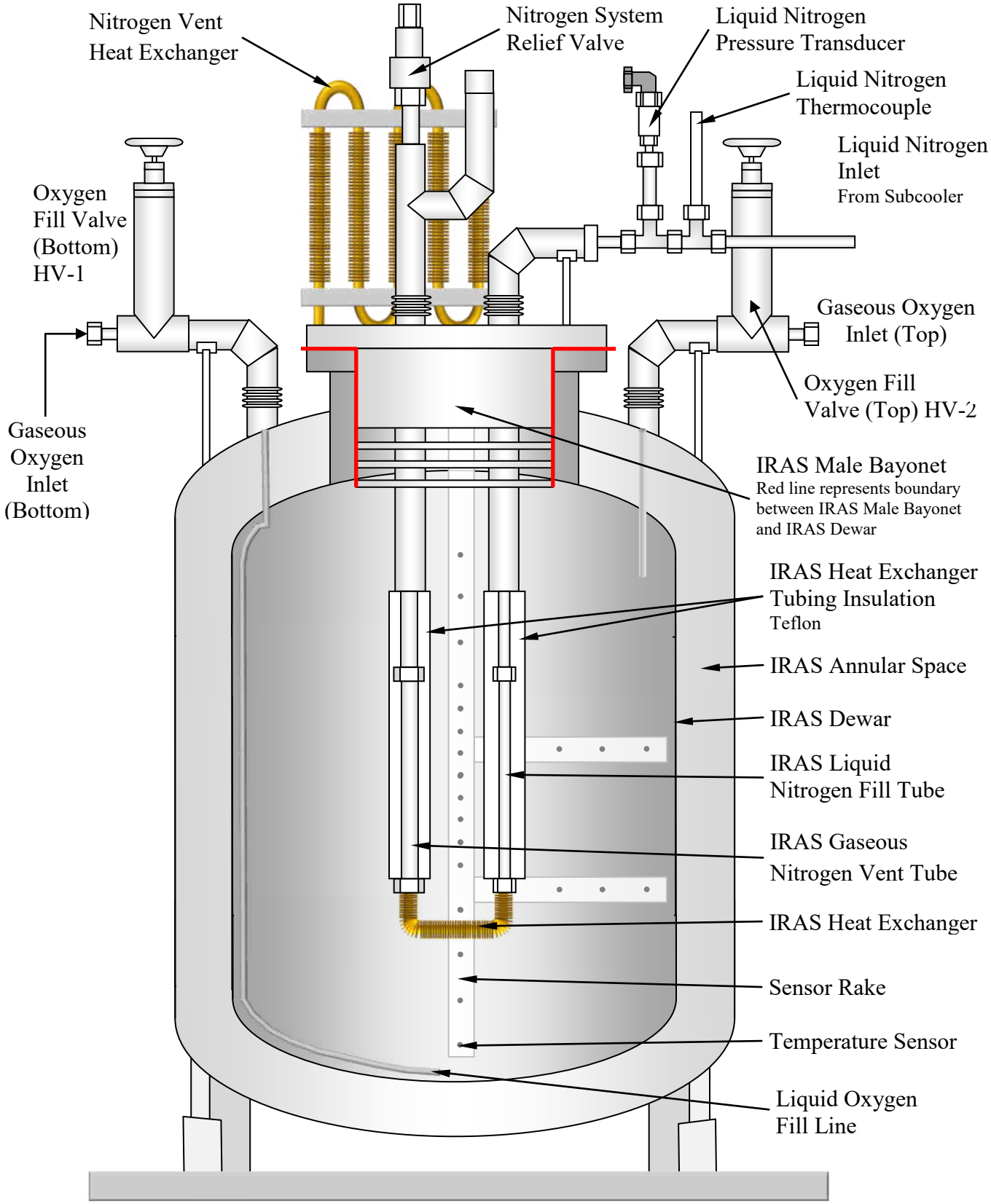

Figure 3: Cross-Section of IRAS Dewar and Male Bayonet

tubing is insulated with Teflon tubing from the copper heat exchanger to the bottom of the vacuum insulated male bayonet. Heat transfer analysis of the Teflon insulated stainless steel tubing and copper heat exchanger is provided in APPENDIX A. Also attached to and extending below the male bayonet is a micarta instrumentation rake, where the internal temperature sensors, resistance temperature diodes, are strategically placed. The instrumentation rake extends to about six inches above the bottom of the IRAS dewar, with two horizontal rakes measuring the lateral temperature gradient.

IRAS Dewar

The IRAS dewar is an open container with a neck sized to accept the IRAS Male Bayonet. The liquid oxygen fill line and gaseous oxygen vent line are routed through the annular space, around the neck, and routed to the inside of the IRAS Dewar. Both lines have an external manual valve. Two pressure relief valves and a burst disc, which are located between the IRAS Dewar and the valve in the gaseous oxygen vent line, provide over-pressurization protection of the dewar. The IRAS dewar pressure is monitored by a pressure gauge and a pressure transducer, which is connected to the data acquisition system.

IRAS Support Equipment

Liquid Nitrogen Supply

A 110 liter dewar provides liquid nitrogen to the IRAS dewar. The liquid nitrogen supply dewar has a MAWP of 90 psi, however, the liquid nitrogen dewar pressure was typically maintained between 20 psig and 40 psig. The liquid nitrogen is procured to a military specification, MIL-

PRF-27401E Grade B, which is industrial grade nitrogen. The procurement requirements and laboratory analyses are found in APPENDIX C.

Gaseous Oxygen Supply

A 1.5 cubic foot water volume k-bottle provides gaseous oxygen to the IRAS dewar. The gaseous oxygen k-bottle has a MAWP of 2,200 psi. The gaseous oxygen is procured to a military specification, MIL-PRF-25508G Grade F, which is electronic grade oxygen. The oxygen is 99.99% oxygen allowing a maximum impurity concentration of 100 parts per million. The procurement requirements and laboratory analyses is found in APPENDIX C. The gaseous oxygen pressure is regulated down to approximately 50 psig upstream of the mass flow controller.

Nitrogen Subcooler

The liquid nitrogen supply dewar is operated at an elevated pressure in order to flow liquid nitrogen to the IRAS dewar. Once the liquid nitrogen supply tank reaches steady state conditions, the nitrogen becomes saturated at the elevated pressure, which corresponds to an elevated bulk liquid nitrogen temperature. As the liquid nitrogen flows to a lower pressure, a portion of the liquid nitrogen evaporates increasing the quality of the liquid nitrogen. Since the heat removed from the IRAS dewar is calculated by the latent heat of liquid nitrogen flowing through the IRAS, the validity of the calculation depends on the ability to obtain liquid nitrogen with no quality. The nitrogen subcooler is employed to subcool the liquid nitrogen and subsequently ensure the quality remains negligible.

The nitrogen subcooler is composed of copper tubing and a double-walled vat. The vat is approximately 18 inches deep, 18 inches wide, and 36 inches long, constructed of double-walled aluminum. For all test runs, the vat is filled with liquid nitrogen. The copper tubing is ½" tubing that coiled at a diameter of 12 inches. The copper tubing is located downstream of the liquid nitrogen supply dewar and upstream of the IRAS dewar and is physically located in the vat. The copper tubing is connected to the LN_2 supply dewar and the IRAS dewar by ½" vacuum insulated flexible hoses.

Flow Control Valves

The flow control valves measure and set the mass flow rates of the liquid nitrogen and the gaseous oxygen, which controls the cooling rate in the IRAS and measures the oxygen condensation rate. The oxygen and nitrogen flow control valves range from 0-20 standard liters per minute (sLm) and 0-100 sLm, respectively, with a tolerance of ±0.2 sLm and ±1 sLm, respectively. In addition to the GO_2 flow control valve, a manual metering valve, with a range of 0-10 sLm, is in parallel to the GO_2 flow control valve, providing a total possible oxygen condensation of 30 sLm.

Data Acquisition

The computer software, Labview, acquires data from the IRAS sensors or pressure transducers, thermocouples, resistance diodes, and mass flow controllers. The IRAS sensors are connected to field points and then to an ethernet switch. The ethernet switch is connected to the computer by a single RJ45 network cable. Labview records the signals from the pressure and temperature sensors and records and controls the mass flow controllers.

Test Configurations

The Integrated Refrigeration and Storage (IRAS) dewar is designed to measure the energy flow in a cryogenic storage system during active refrigeration. Figure 4 shows the energy balance about the IRAS, with the dotted line representing the control volume.

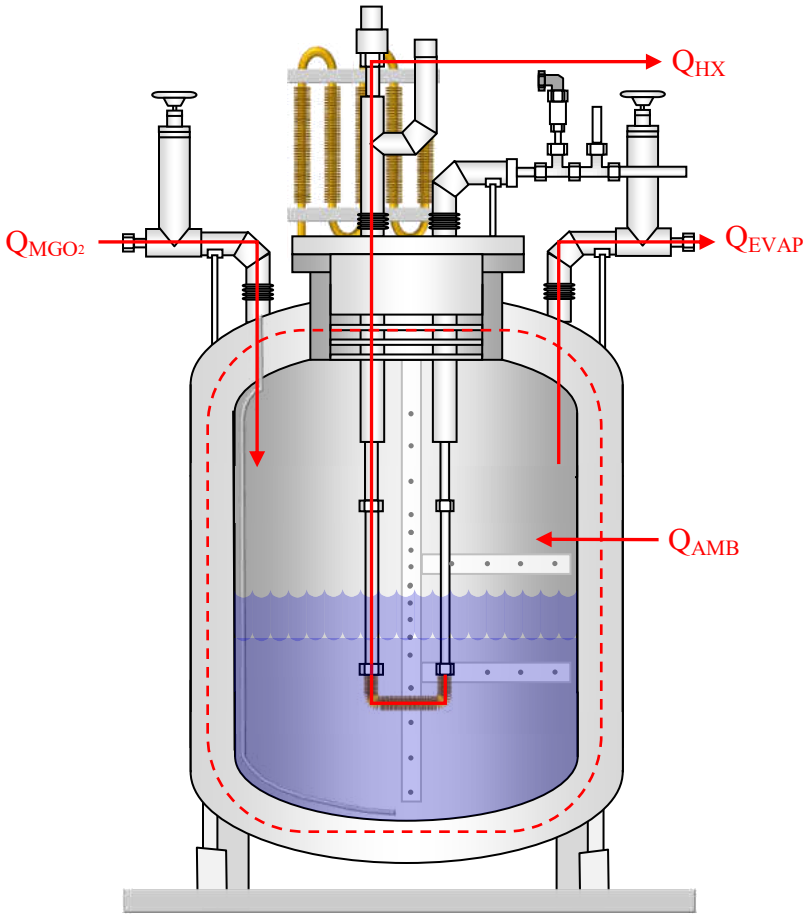

Figure 4: IRAS Energy Balance

Table 2: IRAS Energy Balance Definitions

Label	Definition
Q_{MGO2}	Heat entering IRAS dewar with gaseous oxygen
Q_{HX}	Heat exiting IRAS dewar through the IRAS heat exchanger
Q_{EVAP}	Heat exiting IRAS dewar through evaporation
Q_{AMB}	Heat entering IRAS dewar through IRAS dewar insulation

The IRAS energy balance from Figure 4 is defined by Equation (17).

$$Q_{AMB} + Q_{\dot{m}_{GO_2}} = Q_{EVAP} + Q_{HX} \tag{17}$$

From Equation (17) the individual heat components will be isolated for possible quantification in the following tests.

Test 1

The first test quantifies the ambient heat component by not adding gaseous oxygen or liquid nitrogen through the heat exchanger. This type of operation is typically termed normal evaporation, and the mass flow rate exiting the IRAS is typically termed the Normal Evaporation Rate. Under the normal evaporation configuration, Equation (17) reduces to Equation (18).

$$Q_{\dot{m}_{GO_2}} = Q_{HX} = 0$$

$$Q_{AMB} = Q_{EVAP} \tag{18}$$

Test 2

The second test quantifies the efficiency the heat exchanger by operating the IRAS dewar in a zero boil-off (ZBO) configuration, or no evaporation, with no addition of GO_2 into the IRAS dewar. Three variations of Test 2 are run, which varies the vertical height of the IRAS heat exchanger. Under ZBO conditions, Equation (17) reduces to Equation (19).

$$Q_{\dot{m}_{GO_2}} = Q_{EVAP} = 0$$

$$Q_{AMB} = Q_{HX} \tag{19}$$

Test 3

The third test quantifies the liquefaction rate of the IRAS dewar. Gaseous oxygen enters the IRAS dewar, while the IRAS maintains ZBO conditions and no gaseous oxygen enters the IRAS dewar. Two variations of Test 3 are run; one test flows gaseous oxygen into the ullage, while the other test flows gaseous oxygen into the liquid. The two tests are intended to isolate the condensation rate, or liquefaction rate, at the surface of the liquid. For the liquefaction runs, Equation (17) reduces to Equation (20).

$$Q_{EVAP} = 0$$

$$Q_{AMB} + Q_{\dot{m}_{GO_2}} = Q_{HX} \tag{20}$$

Test 4

The fourth test quantifies the densification rate of liquid oxygen in the IRAS dewar. Since the ullage pressure becomes sub-atmospheric if the temperature of liquid oxygen is reduced below its normal boiling point, gaseous oxygen enters the IRAS dewar in order to maintain a positive pressure. Under the densification conditions, IRAS still maintains ZBO conditions and Equation (17) reduces to Equation (20).

Test Matrices

Although Test 1 was performed in a previous study, Test 1 was performed again at atmospheric pressure under this study and compared to the reported value of 17.5W. The remaining tests will be performed at three different IRAS dewar pressures. Table 3, Table 4, and Table 5 show the test matrices to accomplish Test 2, Test 3 and Test 4.

Table 3: Test 2 Matrix – Zero Boil-off

Test Run Number	IRAS Set Pressure	Gaseous Oxygen Flow Rate
Test Run 2a	3 psig (20.7 kPag)	0 sLm
Test Run 2b	5 psig (34.5 kPag)	0 sLm
Test Run 2c	7 psig (48.3 kPag)	0 sLm

Table 4: Test 3 Matrix – Liquefaction

Test Run Number GO_2 Top Fill	Test Run Number GO_2 Bottom Fill	IRAS Set Pressure	Gaseous Oxygen Flow Rate
Test Run 3a	Test Run 3aa	3 psig (20.7 kPag)	2.5 sLm
Test Run 3b	Test Run 3bb		5.0 sLm
Test Run 3c	Test Run 3cc		7.5 sLm
Test Run 3d	Test Run 3dd		10.0 sLm
Test Run 3e	Test Run 3ee		15.0 sLm
Test Run 3f	Test Run 3ff		20.0 sLm
Test Run 3g	Test Run 3gg	5 psig (34.5 kPag)	2.5 sLm
Test Run 3h	Test Run 3hh		5.0 sLm
Test Run 3i	Test Run 3ii		7.5 sLm
Test Run 3j	Test Run 3jj		10.0 sLm
Test Run 3k	Test Run 3kk		15.0 sLm
Test Run 3l	Test Run 3ll		20.0 sLm
Test Run 3m	Test Run 3mm	7 psig (48.3 kPag)	2.5 sLm
Test Run 3n	Test Run 3nn		5.0 sLm
Test Run 3o	Test Run 3oo		7.5 sLm
Test Run 3p	Test Run 3pp		10.0 sLm
Test Run 3q	Test Run 3qq		15.0 sLm
Test Run 3r	Test Run 3rr		20.0 sLm

Table 5: Test 4 Matrix – Densification

Test Run Number	IRAS Set Pressure	Liquid Nitrogen Flow Rate
Test Run 4a	3 psig (20.7 kPag)	100 sLm
Test Run 4b	5 psig (34.5 kPag)	100 sLm
Test Run 4c	7 psig (48.3 kPag)	100 sLm

CHAPTER FOUR: RESULTS AND DISCUSSION

Initial IRAS Checkout

Instrument Checkout

Prior to liquid oxygen test runs, the IRAS was filled with liquid nitrogen to checkout or ensure proper performance of the pressure, temperature, and flow instrumentation. Initially, the IRAS was subjected to atmospheric pressure by opening of hand valve, HV-2. During this phase of checkout, resistance temperature diode, T27, T30, T32,and T33 read off-scale high at 1123K, while thermocouple, TC1 (Labview designator) read off-scale high at 2048K. The T27 temperature sensor was not replaced because T27 measures the temperature of a lateral position provides no relevant information for the calculations of liquefaction and densification. The T30 thermocouple was damaged during the installation of the Teflon tubing on the vent and fill tubing in the IRAS heat exchanger. The T32 and T33 thermal resistance diodes were never connected to Labview. The thermocouple, TC1, was used for previous IRAS testing and not connected to Labview during the liquefaction and densification testing outlined in this report. Thus, the temperature sensors were deemed capable of providing sufficient measurements for the test matrices outlined above in CHAPTER THREE.

The second phase of checkout ensured the proper performance of the pressure transducers. The IRAS dewar was allowed to pressurize to the relief valve, RV-11, set at 8 psig. The pressure

gauge, PG-6, correlated well with the PT-7 as read on the Labview program during the pressurization. The IRAS heat exchanger loop was pressurized with gaseous helium to 25 psig, as recorded with a separate pressure gauge, while PT-26 correlated well to that pressure input.

IRAS Heat Exchanger Leak Check

As mentioned in CHAPTER THREE, stainless steel and copper compose the IRAS heat exchanger. The tubing were connected using a threaded fitting at ambient conditions and as the metals cool to liquid nitrogen temperatures, the two metals contract at different rates. A pressure decay test was conducted to ensure the IRAS heat exchanger did not develop a leak during cool down. While liquid nitrogen was in the IRAS dewar, the IRAS heat exchanger loop was pressurized to approximately 25 psig with gaseous helium and allowed to decay for fifteen minutes. The pressure decay was approximately 0.5 psig over the fifteen minutes and the profile is shown in Figure 5. Equation (21) represents an isentropic pressure vessel blowdown analysis, while Equation (22) represents an isothermal blowdown analysis to estimate the size of the leak within the heat exchanger loop [28]. Equation (21) and Equation (22) estimate a 0.00010 inch diameter leak and 0.00023 inch diameter leak, respectively. Equation (23) estimates the mass flow rate [29] through the leak at 0.0071 sLm of nitrogen and 0.028 sLm of nitrogen by the isentropic blowdown analysis and isothermal blowdown analysis, respectively. Assuming an eight-hour test with an initial volume of 200 L of LO_2 in the IRAS dewar, Equation (21) and Equation (22) estimates an increase in the nitrogen content of liquid oxygen within the IRAS dewar by approximately 20 ppm and 80 ppm, respectively. The isentropic blowdown analysis predicts the LO_2 remains within specification limits (APPENDIX C), while the isothermal blowdown analysis predicts the nitrogen content within the LO_2 slightly exceeds the

specification limits. Nevertheless, the assumption that the liquid and ullage are composed of a single species is reasonable.

$$\frac{P}{P_i} = \left[1 + \left(\frac{\gamma - 1}{2}\right)\left(\frac{2}{\gamma + 1}\right)^{\frac{(\gamma+1)}{2(\gamma-1)}} \sqrt{\frac{\gamma\, g_c P_i}{\rho_i}}\ \frac{A\, t}{V}\right]^{\frac{-2\gamma}{(\gamma-1)}} \tag{21}$$

$$\frac{P}{P_i} = \exp\left[-\left(\frac{\gamma - 1}{2}\right)\left(\frac{2}{\gamma + 1}\right)^{\frac{(\gamma+1)}{2(\gamma-1)}} \sqrt{\frac{\gamma\, g_c P_i}{\rho_i}}\ \frac{A\, t}{V}\right] \tag{22}$$

$$\dot{m} = \rho\, Q = \rho\, C_D\, A \sqrt{2 \frac{\Delta P\, g_c}{\rho}} = C_D\, A \sqrt{2\, P\, \rho\, g_c} \tag{23}$$

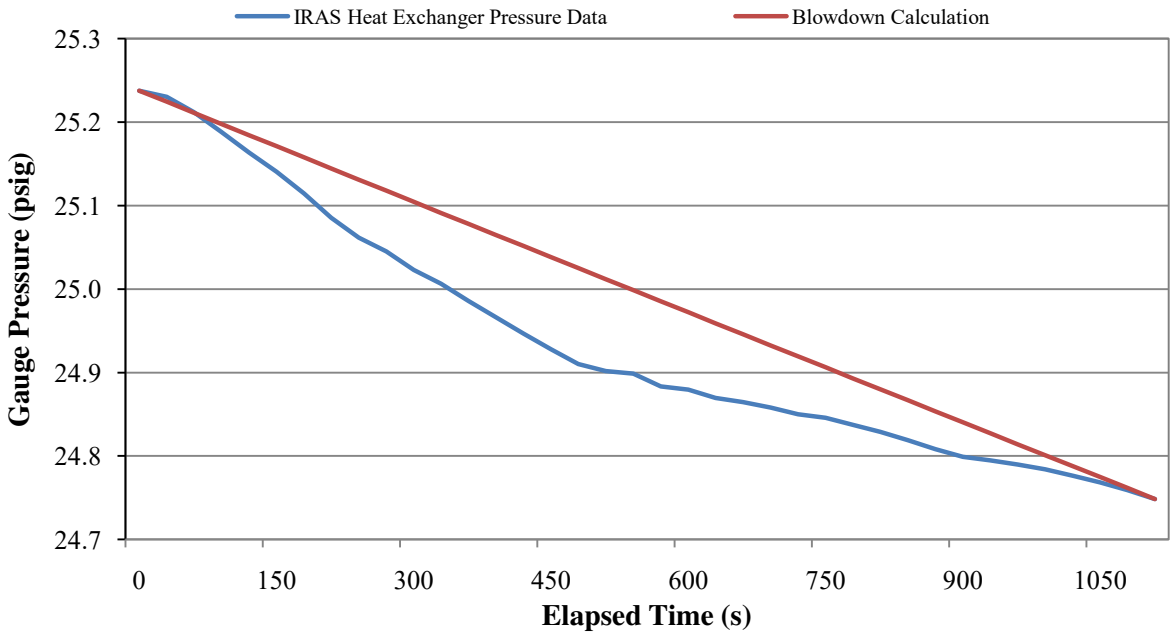

Figure 5: IRAS Heat Exchanger Leak Check

Temperature Profile within the IRAS Dewar

Figure 6 shows the temperature profile of saturated liquid oxygen within the IRAS at steady state conditions. Natural convection currents within the liquid provide sufficient mixing to maintain a uniform temperature with no thermal stratification within the liquid. However, a temperature gradient exists within the ullage and is thermally stratified. Thermal stratification in the ullage occurs because a constant temperature boundary condition exists at the liquid portion of the liquid-vapor interface due to the consequent vaporization. Heat transfer from the ambient warms the vapor at the dewar wall causing the vapor to become less dense and more buoyant. Because the lowest temperature in the ullage exists at the bottom of the ullage, natural convection is too weak to provide sufficient mixing within the ullage.

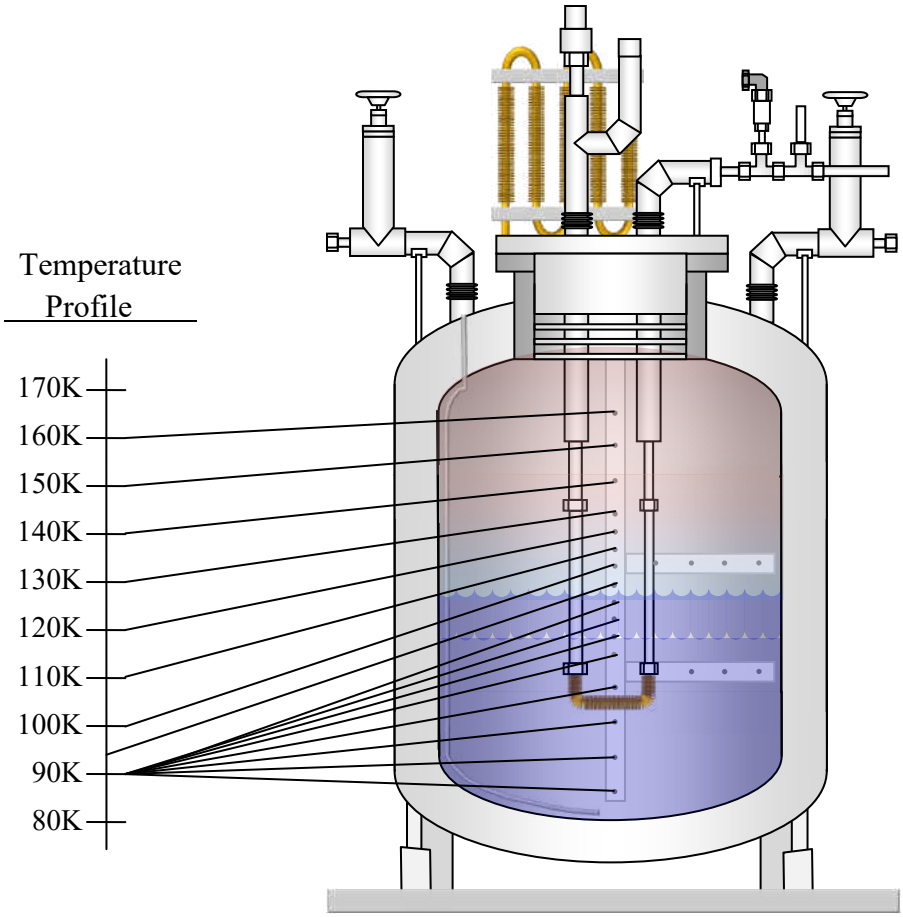

Figure 6: Temperature Profile of IRAS Containing Liquid Oxygen at Steady State Conditions

Normal Evaporation Test

From Equation (18), the heat transferred to the IRAS dewar from the ambient can be determined by measuring the mass flow rate that evaporates from IRAS. The heat released from the IRAS with the evaporation is calculated by Equation (24).

$$Q_{EVAP} = \dot{m}(h_f - h_i) = \dot{m}\left[\int_{T_i}^{T_{BP}} c_{P,l}dT + h_{lv} + \int_{T_{BP}}^{T_f} c_{P,v}dT\right] \quad (24)$$

Once the liquid within the IRAS dewar reaches steady conditions, the liquid is saturated at the IRAS dewar pressure, however, a temperature gradient exists within the ullage as discussed above. Thus, the liquid sensible heat portion of Equation (24) can be neglected, while the vapor sensible heat portion of Equation (24) remains a significant fraction of the total evaporation heat calculation.

With the IRAS dewar filled with liquid nitrogen, a flow meter was placed on the IRAS dewar vent, downstream of HV-2, during normal venting to measure the mass flow rate of the normal evaporation. The average flow rate over the period of an hour measured 5.3 sLm, and the measured ullage temperature gradient ranges from 77 K to 160 K. The measured flow rate represented an average heat transfer rate of 17.6 W, which agrees well with the value reported by Notardonato.

Zero Boil-off

From Equation (19), the heat transferred to the IRAS dewar from the ambient can be removed by the coolant through the IRAS heat exchanger. The heat removed from the IRAS dewar is measured and calculated by Equation (25).

$$Q_{HX} = \dot{m}_{N_2}(h_{HX\ Exit} - h_{HX\ Inlet}) = \dot{m}_{N_2}\left[\int_{T_{HX\ Inlet}}^{T_{BP}} c_{P,l}dT + h_{lv} + \int_{T_{BP}}^{T_{HX\ Exit}} c_{P,v}dT\right] \quad (25)$$

The inlet condition is measured by TC-24 and PT-26 to determine saturation conditions and level of subcooling, while the exit condition is by TC-27. The cooling requirement as determined by Equation (25) is 81.4 W, 67.8 W, and 60.7 W for IRAS pressures of 3 psig, 5 psig, and 7 psig, respectively.

Liquefaction

From Equation (20), the heat that enters the IRAS dewar with the oxygen flow rate is removed by the coolant through the IRAS heat exchanger. The heat removed from the IRAS dewar is measured and calculated by Equation (20) and Equation (25). Another way to measure the heat removed from the IRAS dewar during the liquefaction tests is by Equation (26).

$$Q_{\dot{m}_{O_2}} = \dot{m}_{O_2}\left(h_{Vapor,Ambient} - h_{Liquid,BP}\right) = \dot{m}_{O_2}\left[\int_{T_{Ambient}}^{T_{BP}} c_{P,v}dT - h_{lv}\right] \quad (26)$$

Equation (20) coupled with Equation (25) or Equation (26) provides the heat transfer for the entire IRAS dewar. The results from Equation (26) predict that the cooling rate for GO_2 starting at a temperature of 295K is 8.75 W/sL, 8.71 W/sL, and 8.66 W/sL for 3 psig, 5 psig, and 7 psig, respectively. Liquefaction of oxygen at varying pressures requires different cooling

requirements because of (1) oxygen latent heat decreases as pressure increases, and (2) sensible heat decreases as pressure increases due to the higher boiling point. Equation (1), Equation (2), Equation (3), Equation (6), and Equation (7) predict the heat and mass transfer at the vapor-liquid interface.

Liquefaction – Top Fill

For the Test Run 3a through Test Run 3r, the gaseous oxygen flows through the IRAS vent valve, HV-2, and enters the IRAS dewar from the top. The gaseous oxygen enters the IRAS dewar at a temperature close to ambient, which is the temperature the gaseous oxygen k-bottle. The gaseous oxygen stream enters as a jet into the ullage, however, the gas begins to rise due to buoyancy effects as soon as the downward velocity dissipates. Figure 7 shows the warm gaseous oxygen entering the IRAS dewar, with the isotherms within the ullage.

Because of the buoyancy effects within the ullage, liquefaction by the top fill method condenses the cold isothermal layers nearest the liquid-vapor interface. No mass motion occurs in the ullage except for the general bulk downward movement of the ullage to replace the volume occupied by the vapor that is condensed. Thus, the heat transfer from the liquid surface to the gaseous oxygen is conduction dominant.

Once active cooling is initiated, the cooling from IRAS heat exchanger establishes an artificial boundary, where natural convection currents exist below the heat exchanger and heat is transferred by conduction above the heat exchanger. No convection exists above the heat

exchanger because the lower temperature at the heat exchanger is on the bottom, while the warmer temperature at the vapor-liquid interface is on the top.

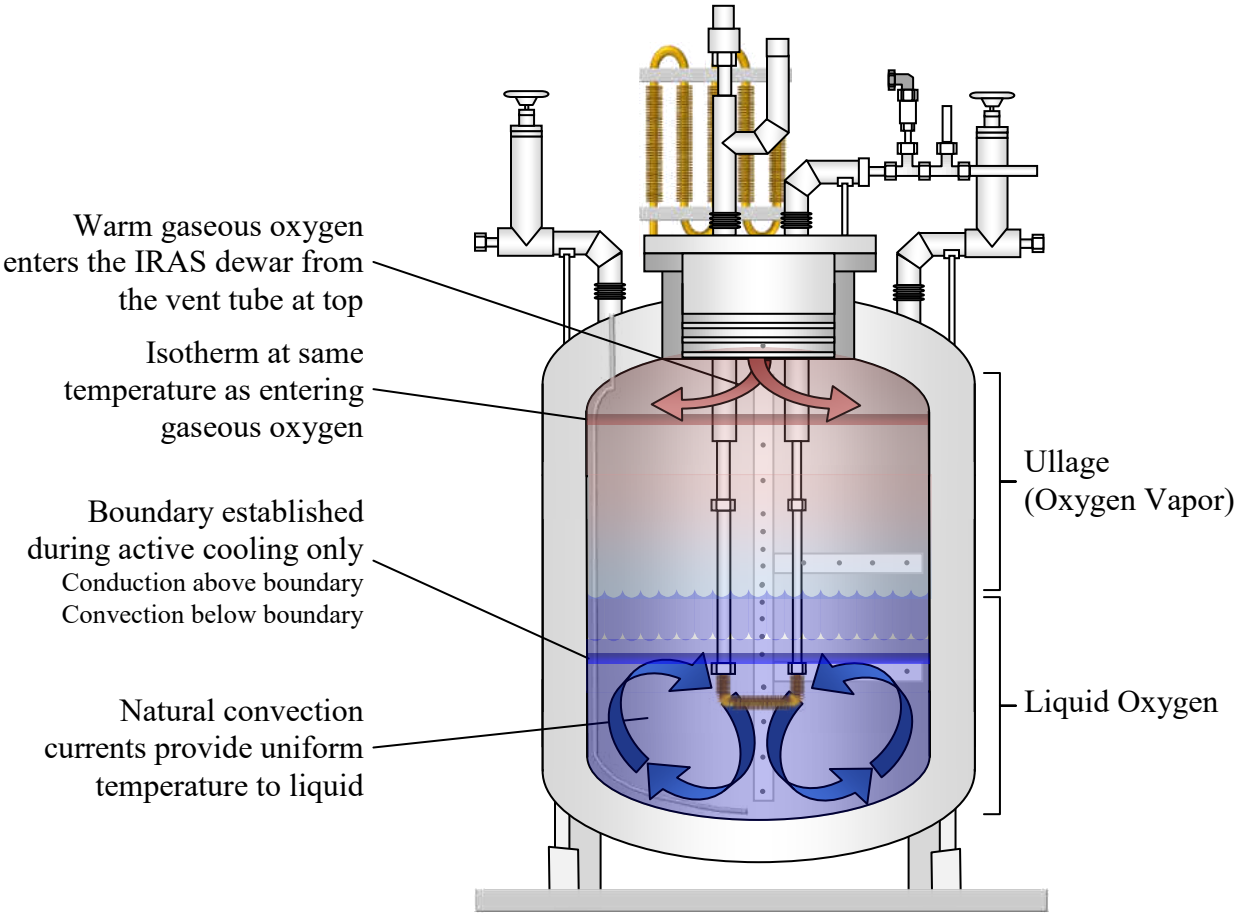

Figure 7: Convection Currents within IRAS Dewar during Top Fill Liquefaction

Liquefaction-Top Fill Experimental Data

Figure 8 shows the liquid temperature data for liquefaction runs (3q, 3b, 3d, 3e, and 3r) that occurred on 9/1/10 and 9/2/10. The bold line represents oxygen saturated temperature, which is calculated from Equation (112), and is located between the temperature sensors, T7 and T8. Thus, the vapor-liquid interface is located between 53 cm, the height of T7, and 61 cm, the height of T8. During active cooling through the IRAS heat exchanger, HX-9, the liquid below the IRAS heat exchanger experiences no thermal stratification, while the liquid above the IRAS heat exchanger is thermally stratified.

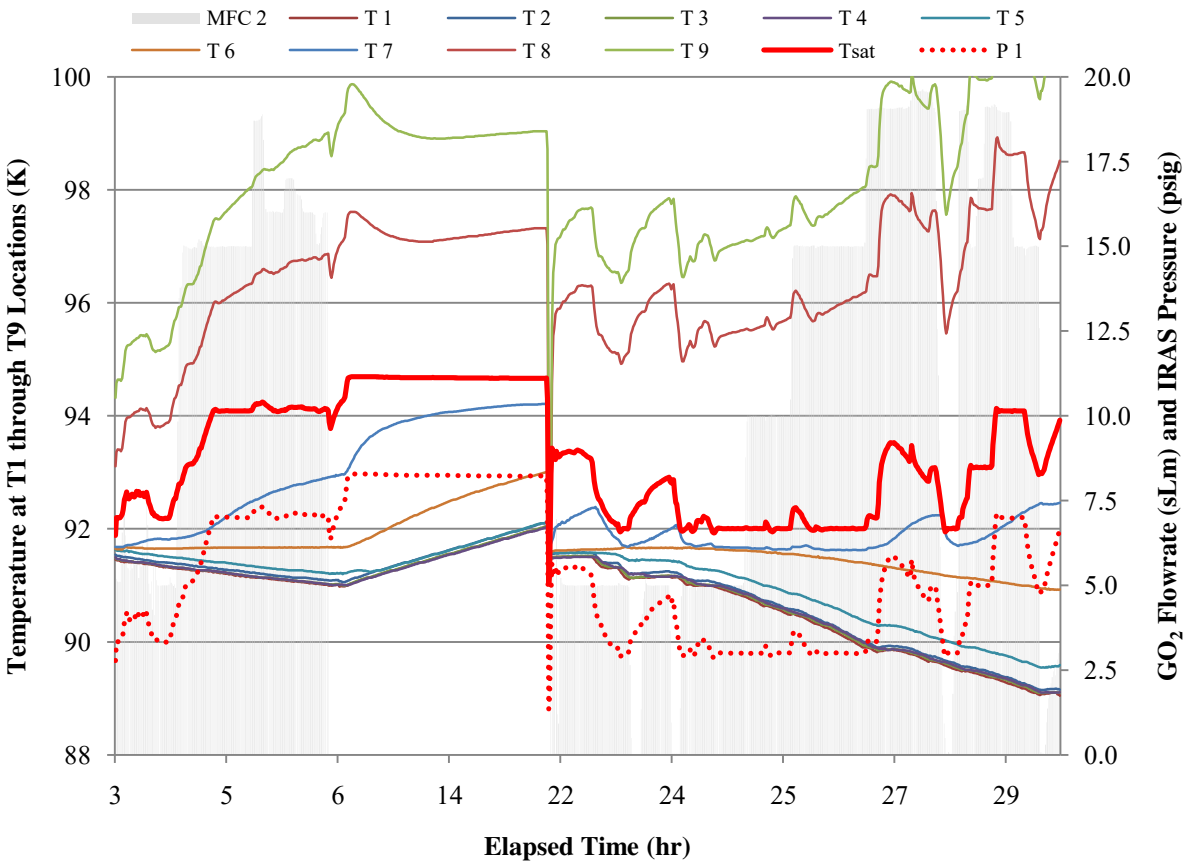

Figure 8: Liquid Temperature Profile During Top Fill Liquefaction

Figure 9 shows the ullage temperature data for liquefaction runs (3q, 3b, 3d, 3e, and 3r) that occurred on 9/1/10 and 9/2/10. Although, the ullage temperature remained thermally stratified throughout the entire test, the stratification increased as the gaseous oxygen flow rate increased. Although all temperature locations within the ullage increased linearly at a constant pressure and constant gaseous oxygen flow rate, the higher the temperature locations increased at a greater rate. Also, an increase in IRAS dewar pressure drives an instantaneous increase in the temperature at all locations within the ullage.

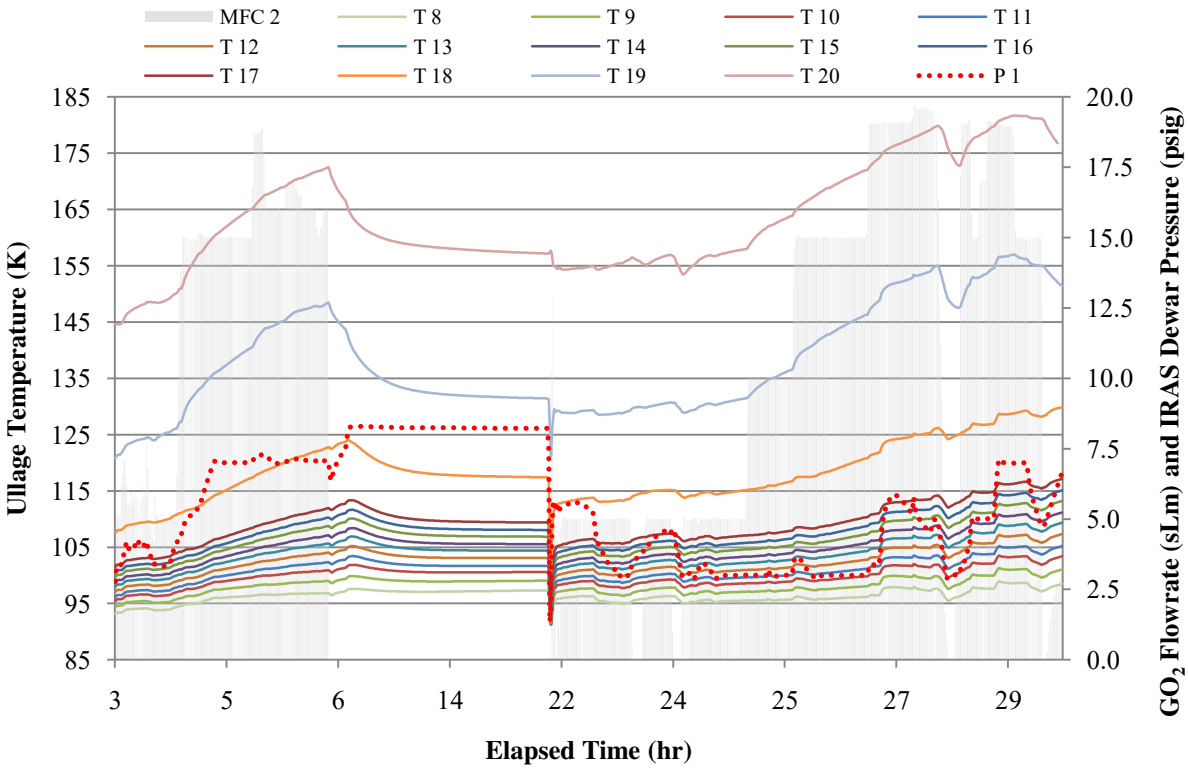

Figure 9: Ullage Temperature Profile During Top Fill Liquefaction

Figure 10 shows the results of the cooling requirement for Test Run 3a through Test Run 3r. The cooling requirement was calculated by Equation (25), where TC-24 and PT-26 provide the nitrogen inlet conditions and TC-27 provides the exit conditions. The cooling requirement increases as the oxygen condensation rate increases; the measured cooling requirement, as shown in Figure 10, agrees with anticipated cooling requirement increase of approximately 8.7 W/sL.

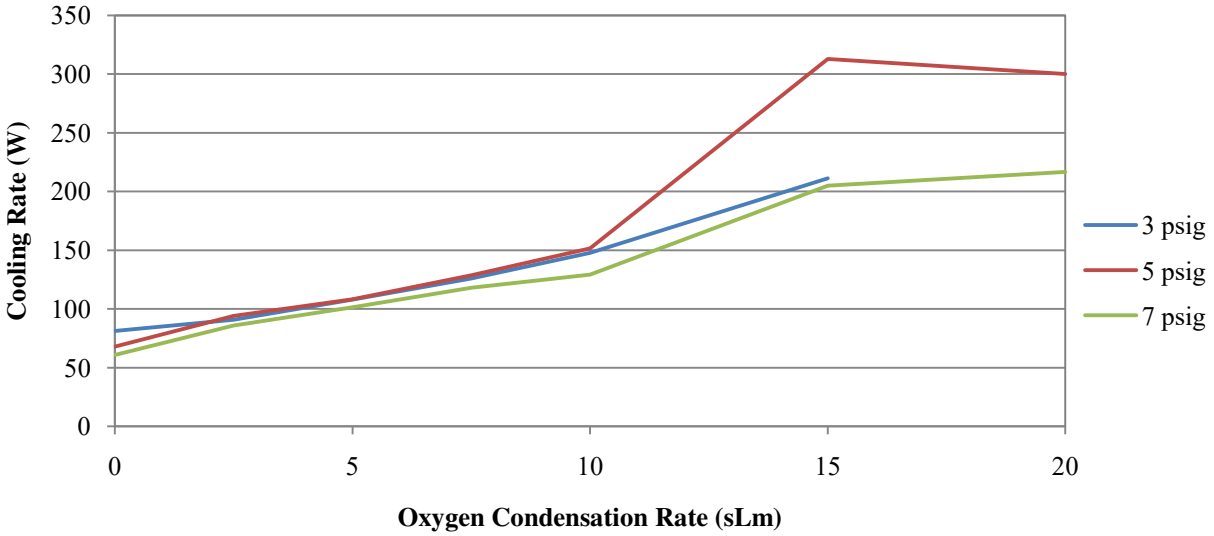

Figure 10: Cooling Requirement for Top Fill Liquefaction

Liquefaction-Top Fill Mathematical Model Results

Using temperature and pressure measurements during the test runs 3a through 3l, Equation (1), Equation (3), and Equation (6) estimate the oxygen condensation rate through direct contact. Figure 11, Figure 12, and Figure 13 show the results of the estimates provided by Equation (1), Equation (3), and Equation (6), respectively.

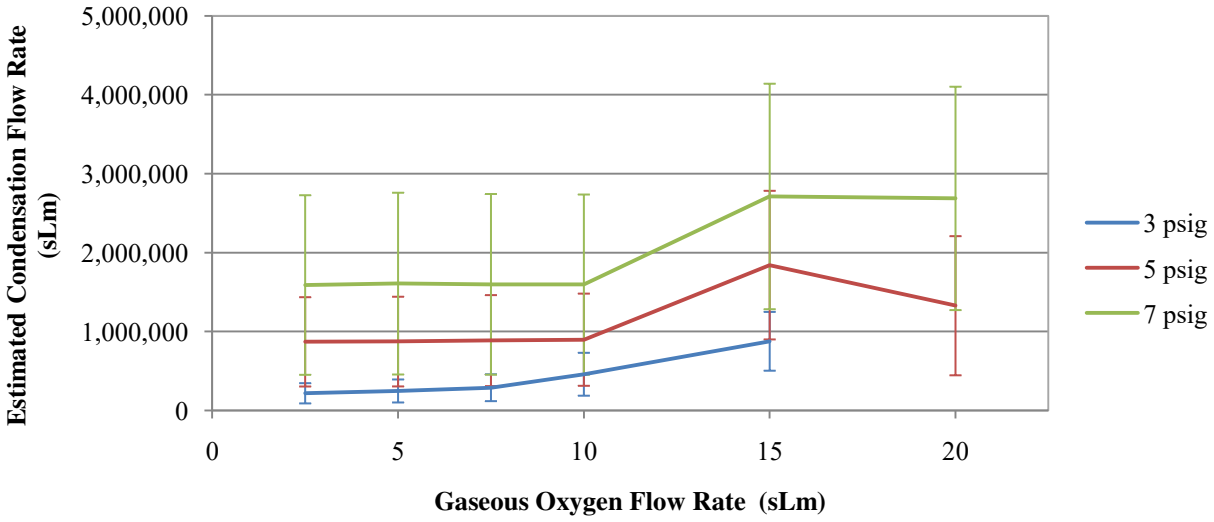

Figure 11: Equation (1) Results for Test Run 3a through Test Run 3r

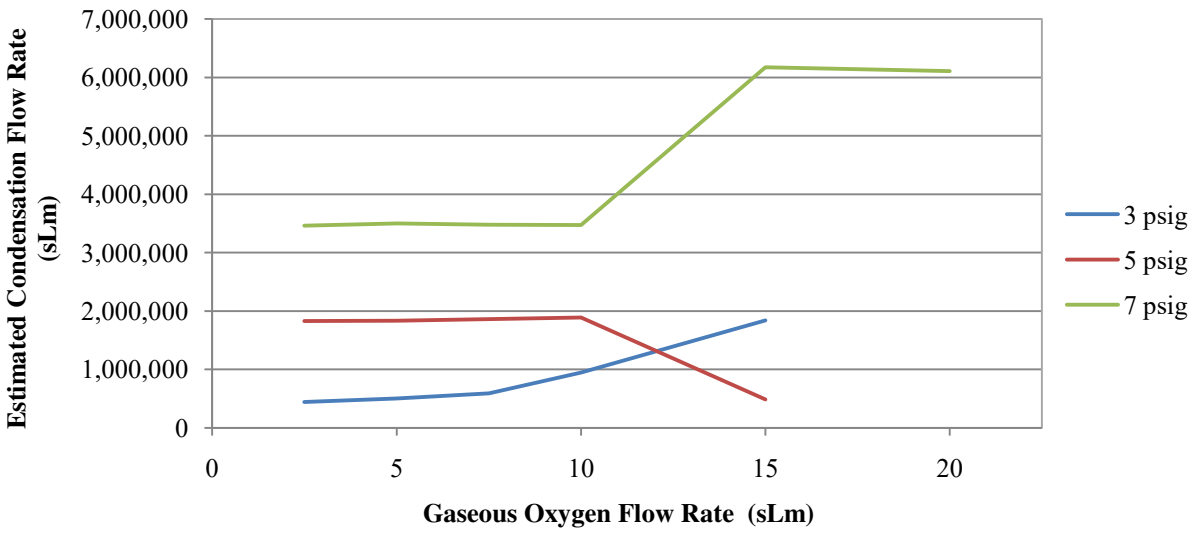

Figure 12: Equation (3) Results for Test Run 3a through Test Run 3r

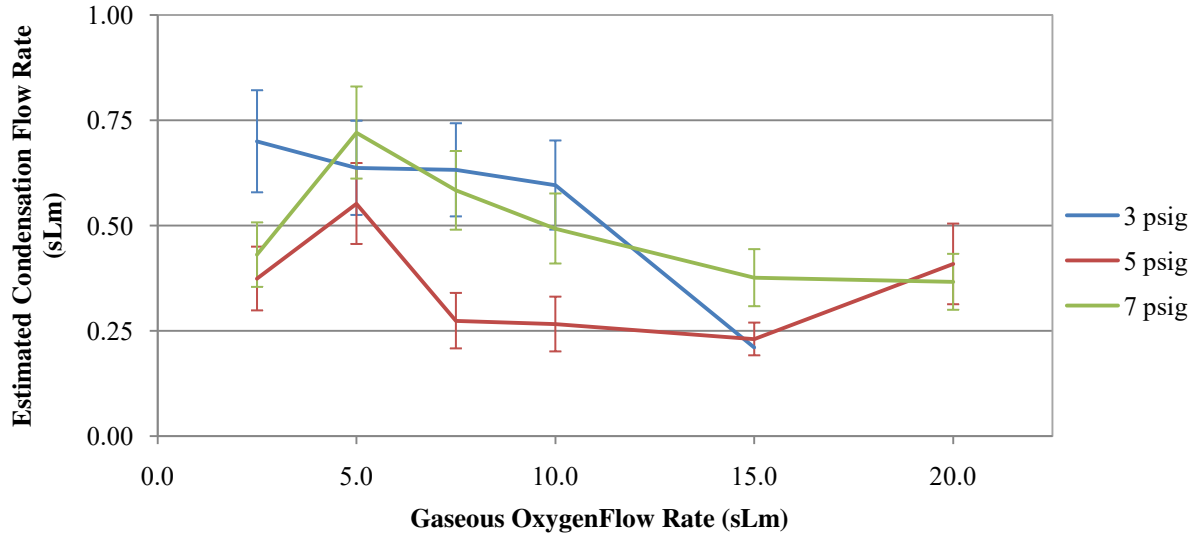

Figure 13: Equation (6) Results for Test Run 3a through Test Run 3r

Equation (27) determines the heat transfer coefficient as measured by the sensors within the IRAS dewar.

$$h = \frac{Q}{A\,\Delta T} = \frac{\dot{m}_{GO_2} h_{lv}}{A_{IRAS-CS}\,(T_{U1} - T_{L1})} \tag{27}$$

Figure 14 shows the results for heat transfer coefficient as determined by Equation (27). Figure 15 and Figure 16 show the results for Equation (2) and Equation (7), respectively.

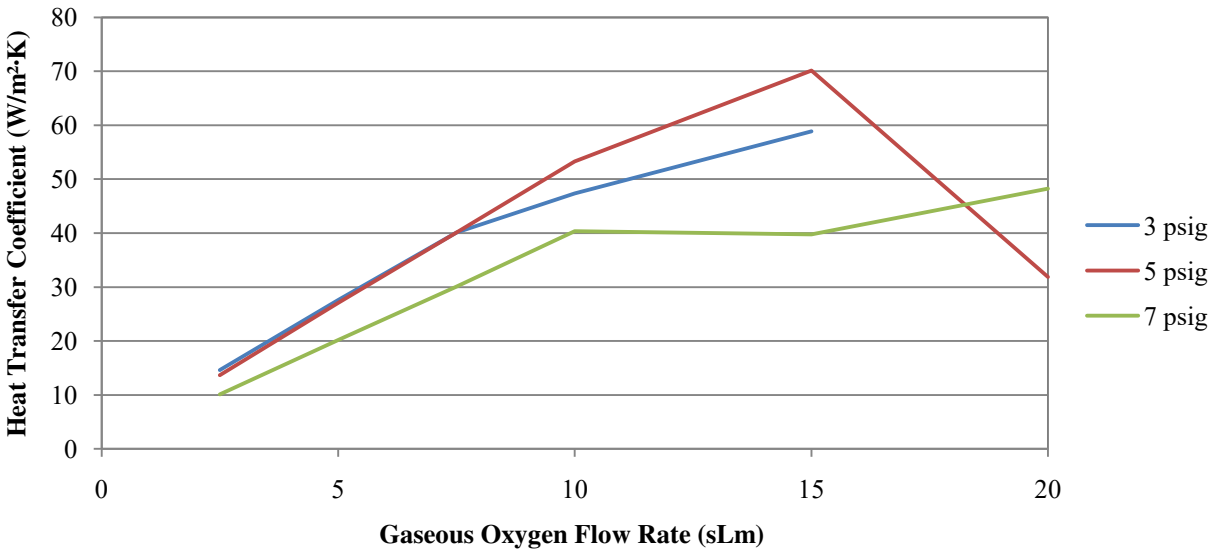

Figure 14: Measured Heat Transfer Coefficient for Test Run 3a through Test Run 3r

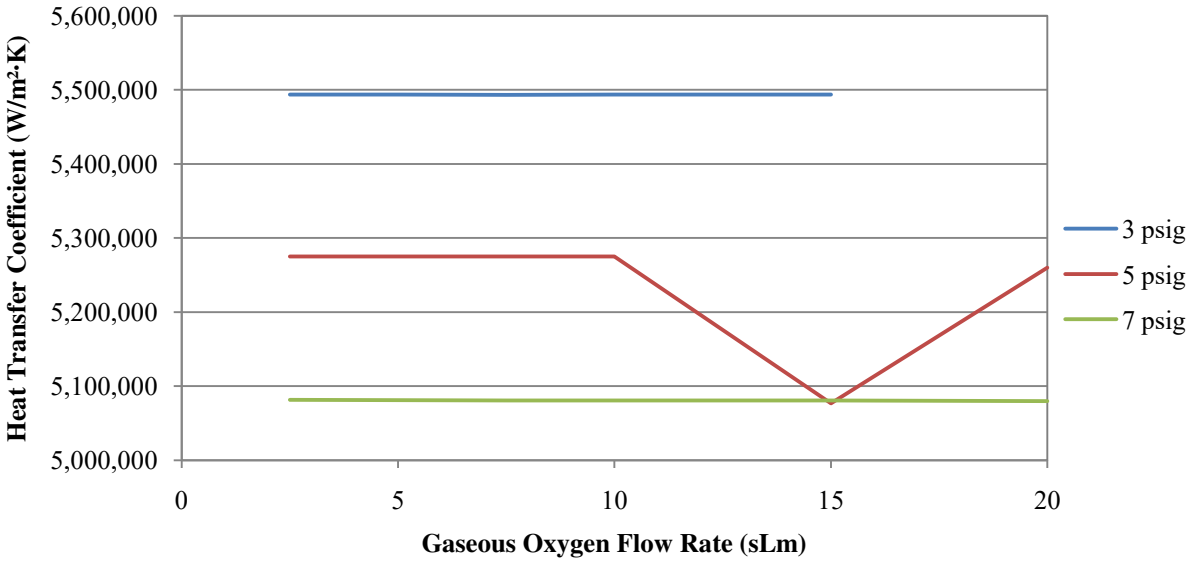

Figure 15: Equation (2) Results for Test Run 3a through Test Run 3r

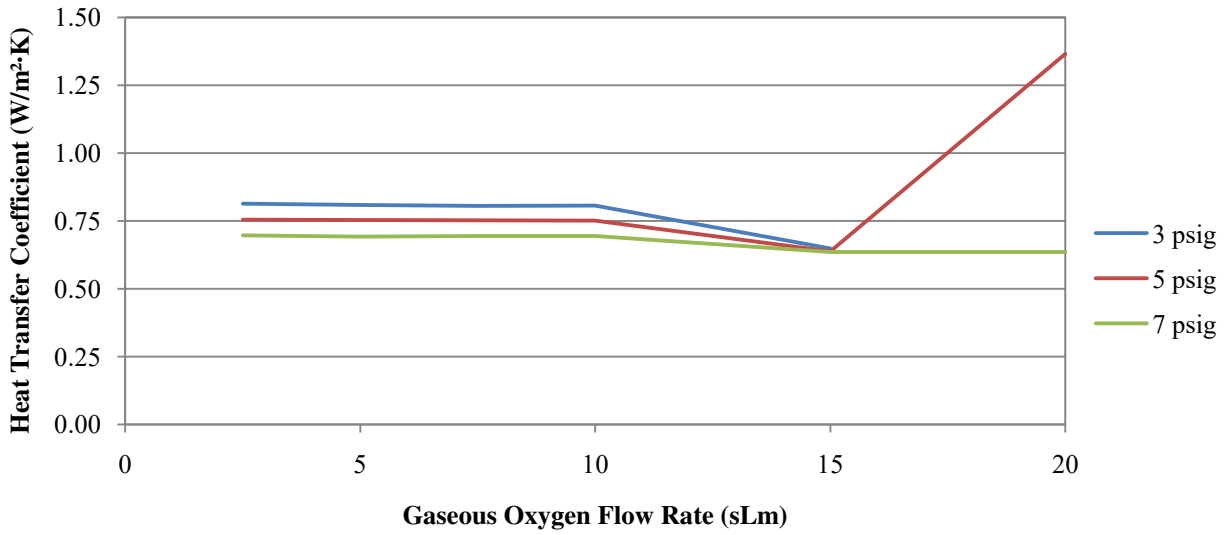

Figure 16: Equation (7) Results for Test Run 3a through Test Run 3r

Liquefaction-Top Fill Mathematical Model Discussion

Kinetic Theory Model Discussion

The results from both Equation (1) and Equation (3) are five to six orders of magnitude higher than the actual GO_2 flow rate. The two kinetic theory models, Equation (1) and Equation (3), depend on the temperature at the vapor-liquid interface. However, the temperature sensors on each side of the vapor-liquid interface are separated by a distance of four inches and a minimum temperature difference of 3K. The precision and accuracy of the temperature and pressure sensors also contribute to the lack of model verification.

Figure 17 and Figure 18 show a simple sensitivity analysis of Equation (1) with respect to small changes in pressure and temperature, respectively. The signal from the pressure transducer, PT-7, measuring the IRAS dewar pressure and the temperature sensors, T1 through T20, are recorded by the data acquisition program, Labview, to the ten-thousandths of a psig and K,

respectively. However, the error of the PT-7 and T1 through T8 are ±0.1 psig and ±0.5K, respectively. Thus, the instruments within the IRAS lack the precision and accuracy to confirm the equations derived from kinetic theory, which are Equation (1), Equation (2), and Equation (3).

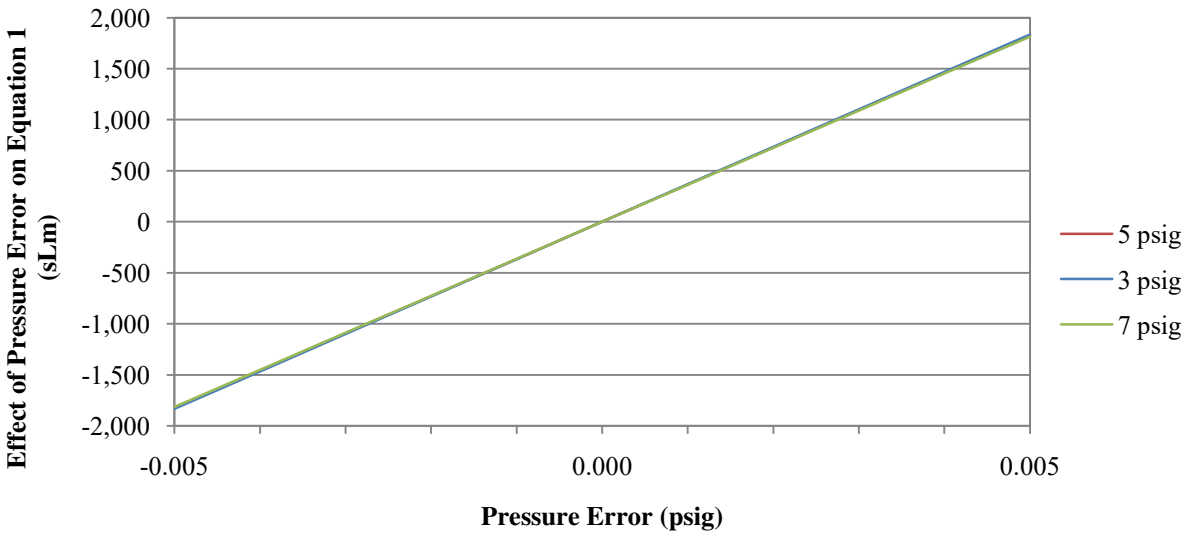

Figure 17: Sensitivity of Equation (1) With Respect to Small Changes in Pressure

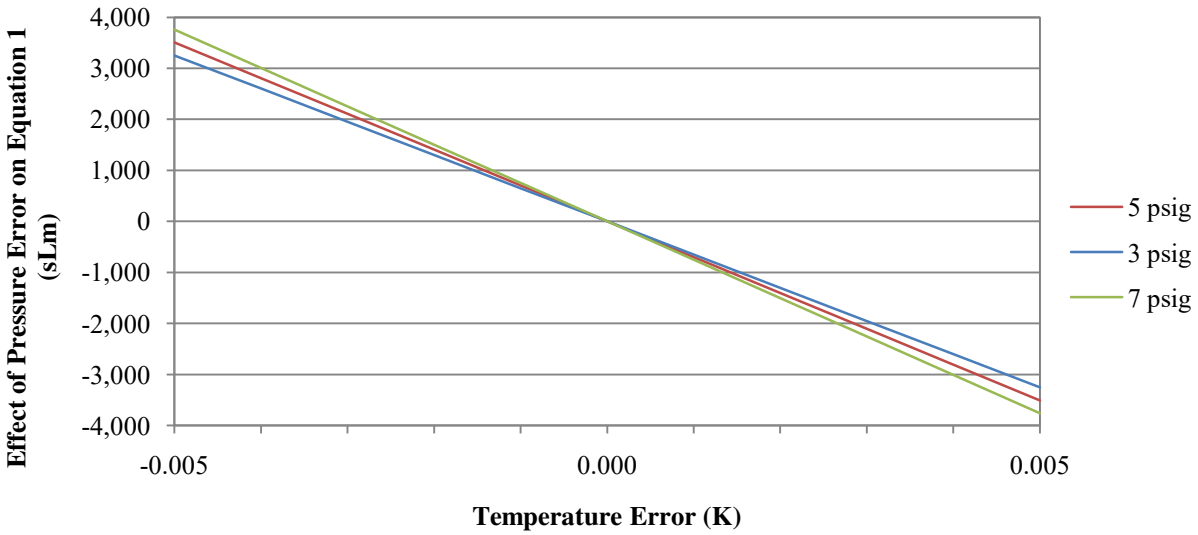

Figure 18: Sensitivity of Equation (1) With Respect to Small Changes in Temperature

Likewise, the results of the heat transfer coefficient using the Kinetic Theory Model, Equation (2), predicts a heat transfer coefficient approximately five orders of magnitude higher than results from Equation (27). Since Equation (1), Equation (2), and Equation (3) all use the Kinetic Theory Model, all three models predict suffer from the lack of precision and accuracy of the temperature and pressure sensors and result in predictions about five to six orders of magnitude higher actual result.

Cold Plate Model Discussion

The liquefaction prediction from Equation (6) was relatively constant across all GO_2 flow rates and about an order of magnitude lower than the actual gaseous oxygen flow rate. Likewise the Equation (7) results are about one or two orders of magnitude lower than the actual results from Equation (27). In an attempt to understand the reasons why the Cold Plate Model failed to predict the liquefaction rate, additional analysis of the IRAS dewar was performed. The actual GO_2 flow rate was measured by CV-18 and MCV-19, which was the flow rate of the gaseous oxygen entering the IRAS dewar. This gaseous oxygen could either (1) accumulate in the ullage represented by a pressure increase or decrease, (2) condense on the liquid nitrogen fill and vent tubes, or (3) condense on the liquid oxygen surface. APPENDIX E and APPENDIX A provide the methods and equations to determine the accumulation due to IRAS dewar pressure variations and possible condensation on the fill and vent tubes, respectively. Alternatively, Equation **(6)** did not consider an energy accumulation within the liquid layer between the heat exchanger and the vapor-liquid interface in the form of heat capacitance. APPENDIX E provides the equations and methods to determine the variation in heat capacitance within the liquid layer between the heat exchanger and vapor-liquid interface. Nevertheless, Figure 19 shows the above corrections

for the top-fill liquefaction for Test Run 3a-3e. As Figure 19 shows, there are still some unaccounted for liquefaction that occurs. Possible leaks downstream of the GO_2 flow controller could have been the reason for the unaccounted liquefaction, however, no leaks were determined about the IRAS dewar.

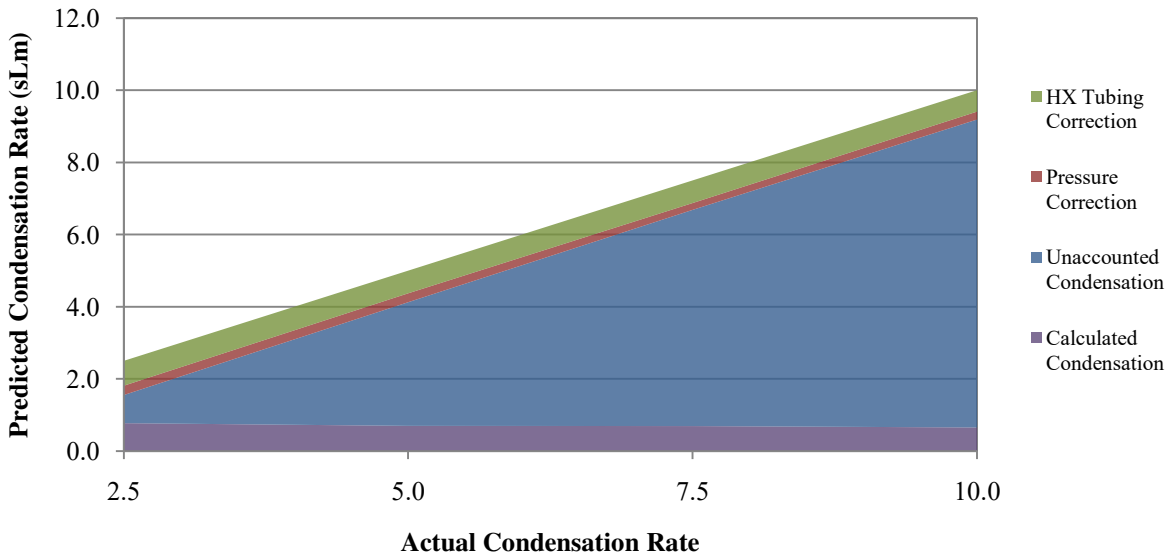

Figure 19: Correction to Equation (6) Prediction

Liquefaction – Bottom Fill

For Test Run 3aa through Test Run 3rr, gaseous oxygen enters the IRAS dewar through the hand valve, HV-1, to the liquid oxygen fill line. The liquid oxygen fill line is routed through the annular space and enters the inner tank near the top and runs vertically down the interior of the tank to the bottom as shown in Figure 20. The gaseous oxygen temperature is close to ambient as it enters the liquid oxygen fill line, however, the gaseous oxygen cools while flowing down the liquid oxygen fill line. The gaseous oxygen departs the liquid oxygen fill line as bubbles that flow upward through the liquid oxygen and into the ullage.

The gaseous oxygen within the bubbles continues to cool and collapse as the bubbles rise through the liquid oxygen. If insufficient cooling is provided to the bubble, the gaseous oxygen eventually reaches the liquid oxygen surface. The gaseous oxygen continues to rise into the ullage until the bubble reaches the isotherm equal to the temperature of the cooled gaseous oxygen as shown in Figure 20. The bottom fill takes advantage of the convection currents within the liquid to provide cooling to the gaseous oxygen bubble as well as placing the gaseous oxygen in the ullage at a distance closer to the liquid surface. Since the ullage remains conduction dominant, the shorter distance to the liquid surface allows for more efficient heat transfer than the top fill where the gaseous oxygen is placed at the top of the IRAS dewar.

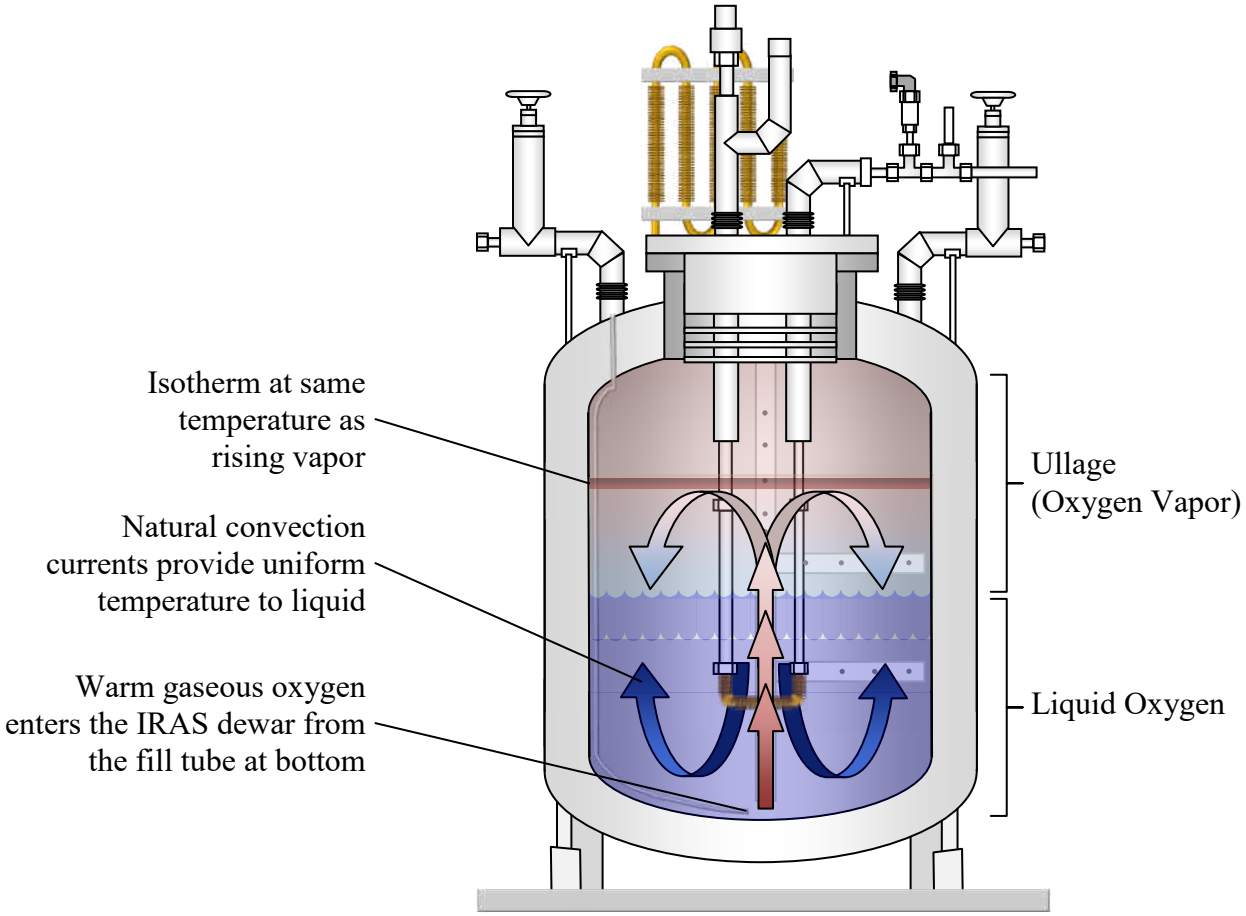

Figure 20: Convection Currents within IRAS Dewar during Bottom Fill Liquefaction

Figure 8 shows the liquid temperature data for liquefaction runs (3aa, 3bb, 3cc, 3dd, 3gg, 3hh, 3ii, 3mm, 3nn, 3oo, and 3pp) that occurred on 8/20/10 through 8/23/10. The bold red line represents the saturated temperature, which is calculated from Equation (112), and is located between the temperature sensors, T6 and T7. Thus, the vapor-liquid interface is located between 46 cm, the height of T6, and 53 cm, the height of T7. Once gaseous oxygen is introduced to the bottom of the IRAS dewar with active cooling through the IRAS heat exchanger, HX-9, the temperature at all positions within the liquid approach the saturation temperature. Also, no thermal stratification occurs within the liquid regardless of position above or below the heat exchanger.

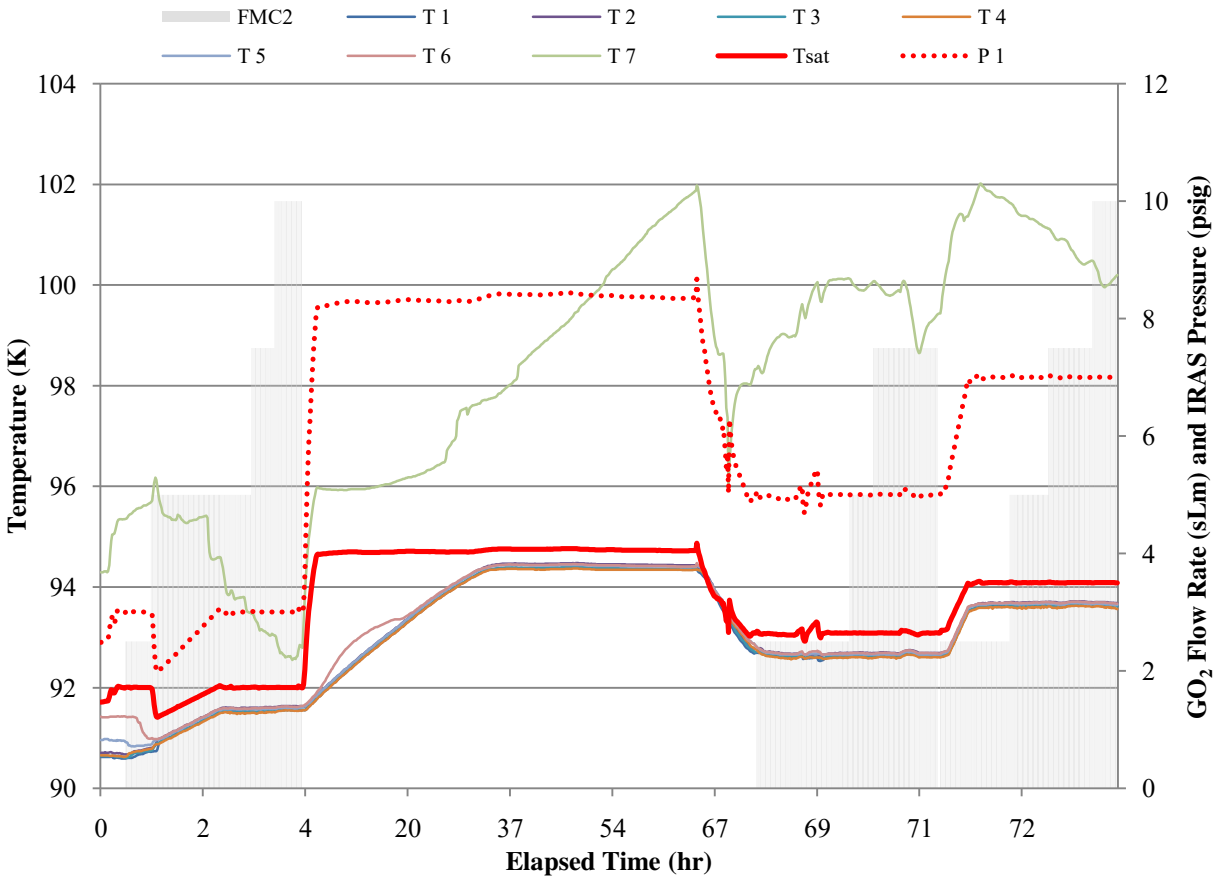

Figure 21: Liquid Temperature Profile During Bottom Fill Liquefaction

Figure 22 shows the ullage temperature data for liquefaction runs (3aa, 3bb, 3cc, 3dd, 3gg, 3hh, 3ii, 3mm, 3nn, 3oo, and 3pp) that occurred between 8/20/10 and 8/23/10. The ullage temperature remains thermally stratified throughout the entire test. Unlike the top-fill liquefaction results, the position temperature sensors along the upper boundary, were slower to react to the gaseous oxygen flow rate than the position temperature sensors at the lower boundary of the ullage, thus, the qualitative description of Figure 20 provides an accurate description of the bottom-fill liquefaction. As in general operation of the IRAS dewar, an increase in IRAS dewar pressure drives an instantaneous increase in the temperature at all locations within the ullage.

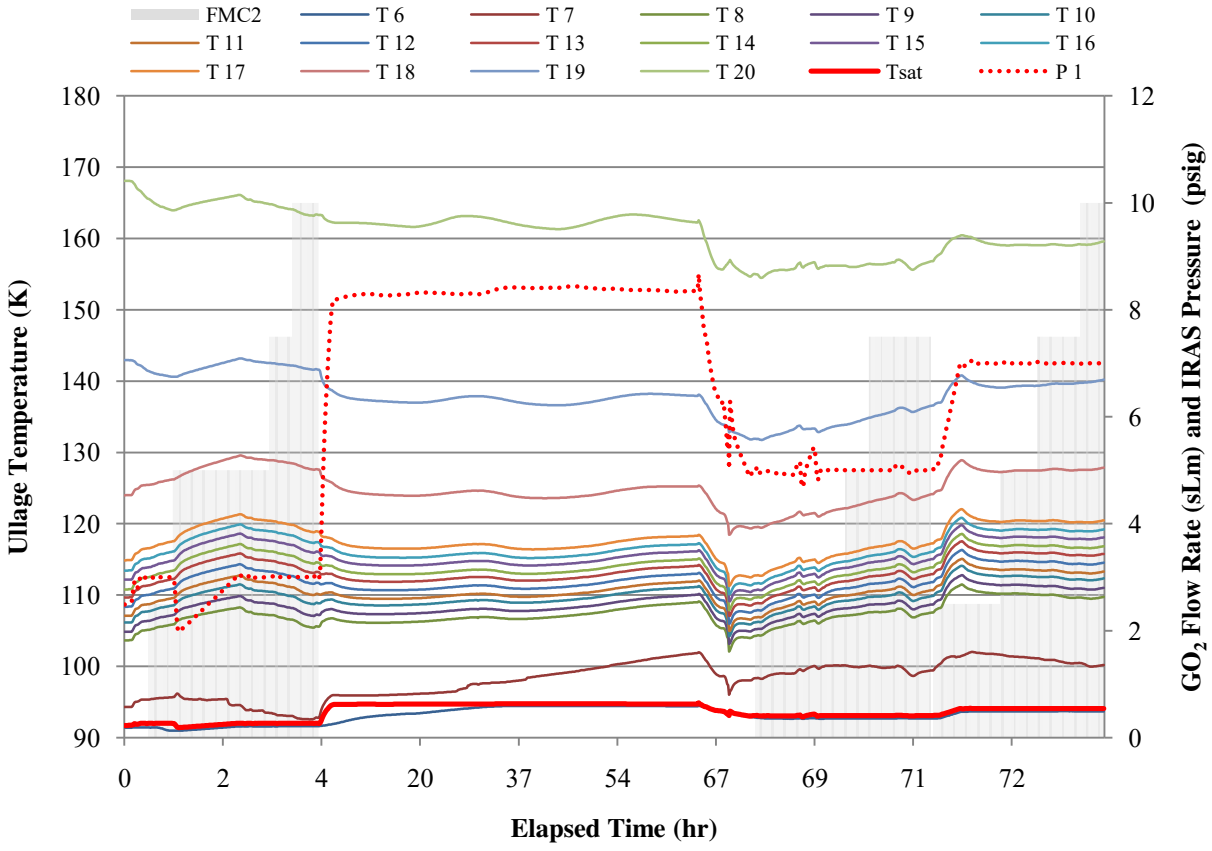

Figure 22: Ullage Temperature Profile During Bottom Fill Liquefaction

Figure 23 shows the results of the cooling requirement for Test Run 3aa through Test Run 3rr. The cooling requirement was calculated by Equation (25), where TC-24 and PT-26 provide the nitrogen inlet conditions and TC-27 provides the exit conditions. The cooling requirement presented in Figure 23 is corrected for the variation in heat capacitance within the liquid as calculated by Equation (111). As mentioned above in the top-fill liquefaction discussion, the cooling requirement should decrease as the IRAS dewar pressure increases. However, the cooling requirement, as presented in Figure 23, does not show an explicit trend with respect to cooling requirement and pressure. Nevertheless, the cooling requirement increases as the oxygen condensation rate increases; the measured cooling requirement, as shown in Figure 23 agrees with the 8.7 W/sL.

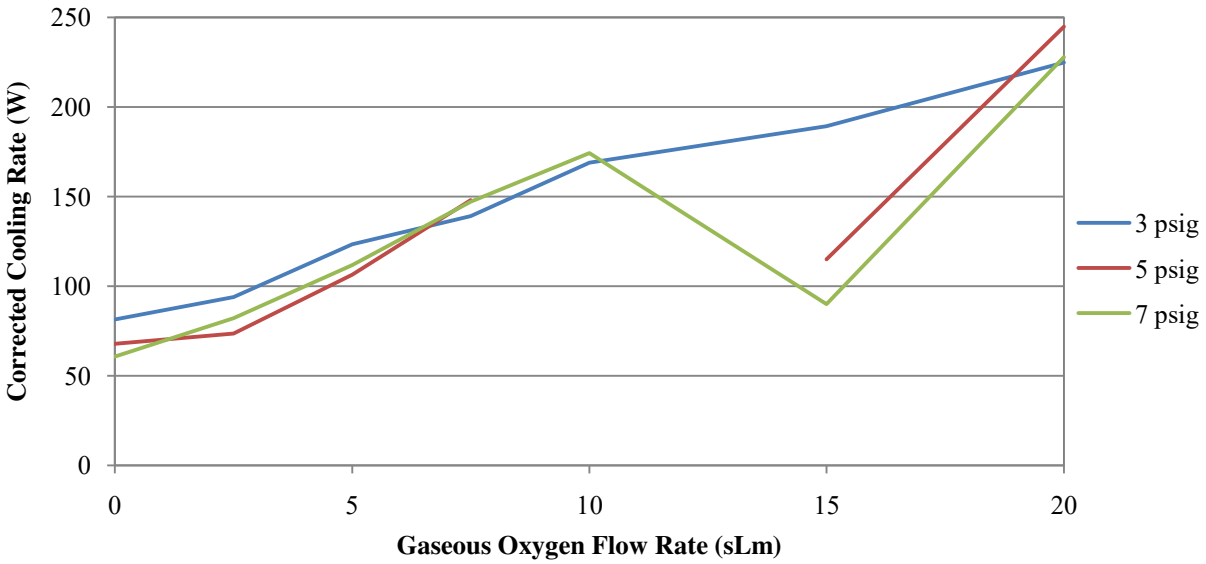

Figure 23: Cooling Requirement for Bottom Fill Liquefaction

Liquefaction-Bottom Fill Mathematical Model Results

Figure 24 shows the results of Equation (9), and Figure 25 shows the results of Equation (89). The GO_2 mass flow rate in Equation (89) is predicted by Cold Plate Model, Equation (6). The GO_2 mass flow rate predicted by the Kinetic Theory Model was not used in Equation (89)

because of the inability of precision from the sensors as discussed above. Figure 26 shows the results of Equation (27) to show the measurement of the heat transfer coefficient during the bottom fill liquefaction. Figure 27 shows the results of Equation (7) to predict the heat transfer coefficient during the bottom fill liquefaction.

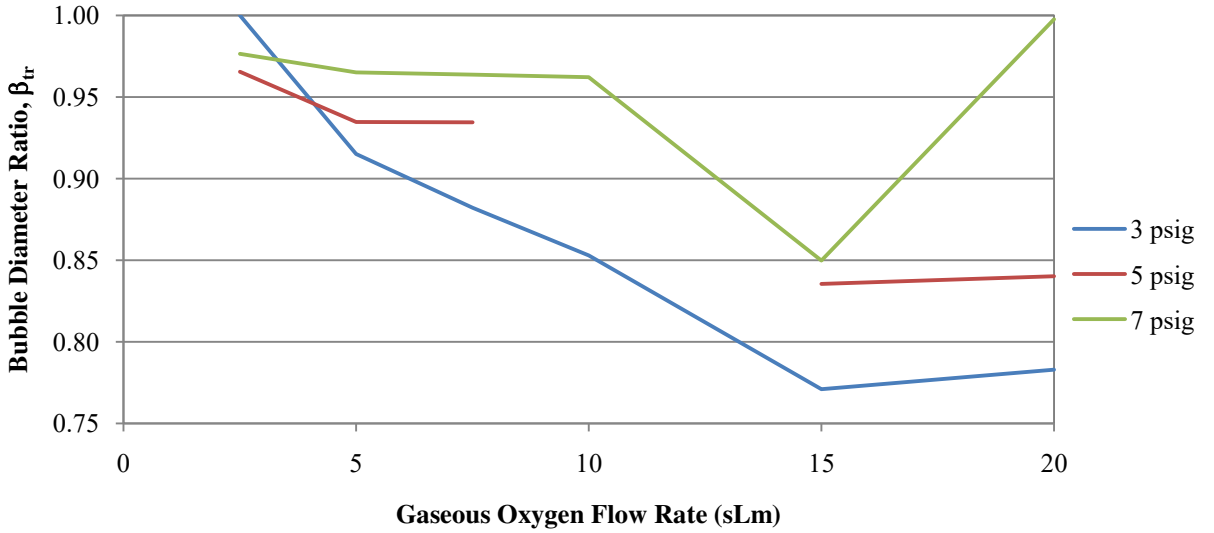

Figure 24: Bubble Collapse During Bottom Fill Liquefaction

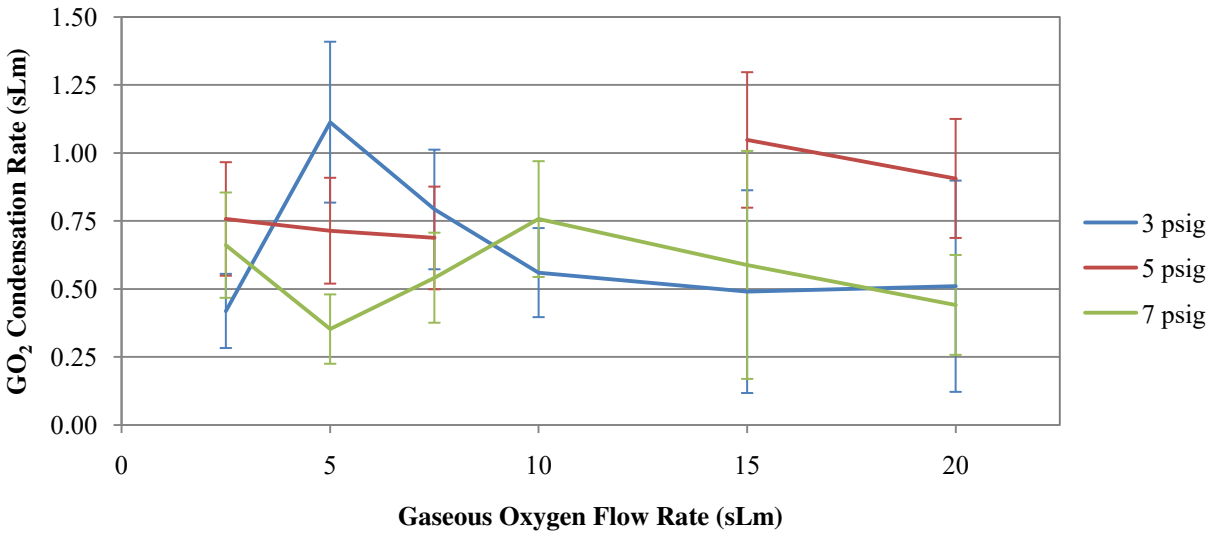

Figure 25: Equation (89) Results for Test Run 3aa through Test Run 3rr

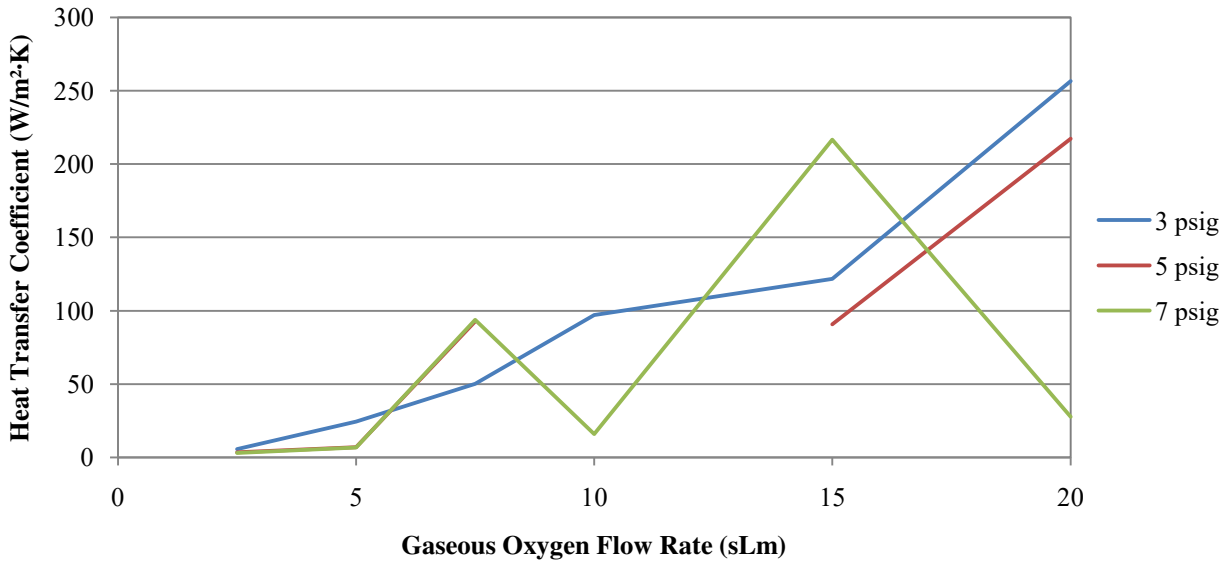

Figure 26: Measured Heat Transfer Coefficient for Test Run 3aa through Test Run 3rr

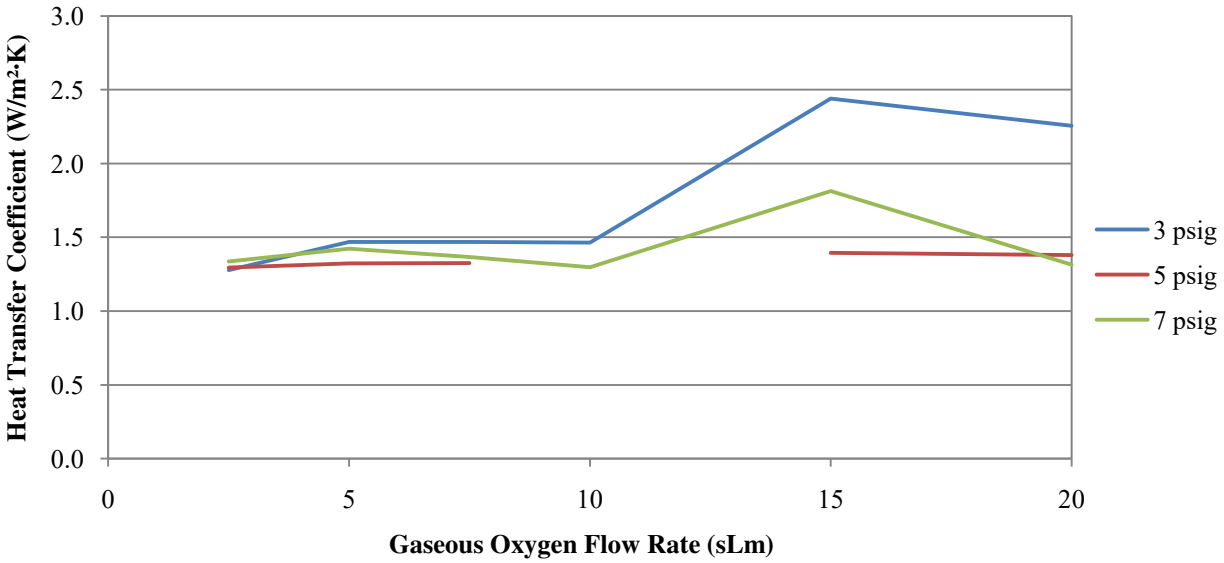

Figure 27: Equation (7) Results for Test Run 3aa through Test Run 3rr

Liquefaction-Bottom Fill Mathematical Model Discussion

The experimental apparatus could not determine the quantity of gaseous oxygen that condensed in the liquid oxygen. In general from the results of Equation (9), the condensation from the bubble increases as the gaseous oxygen flow rate increases. The Equation (9) results and Equation (89) results resembled the Equation (6) results from the top fill liquefaction section

with respect to order of magnitude and no observable trend. Likewise the heat transfer coefficient from the bottom fill liquefaction and top fill liquefaction showed similar results. The liquefaction rate and heat transfer coefficient models were discussed in the top fill liquefaction section and any further discussion would be redundant.

As Equation (89) predicts, the amount of oxygen liquefied from the bubble collapse should always be greater than Liquefaction by Ullage Collapse due to the convection heat transfer. However, no difference between the bottom fill liquefaction and top fill liquefaction was observed.

Densification

Densification Below Heat Exchanger

Densification Below Heat Exchanger Mathematical Model Results

The subcooling and densification data as presented in Figure 28 and Figure 29 was taken during liquefaction test runs, Test Run 4a through Test Run 4c. As mentioned in CHAPTER TWO, the heat transfer within the liquid is modeled by transient heat conduction analysis. The liquid below the heat exchanger is an average temperature across the entire height of liquid below the heat exchanger. The summation of the Equation (16) to n=1500, as opposed to n=∞. The position of the IRAS heat exchanger remained stationary throughout the entire test at the T5 position or 15 inches (0.381 m) above the bottom of the IRAS dewar. To determine θ_i, the surface temperature of the heat exchanger and the initial temperature of the liquid were determined by an average of TC-23 over the entire test period and an average of the T1 through T4 initial observations, respectively.

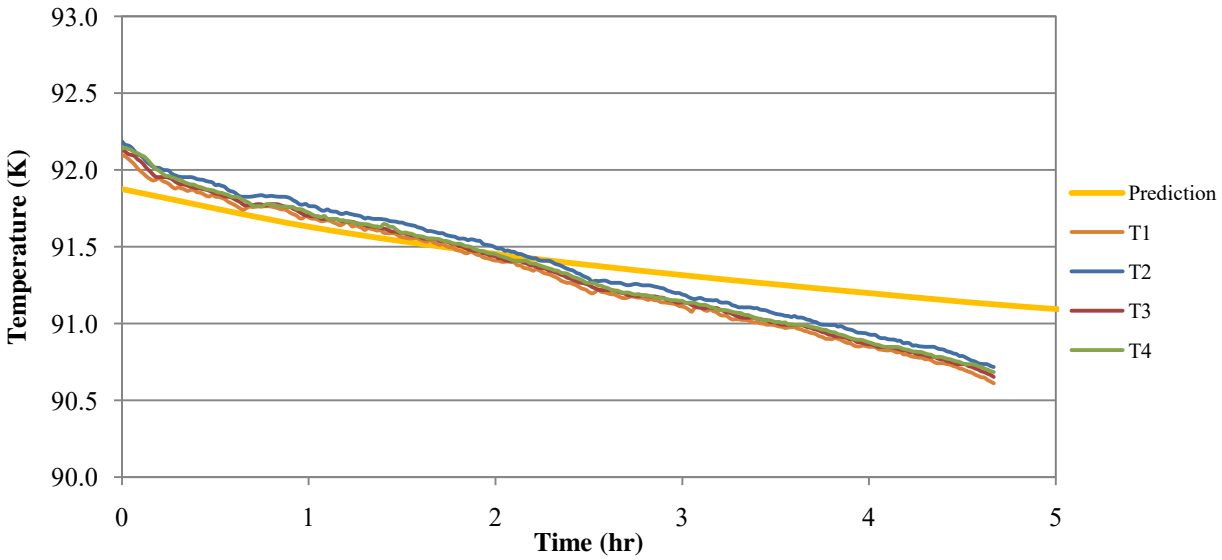

Figure 28: Temperature Profile Below Heat Exchanger of 8/19/10 Test

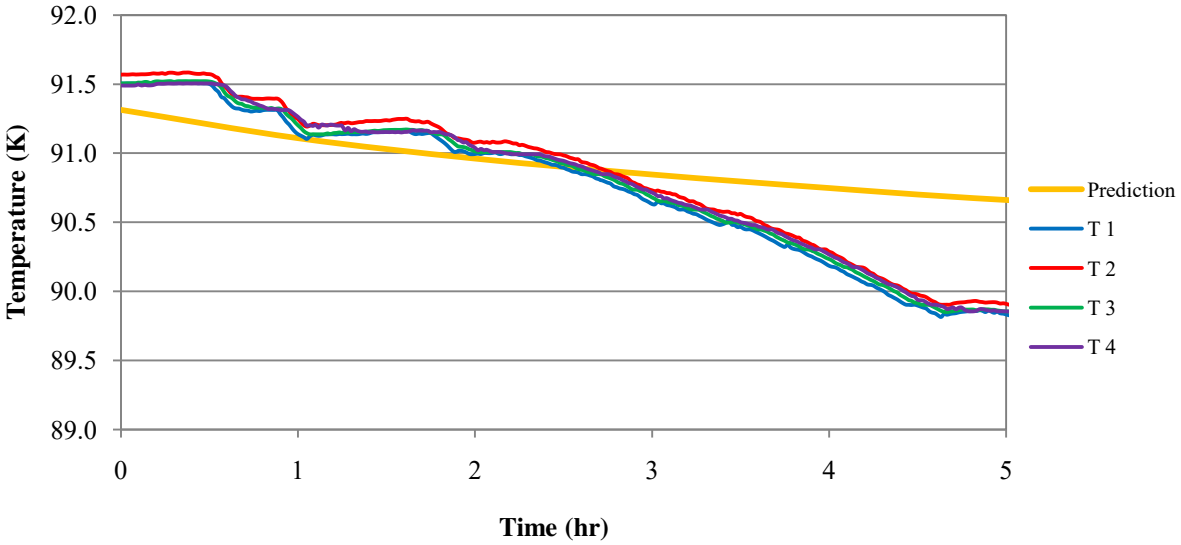

Figure 29: Temperature Profile Below Heat Exchanger of 9/2/10 Test

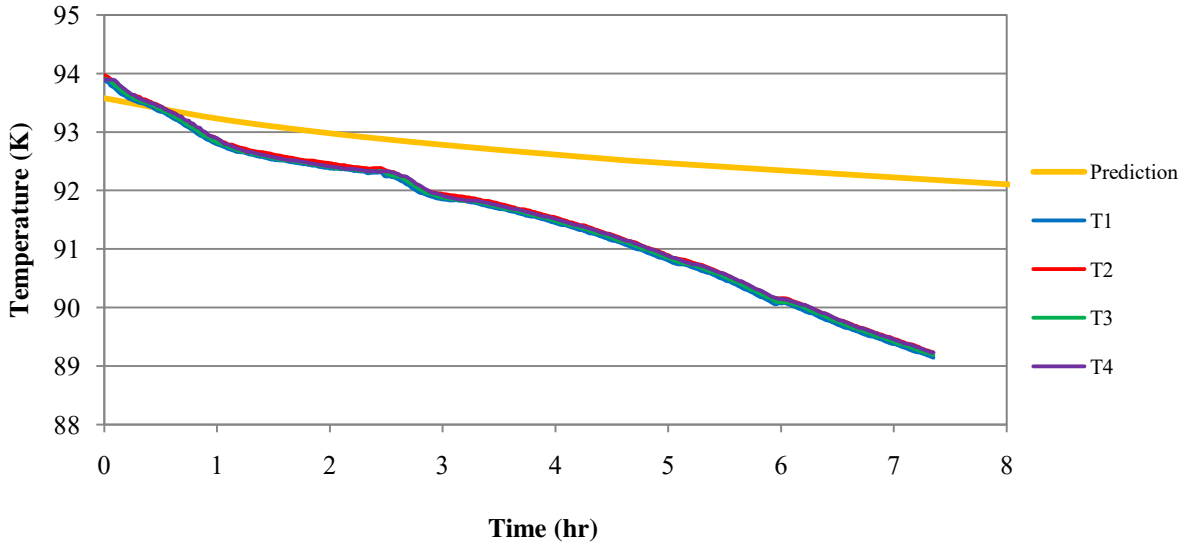

Figure 30: Temperature Profile Below Heat Exchanger of 9/24/10 Test

Densification Below Heat Exchanger Mathematical Model Discussion

The average of the transient heat conduction analysis provided a good prediction of the densification rate of liquid oxygen below the heat exchanger. The transient one-dimensional heat conduction analysis neglected the heat flux through the IRAS dewar walls. The transient

heat conduction assumes uniform temperature not only but vertically but also horizontally, which is confirmed by the temperature profile of T21 through T24.

Densification Above Heat Exchanger

Densification Above Heat Exchanger Mathematical Model Results

The subcooling and densification data as presented in Figure 31 and Figure 32 shows the liquid temperature data above the heat exchanger during the same timeframe as Figure 28 and Figure 29. As mentioned in CHAPTER TWO, the heat transfer within the liquid is modeled by transient heat conduction analysis of Equation (15). For predicting the temperature with respect to height and time, the summation of the Equation (15) was from n = 1 to n=1500, as opposed to n=∞. Although, the position of the IRAS heat exchanger remained stationary throughout the entire test at the T5 position or 15 inches (0.381 m) above the bottom of the IRAS dewar, the total height of the liquid was determined by the method described in APPENDIX E. The constant temperature at the upper boundary is the saturated temperature of the liquid as determined by Equation (112) and Equation (113). The constant temperature of the heat exchanger surface at the lower boundary is determined by an average of the TC-3 observations over the test period. The constant, I_i, is determined by Equation (93) and other the other constraints of Equation (15) are noted in each figure.

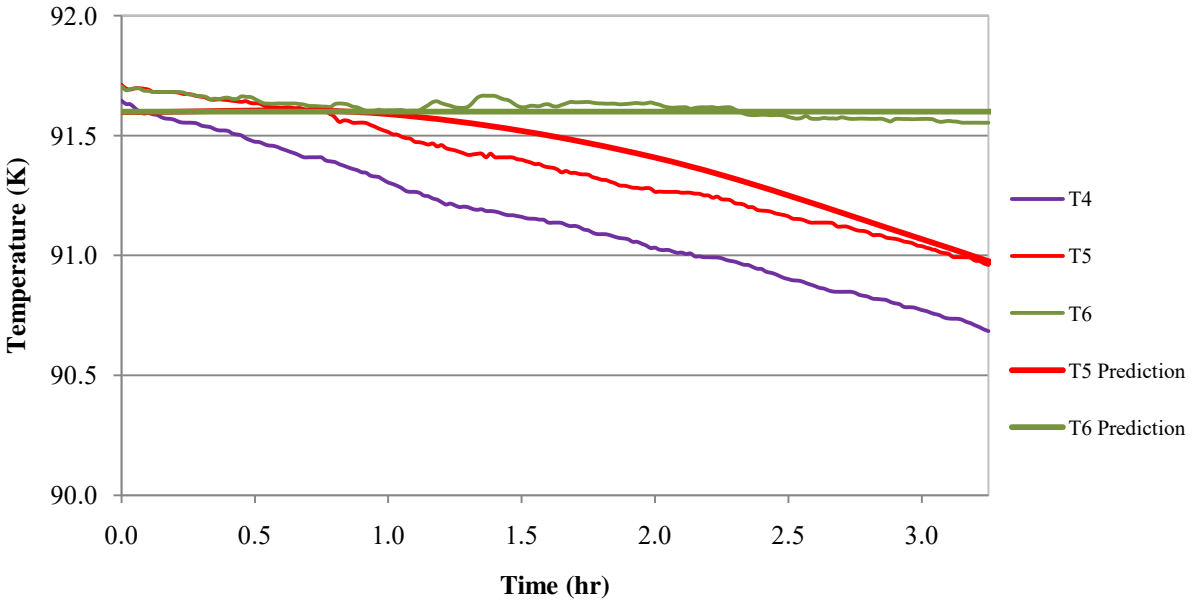

Figure 31: Temperature Profile of Liquid Above Heat Exchanger for 8/19/10 Test

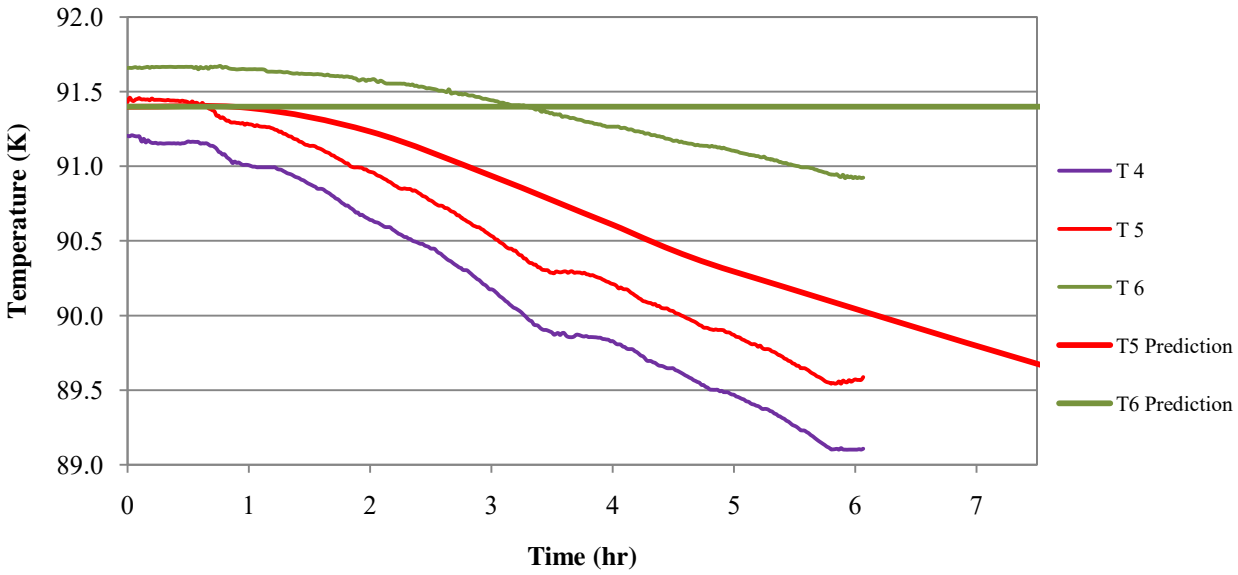

Figure 32: Temperature Profile of Liquid Above Heat Exchanger for 9/2/10 Test

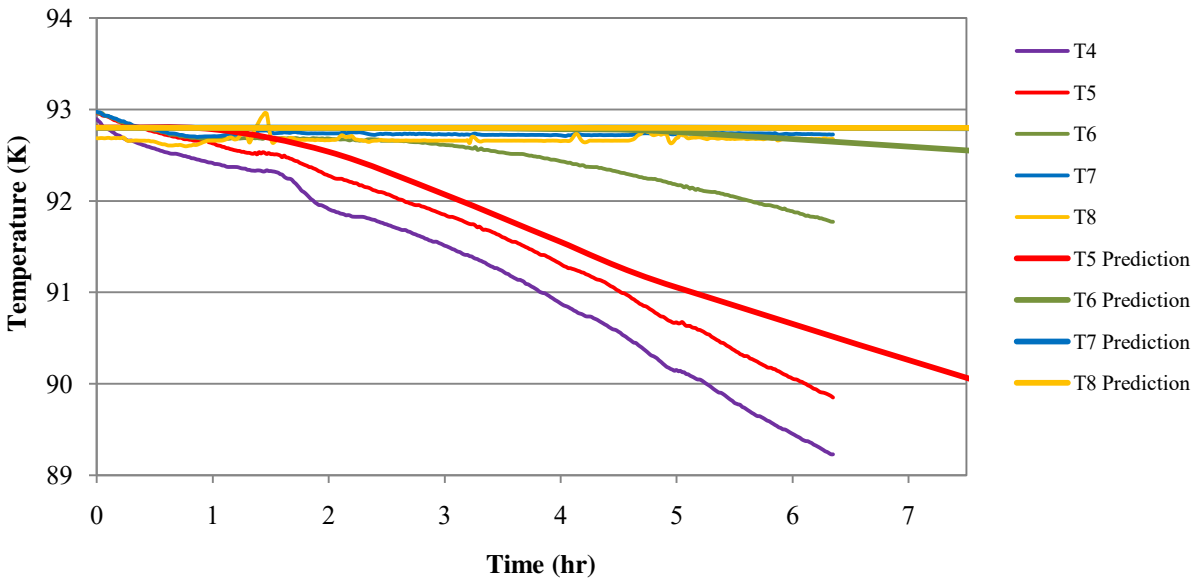

Figure 33: Temperature Profile of Liquid Above Heat Exchanger for 9/24/10 Test

Densification Above Heat Exchanger Mathematical Model Discussion

The transient heat conduction analysis provided a good prediction of the densification rate of liquid oxygen above the heat exchanger. The transient one-dimensional heat conduction analysis neglected the heat flux through the IRAS dewar walls. The transient heat conduction assumes uniform temperature horizontally, which is confirmed by the temperature profile of T25 through T28. The transient heat conduction analysis predicted by Equation (15) assumes the upper boundary remains constant throughout the entire densification test runs. However, the IRAS dewar pressure varied throughout the densification test runs, thus, the saturation temperature, or upper boundary temperature, varies throughout the densification test runs.

If the ullage is pressurized with a non-condensable, such as helium, the densification rate of the liquid above the heat exchanger should show similar results as when the ullage remains at constant pressure with gaseous oxygen. The liquid oxygen at the vapor-liquid interface begins the densification at the boiling point

Combined Densification Model Discussion

Both mathematical models for the densification of liquid oxygen have the same boundary condition at the heat exchanger. However, an average of Equation (16) is used to model the liquid oxygen below the heat exchanger to account for the convection. Using the average of Equation (16) yields a temperature discontinuity at the heat exchanger as shown in Figure 34. Figure 34 also shows the combination of the two mathematical with a continuous temperature distribution. The continuous temperature distribution is based on convection principle that the density at any position must be less than the density at all lower vertical positions. As Figure 51 shows, liquid oxygen density increases as the temperature decreases across the entire liquid range, from the triple point to the critical point. Thus, the convection principle implies that the temperature at any position must be greater than or equal to the temperature at all lower vertical positions. Figure 34 assumes a heat exchanger temperature location at T5, a heat exchanger temperature at 83K, and a liquid oxygen initial temperature of 94K.

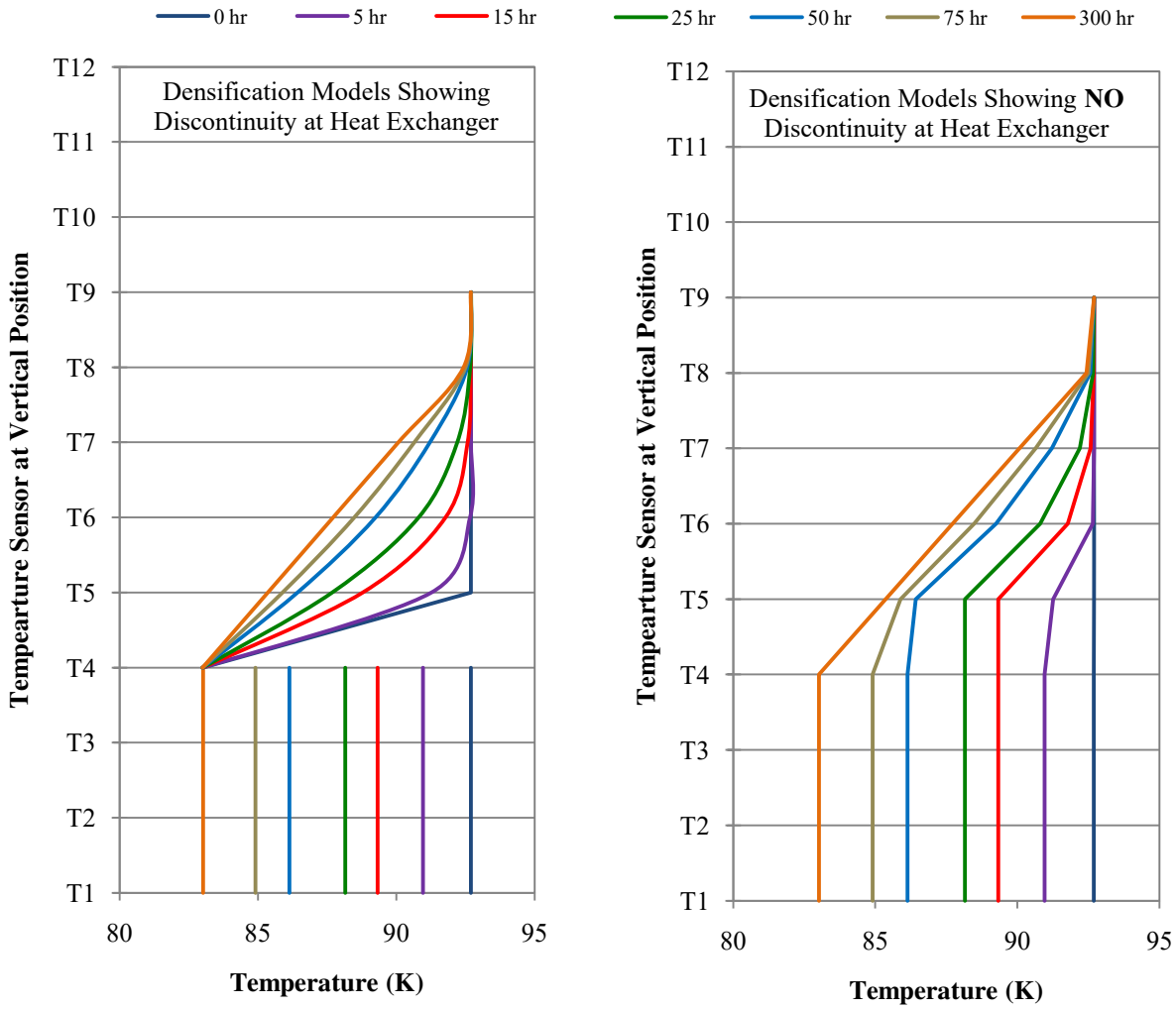

Figure 34: Combination of Densification Models

Figure 35 is from the 9/24/10 densification test. The densification test was run at a constant pressure of 5 psig, however the first hour was dedicated to reducing the IRAS pressure from 8 psig to the intended test pressure of 5 psig. The temperature remains uniform throughout the liquid, independent of vertical position for the first hour, or until the test pressure was achieved and setting a constant temperature at the upper boundary as described in CHAPTER TWO and APPENDIX D.

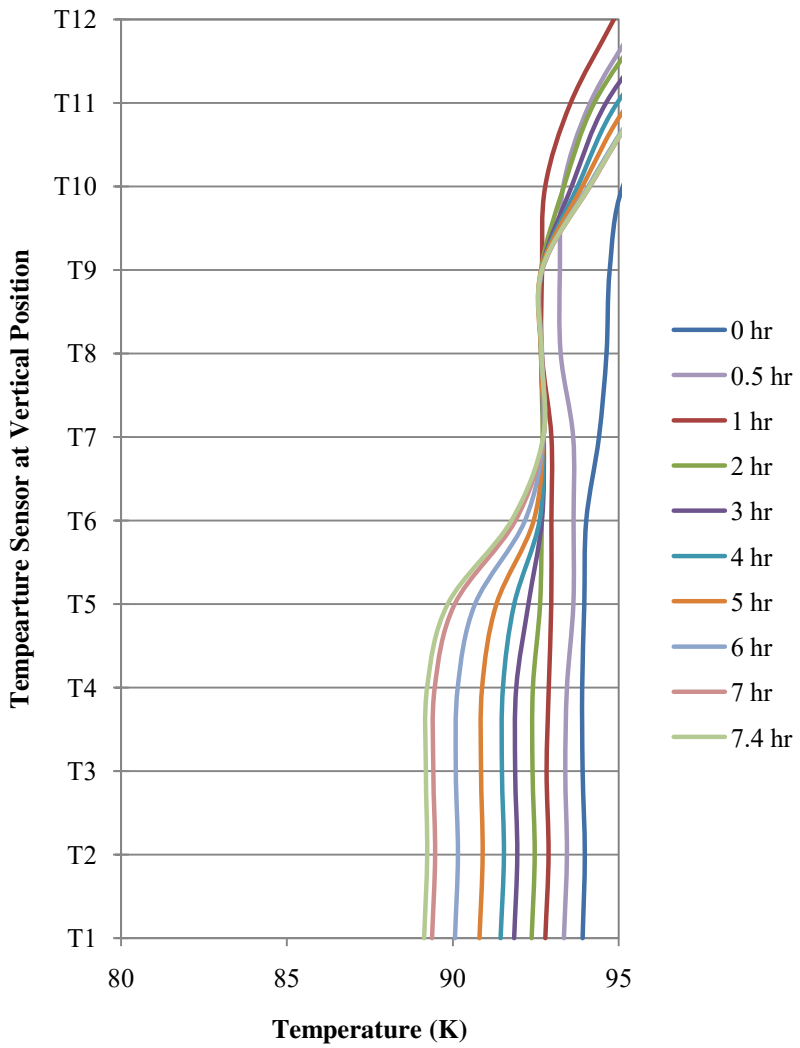

Figure 35: Vertical Temperature Profile at Given Time Intervals for 9/24/10 Test

CHAPTER FIVE: CONCLUSIONS AND FUTURE WORK

Conclusions

- Experimental results could not verify Kinetic Theory Model for direct contact condensation due to lack of precision and accuracy of the pressure and temperature sensors, and perhaps the fixed locations of the temperature sensors. Results from the Kinetic Theory Model overestimated the observed liquefaction rate and calculated heat transfer coefficient by five to six orders of magnitude.

- Experimental results could not verify Cold Plate Model for direct contact condensation. Results from the Cold Plate Model underestimated the observed liquefaction rate and calculated heat transfer coefficient by one to two orders of magnitude.

- Experimental results could not verify the Bubble Collapse model, nor that bottom fill liquefaction is a more efficient manner for liquefaction as predicted by Equation (89).

- Experimental results verified the qualitative models for Top Fill Liquefaction, Figure 7, and Bottom Fill Liquefaction, Figure 20.

- Experimental results verified the transient heat conduction model, Equation (15), applied to the liquid above the IRAS heat exchanger during active cooling and gaseous oxygen flowing into the ullage to maintain the IRAS at a constant pressure.

- The transient heat conduction model, Equation (16), provided reasonable prediction of the densification rate. The liquid below the heat exchanger is not thermally stratified and the temperature is estimated by averaging the temperature across all positions in Equation (16).

Future Work

Liquefaction

Future liquefaction work should test the Cold Plate Model with respect to liquid height above the heat exchanger. Figure 36 shows the predictions of the Cold Plate Mode, Equation (6), with respect to initial liquid height and time equal to zero.

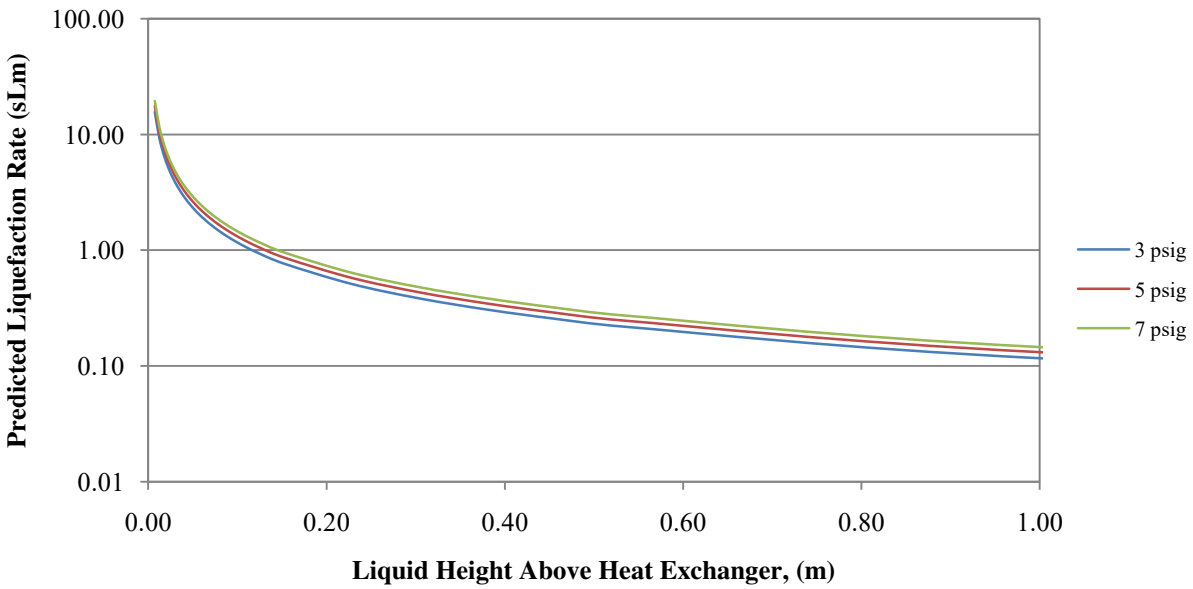

Figure 36: Predicted Liquefaction Rate from Equation (6) with Respect to Liquid Height

Densification

Future densification work should test the densification models at sub-atmospheric pressure and with a non-condensable pressurant to maintain the constant pressure in the ullage. If the ullage

pressure goes sub-atmospheric, then no constant pressure is maintained in the ullage, thus, the upper boundary above the heat exchanger is not maintained at a constant temperature. In this case, the average of Equation (16) should be used to model the entire liquid, above and below the heat exchanger. If a non-condensable, such as gaseous helium, is used to maintain constant ullage pressure, then the liquid should be modeled as discussed in CHAPTER TWO. Although the ullage gas does not condense, the liquid at the vapor-liquid interface absorbs heat from ambient and ullage until it reaches the boiling point. Thus, the top boundary of the liquid is still held at constant temperature when the ullage is held at constant pressure, regardless of the ullage constituents.

APPENDIX A: HEAT TRANSFER ANALYSIS

Heat Transfer Analysis Through Teflon Insulation

The vertical tubing carrying the liquid nitrogen to the heat exchanger and the vaporized gaseous nitrogen from the heat exchanger needs to be insulated to minimize heat transfer into the ullage. It is desired to optimize the insulation thickness before specifying the design requirements for the insulation. An optimum insulation thickness, or heat transfer minimum, does not exist for radial systems, but a heat transfer maximum can exist [18]. To ensure that the insulation thickness inhibits heat transfer, the heat transfer through the fill and vent tubes are analyzed.

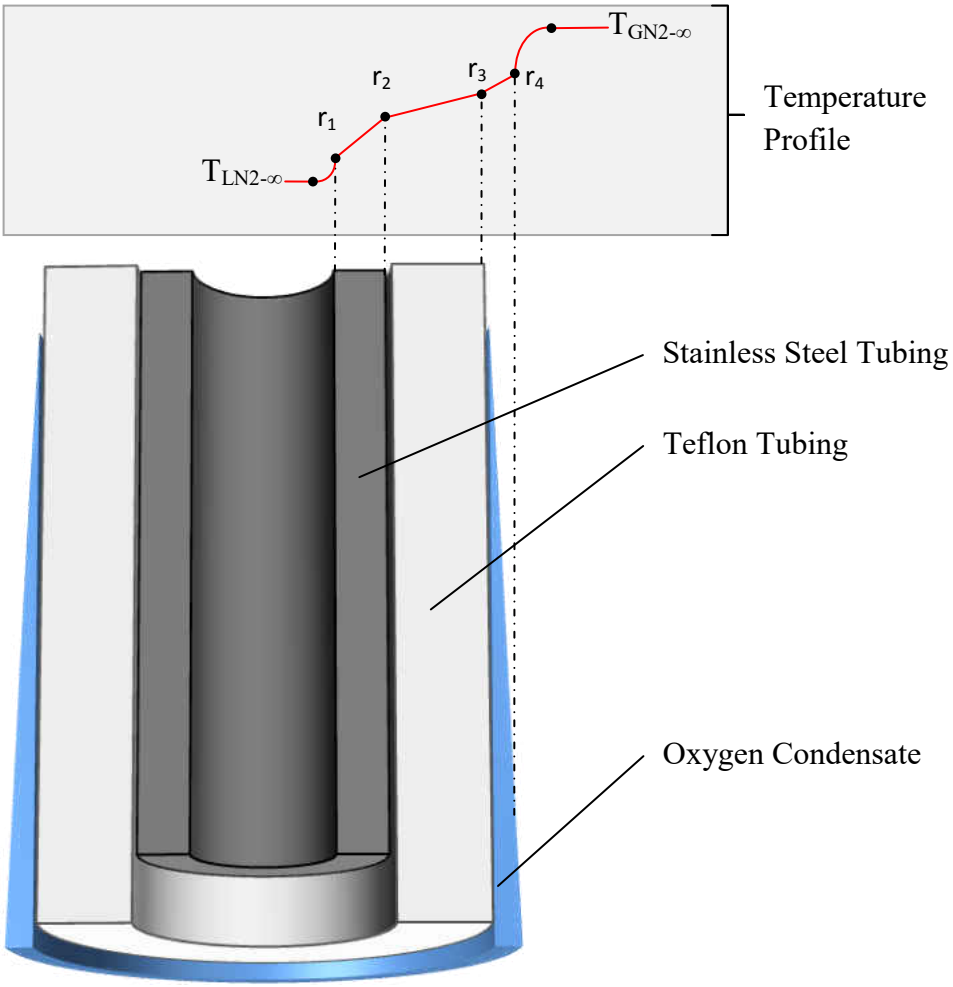

Figure 37: Fill and Vent Tubing Thermal Resistance Model

Figure 37 shows cutaway of the fill and vent tubes. The fill and vent tubes are composed of the stainless steel tubing surrounded by the Teflon tubing as insulation. Depending on the Teflon outer wall temperature, oxygen may condense on the outside of the Teflon. The nitrogen flows down through the fill tube as two phase fluid; then the nitrogen flows up through the vent tube as a gas. The outside of both the fill and vent tube is the natural convection. Heat transfers from the gaseous oxygen ullage through the natural convection boundary layer, through the oxygen condensate, through the Teflon and stainless steel by conduction, and through the internal convection layer.

Overall Radial Heat Transfer to the Fill Tube and Vent Tube

Equation (28) calculates the overall heat transfer through the fill and vent tubes [18].

$$q_r = \frac{T_{GO_2-\infty} - T_{LN_2-\infty}}{R_{tot}} \tag{28}$$

$$q_r = \frac{T_{GO_2-\infty} - T_{LN_2-\infty}}{\frac{1}{2\pi r_1 L h_{IC}} + \frac{\ln\left(\frac{r_2}{r_1}\right)}{2\pi k_{SS} L} + \frac{\ln\left(\frac{r_3}{r_2}\right)}{2\pi k_{PTFE} L} + \frac{1}{2\pi r_3 L h_{CC}} + \frac{1}{2\pi r_4 L h_{EC}}} \tag{29}$$

Convection of Nitrogen Flowing Inside Fill Tube

Equation (30) through Equation (38) develop the convective heat transfer coefficient from the stainless steel tube wall to the nitrogen. Even though the nitrogen is subcooled before entering the IRAS, these calculations assume two-phase flow once entering the fill tube. The Chen correlation and the Kandlikar correlation were considered to evaluate the heat transfer coefficient, which provided the same order of magnitude result. The Chen correlation sums the convective contributions from the bulk convection and the microscopic nucleate boiling [30].

$$h_{IC} = h_{mic} + h_{mac} \tag{30}$$

$$h_{mic} = 0.00122\left[\frac{k_l^{0.79} c_{pl}^{0.45} \rho_l^{0.49}}{\sigma^{0.5} \mu_l^{0.29} h_{lv}^{0.24} \rho_v^{0.24}}\right][T_w - T_{sat}(P_l)]^{0.24}[P_{sat}(T_w) - P_l]^{0.75} S \tag{31}$$

$$S(Re_{tp}) = \left(1 + 2.56x10^{-6} Re_{tp}^{1.17}\right)^{-1} \tag{32}$$

$$Re_{tp} = Re_l[F(X_{tt})]^{1.25} \tag{33}$$

$$X_{tt} = \left(\frac{1-x}{x}\right)^{0.9}\left(\frac{\rho_v}{\rho_l}\right)^{0.5}\left(\frac{\mu_l}{\mu_v}\right)^{0.1} \tag{34}$$

$$F(X_{tt}) = \begin{cases} 1 & X_{tt}^{-1} \le 0.1 \\ 2.35\left(0.213 + \frac{1}{X_{tt}}\right)^{0.736} & X_{tt}^{-1} < 0.1 \end{cases} \tag{35}$$

$$h_{mac} = h_l F(X_{tt}) \tag{36}$$

$$h_l = 0.023\left(\frac{k_l}{D}\right) Re_l^{0.8} Pr_l^{0.4} \tag{37}$$

$$Re_l = \frac{4\dot{m}}{\pi \mu_l D} \tag{38}$$

Convection of Nitrogen Flowing Inside Vent Tube

Equation (39) calculates the convective heat transfer coefficient across the boundary layer from forced convection of the gaseous nitrogen flowing upward through the inside of the vent tube. Equation (39) is developed by solving the Navier-Stokes energy equation in cylindrical coordinates and assuming (1) laminar, fully developed flow and (2) isothermal inner vent tube wall [18].

$$h_{IC} = \frac{k_v}{D} Nu_D = 3.66 \frac{k_v}{D} \tag{39}$$

Equation (40) calculates the convective heat transfer coefficient across the boundary layer from forced convection of the gaseous nitrogen flowing upward through the inside of the vent tube [18]. Equation (40) uses the Gnielinski correlation by assuming (1) turbulent flow through (2) a smooth tube. For the most realistic flow regimes (GN_2 flows above 5 sLm), the GN_2 flow is turbulent.

$$h_{IC} = \frac{k_v}{D} Nu_D = \frac{k_v}{D} \left[\frac{(f/8)(Re_D - 1000)Pr}{1 + 12.7(f/8)^{1/2}(Pr^{2/3} - 1)} \right] \tag{40}$$

$$f = (0.790 \ln Re_D - 1.64)^{-2} \tag{41}$$

Condensation Correlation

Equation (42) represents the condensation convection coefficient and was developed using the Nusselt approximation for laminar flow, which is conditional on the value of the Reynolds number defined by Equation (44). Equation (45) and Equation (46) represent the condensation convection coefficient for the wavy and turbulent flow, respectively [18].

$$\bar{h}_{CC} = 0.943 \left[\frac{g\rho_l(\rho_l - \rho_v)k_l^3 h'_{lv}}{\mu_l(T_{sat} - T_s)L} \right]^{\frac{1}{4}} \tag{42}$$

$$h'_{lv} = h_{lv}(1 + 0.68Ja) \tag{43}$$

$$Re_\delta = \frac{4\bar{h}_L(T_{sat} - T_s)L}{\mu_l h'_{lv}} \tag{44}$$

$$\frac{\bar{h}_{CC}(\nu_l^2/g)^{1/3}}{k_l} = \frac{Re_\delta}{1.08Re_\delta^{1.22} - 5.2} \qquad 30 \le Re_\delta \le 1800 \tag{45}$$

$$\frac{\bar{h}_{CC}\left(v_l^2/g\right)^{1/3}}{k_l} = \frac{Re_\delta}{8750 + 58Pr^{-0.5}\left(Re_\delta^{0.75} - 253\right)} \qquad Re_\delta > 1800 \tag{46}$$

Natural Convection of Gaseous Oxygen Outside Fill Tube and Vent Tube

Equation (47) calculates the convective heat transfer coefficient through boundary layer developed by the natural convection [18]. Equation (47) assumes (1) flat, vertical plate analysis and (2) isothermal tube wall temperature and suggested for Rayleigh numbers below 10^9. The flat plate assumption can be applied to vertical cylinders if the boundary layer is much less than diameter of the cylinder; the condition is satisfied by Equation (48). The assumption that the tube walls are isothermal is a great approximation for the fill tube because the nitrogen is saturated and heat transferred to the nitrogen from the ullage gas produces a phase change and not a temperature change, thus, the nitrogen maintains the tube wall temperature. Although heat transferred to the nitrogen in the vent tube produces a temperature increase, the temperature increase is minimal, typically less than 10°C, and the isothermal assumption for the vent tube outer wall remains a good approximation.

$$h_{EC} = \frac{k_{GO_2}}{D}\overline{Nu}_D = \frac{k_{GO_2}}{D}\left[0.68 + \frac{0.670Ra_D^{1/4}}{\left[1 + \left(\frac{0.492}{Pr}\right)^{9/16}\right]^{4/9}}\right] \tag{47}$$

$$\frac{D}{L} = \frac{35}{Gr_L^{1/4}} \tag{48}$$

The results for simultaneous solutions for Equation (28) through Equation (47) as a function of insulation thickness are shown in Figure 38 and Figure 39 for the fill tube and vent tube, respectively. Each figure shows a "break-even" insulation thickness, which is the minimal

insulation thickness required to make any thermal resistance improvements. The proposed insulation thickness is 1.0625 inches and 1 inch for the fill tube and vent tube, respectively, and shown by the arrow on the right hand side of the figure pointing upward. The proposed insulation decreases the heat transfer through the fill tube and vent tube by 1.1W and 2.7W, respectively.

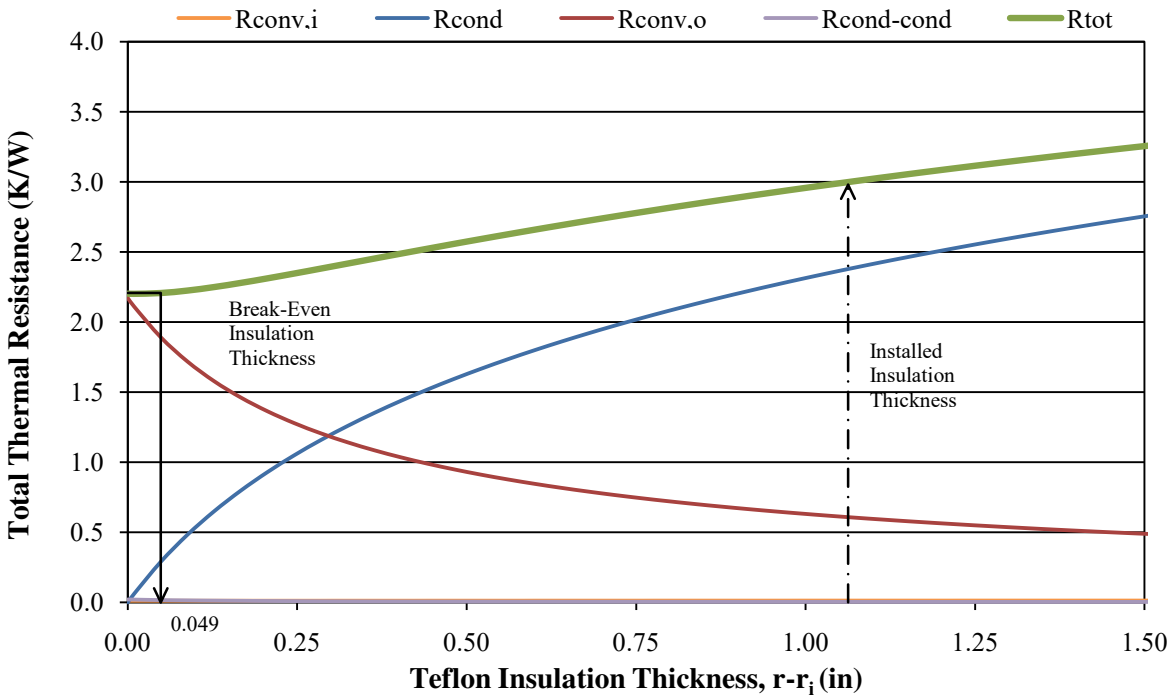

Figure 38: Fill Tube Insulation Optimization

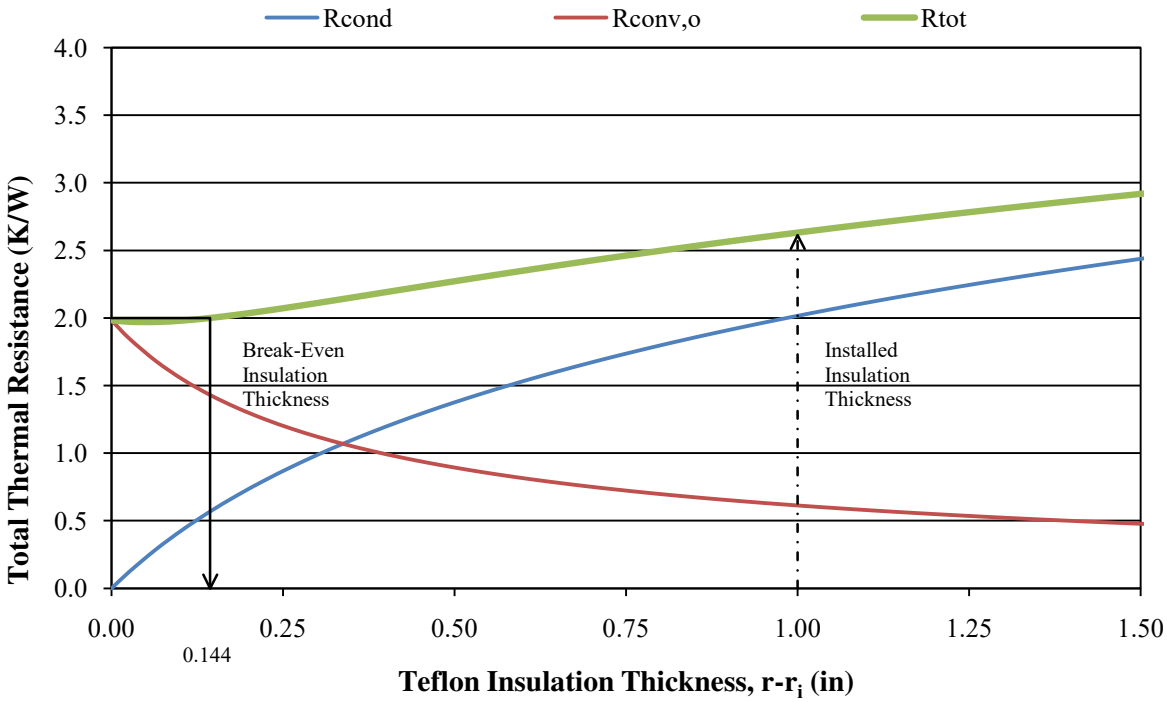

Figure 39: Vent Tube Insulation Optimization

Heat Transfer Analysis for IRAS Heat Exchanger

The IRAS heat exchanger is a ½" copper tubing in the shape of a "U" with annular fins. Figure 40 represents the heat exchanger and Figure 41 represents a cross-section of the IRAS heat exchanger for calculation purposes. The variables in Figure 41 are consistent with fin heat transfer presented in Incropera [18]. The overall length of the heat exchanger is 14 inches and the fins extend 5/16" in the radial direction from the base of the tubing.

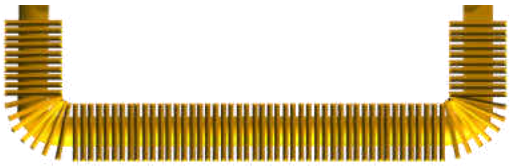

Figure 40: IRAS Heat Exchanger

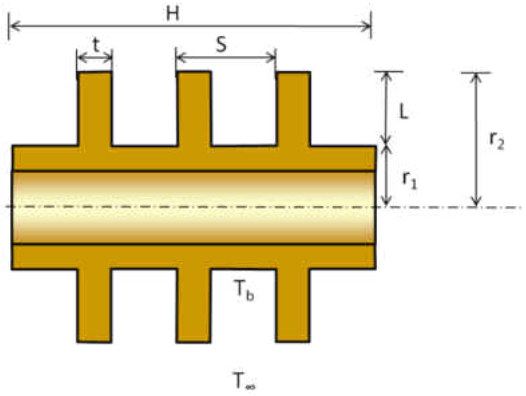

Figure 41: IRAS Heat Exchanger Cross-Section

Equation (49) calculates the heat transfer through the IRAS heat exchanger.

$$q_t = h\,A_t\left[1 - \frac{N\,A_f}{A_t}(1-\eta_f)\right]\theta_b \tag{49}$$

From Incropera, the convective heat transfer coefficient is given by Equation (50):

$$\overline{Nu}_D = \frac{\bar{h}D}{k} = \left\{0.60 + \frac{0.387Ra_D^{1/6}}{[1+(0.559/Pr)^{9/16}]^{8/27}}\right\}^2 \tag{50}$$

From Incropera, the total surface area of the heat exchanger is given by Equation (51):

$$A_t = NA_f + A_b = NA_f + 2\pi r_1(H - Nt) \tag{51}$$

From Incropera Table 3.5 for straight fins:

$$A_f = 2\pi\left(r_{2,c} - r_1\right)^2 \tag{52}$$

From Incropera, the single fin efficiency is given by Equation (53):

$$\eta_f = \frac{\tanh mL_c}{mL_c} = \frac{\tanh\left[\left(\frac{2h}{kA_p}\right)^{1/2} L_c^{3/2}\right]}{\left[\left(\frac{2h}{kA_p}\right)^{1/2} L_c^{3/2}\right]} \tag{53}$$

The heat exchanger is capable of transferring 3,400 W of heat. The fins increase the heat transfer rate capability by approximately 1000% when compared to a copper tube without fins.

APPENDIX B: EXPERIMENTAL SETUP INFORMATION

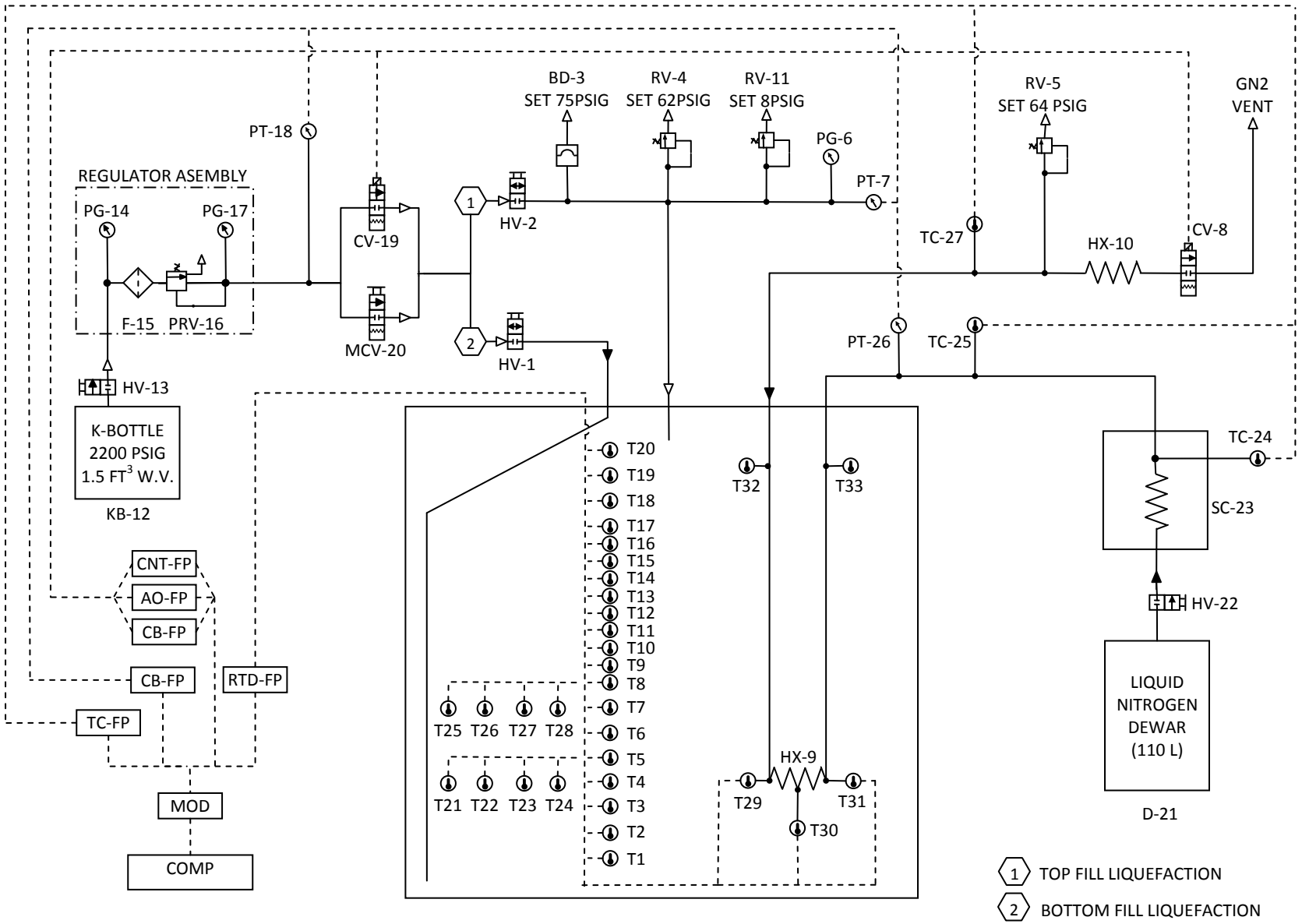

Figure 42: Experimental Setup - Detailed Process and Instrumentation Diagram

Table 6: Experimental Setup - Detailed Process and Instrumentation Legend

REFERENCE DESIGNATOR	DESCRIPTION	SPECIFICATION	MANUFACTURER	MANUFACTURER NUMBER
HV-1	IRAS DEWAR INLET VALVE (TYPICALLY LO2)	½"	EDEN CRYOGENICS	BC-02042-8101-1
HV-2	IRAS DEWAR EXIT VALVE (GO2 VENT)	½"	EDEN CRYOGENICS	BC-02042-8100-1
BD-3	IRAS BURST DISC	75PSIG	FIKE CORPORATION	P ST
RV-4	IRAS MAIN RELIEF VALVE	SET 61.7PSIG, 84SCFM	FLOWSAFE, INC	01-2190M-101
RV-5	IRAS COOLANT LOOP RELIEF VALVE	SET 63PSIG	FLOWSAFE, INC.	01-2190M-101
PG-6	IRAS DEWAR PRESSURE GAUGE	0-100 PSIG	ASHCROFT	1008
PT-7*	IRAS DEWAR PRESSURE TRANSDUCER	0-25PSIG	TELEDYNE TABER	2415
CV-8*	IRAS COOLANT LOOP MASS FLOW CONTROL VALVE	0-100 SLM ± 1SLM	TELEDYNE INSTR.	HFC-203
HX-9	IRAS HEAT EXCHANGER	½" COPPER TUBE		
HX-10	IRAS COOLANT LOOP AMBIENT HEAT EXCHANGER	½" COPPER TUBE		
RV-11	IRAS OPERATIONAL RELIEF VALVE	SET 8PSIG		
KB-12	GASEOUS OXYGEN K-BOTTLE	1.5 FT^3 (W.V)		
HV-13	K-BOTTLE ISOLATION VALVE			
PG-14	K-BOTTLE UPSTREAM PRESSURE GAUGE	0-4000 PSI	CONCOA	312-4311-540
F-15	GASEOUS OXYGEN FILTER	10 MICRON		
PRV-16	K-BOTTLE PRESSURE REGULATING VALVE	3000PSI TO 0-250PSI		
PG-17	K-BOTTLE DOWNSTREAM PRESSURE GAUGE	0-400 PSI		
PT-18*	GASEOUS OXYGEN PRESSURE TRANSDUCER			
CV-19*	MASS FLOW CONTROL VALVE (GO2)	0-20 SLM ± 0.2SLM	MKS INSTRUMENTS	1179A
MCV-20	MANUAL MASS FLOW CONTROL VALVE (GO2)	0-10 SLM	HOKE	1335M4Y
D-21	LIQUID NITROGEN DEWAR	110 LITER	TAYLOR WHARTON	
HV-22	LIQUID NITROGEN STORAGE DEWAR ISOLATION VALVE			
SC-23	SUBCOOLER			
TC-24*	SUBCOOLER COOLING FLUID EXIT THERMOCOUPLE	TYPE T (-200 to 350°C)	OMEGA	
TC-25*	IRAS HEAT EXCHANGER INLET THERMOCOUPLE	TYPE T (-200 to 350°C)	OMEGA	
PT-26*	SUBCOOLER PROCESS FLUID EXIT PRESSURE TRANSDUCER	0-30 PSIG ± 0.5 PSIG	WIKA INSTR.	4258112
TC-27*	IRAS HEAT EXCHANGER EXIT THERMOCOUPLE	TYPE T(-200 to 350°C)	OMEGA	
T1 – T32	IRAS DEWAR POSITION TEMPERATURE SENSOR	25K-450K ± 0.5K	SCIENTIFIC INSTR.	Si410

Table 6: Experimental Setup - Detailed Process and Instrumentation Legend (Continued)

REFERENCE DESIGNATOR	DESCRIPTION	SPECIFICATION	MANUFACTURER	MANUFACTURER NUMBER
TC-FP	THERMOCOUPLE FIELD POINT	8 CHANNEL	NATIONAL INSTRUM	cFP-TC-120
CB-FP	INTEGRATED CONTROL BLOCK FIELD POINT	8 CHANNEL	NATIONAL INSTRUM	cFP-CB-1
RTD-FP	TEMPERATURE MODULE FIELD POINT	8 CHANNEL	NATIONAL INSTRUM	cFP-RTD-124
AO-FP	ANALOG VOLTAGE OUTPUT MODULE FIELD POINT	8 CHANNEL 0-10V	NATIONAL INSTRUM	cFP-AO-210
CNT-FP	INTELLEGIENT CONTROLLER FIELD POINT	2 PORT	NATIONAL INSTRUM	cFP-2110
MOD	ETHERNET SWITCH MODEM	5 PORT	B&B ELECTRONICS	ELINX EIR205
COMP	COMPUTER	2.99GHz, 1.00GBRAM	DELL	PRECISION 670

*PT-7 (Designated as P1 by Labview) Calibrated by NASA-KSC Calibration Laboratory on 03/23/2010 and found within tolerance
*CV-8 (Designated as FM1 by Labview) Calibrated by NASA-KSC Calibration Laboratory on 04/09/2010 and found within tolerance
*PT-18 (Designated as P2 by Labview)
*CV-19 (Designated as FMC2 by Labview) Calibrated by Teledyne on 3/30/2010 and found within tolerance
*TC-24 (Designated as TC3 by Labview)
*TC-25 (Designated as TC2 by Labview)
*PT-26 (Designated as P3 by Labview) Calibrated by NASA-KSC Calibration Laboratory on 03/29/2010 and found within tolerance
*TC-27 (Designated as TC4 by Labview)

Figure 43: Process and Instrumentation Diagram Legend

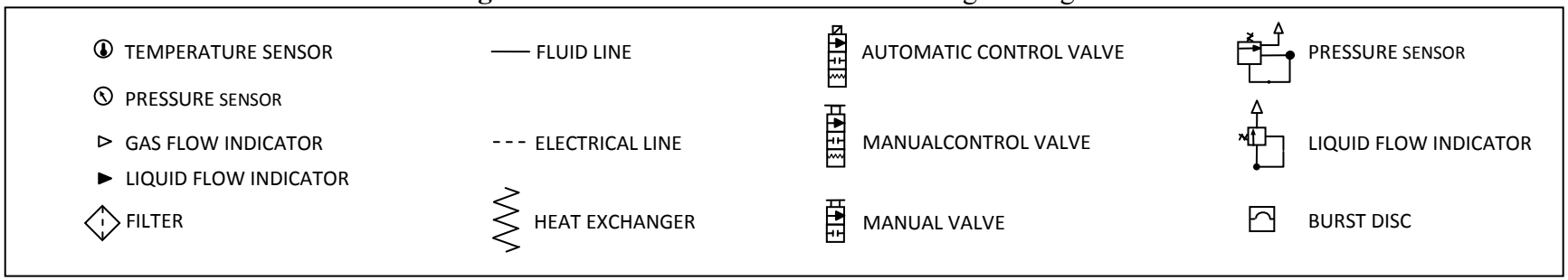

APPENDIX C: FLUID COMPOSITION

Nitrogen

NASA procures nitrogen in accordance with the military specification, MIL-PRF-27401. The purity and impurity limits are listed in Table 7 under the column titled, "Procurement Specification." The military specification requires the vendor to verify that the individual tanker load met the procurement specification prior to shipment, and shows an actual concentrations of the liquid procured. In addition to the vendor analysis, NASA randomly samples a tanker and analyzes the sample on a periodic basis. Table 7 provides average results from vendor and NASA analysis.

Table 7: Nitrogen Procurement Specification and Laboratory Analysis

Component	Procurement Specification[1]	Vendor Laboratory Analysis	NASA Laboratory Analysis
Nitrogen	99.5% (min)	99.999 %	>99.99 %
Oxygen	50 ppm (max)	0.4 ppm	<2 ppm[2]
Total Hydrocarbons	25 ppm (max)	0.4 ppm	<1 ppm[2]
Water	11.6 ppm (max)	0.9 ppm	<2 ppm[2]
Argon	Not Required	Not Required	7 ppm

[1] Nitrogen is procured to military specification, MIL-PRF-27401F Grade B.

[2] The unit, ppm, is parts per million by volume as a gas at standard conditions.
A less than ("<") represents a value below the lower detection limit of the analytical equipment.

Oxygen

NASA procures oxygen in accordance with the military specification, MIL-PRF-25508. Table 8 lists the purity and impurity requirements from the military specification. Like the nitrogen, a vendor analysis exists for every oxygen delivery. Unlike the nitrogen, a NASA analysis exists for every oxygen delivery as well the vendor analysis. Table 8 shows the average analysis for oxygen.

Table 8: Oxygen Procurement Specification and Laboratory Analysis

Component	Procurement Specification[1]	Vendor Laboratory Analysis	NASA Laboratory Analysis
Oxygen	99.99% (min)	>99.99 %	>99.989 %
Total Hydrocarbons	20 ppm (max)	<10.00 ppm[2]	6 ppm
Water	3 ppm (max)	<3.00 ppm[2]	<2 ppm[2]
Methane	16 ppm (max)	5.53 ppm	6 ppm
Ethane	2 ppm (max)	Not Measured	Not Measured
Propane	1 ppm (max)	<1.00 ppm[2]	Not Measured
Nitrous Oxide	1 ppm (max)	<1.00 ppm[2]	<1 ppm[2]
Halogenated Hydrocarbons	1 ppm (max)	<1.00 ppm[2]	<1 ppm[2]
Carbon Monoxide	1 ppm(max)	<1.00 ppm[2]	<1 ppm[2]
Carbon Dioxide			
Nitrogen	75 ppm(max)	4.50 ppm	<5 ppm[2]
Argon		31.56 ppm	19 ppm
Krypton		Not Measured	<5 ppm[2]
Helium	Not Required	Not Required	<10 ppm[2]

[1] Oxygen is procured to military specification, MIL-PRF-25508G Grade F.

[2] A less than ("<") represents a value below the lower detection limit of the analytical equipment. The unit, ppm, is parts per million by volume as a gas at standard conditions.

APPENDIX D: HEAT TRANSFER DERIVATION

Direct Contact Condensation by Vapor Collapse

Consider a flat, horizontal, cold plate with quiescent saturated oxygen vapor above the cold plate. A film of liquid oxygen condenses on the cold plate, with the film thickness, δ(t), increasing with time as shown in Figure 44. A control volume, represented by the dotted line, is established around the liquid-vapor interface [31]. The energy balance through the control volume is given by Equation (54).

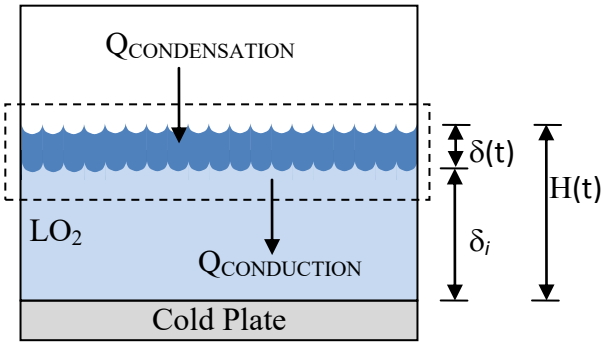

Figure 44: Heat Transfer Coefficient Derivation Model

$$Q_{CONDENSATION} = Q_{CONDUCTION} \tag{54}$$

$$\dot{m}_{COND}\, h'_{lv} = k_l\, A_s \left(\frac{T_{sat} - T_s}{H(t)}\right) \tag{55}$$

Where the height of the liquid from the cold plate is given by Equation (56).

$$H(t) = \delta_i + \delta(t) \tag{56}$$

$$\dot{m}_{COND} = \rho_l A_s \left(\frac{dH}{dt}\right) \tag{57}$$

Equation (58) is obtained by substituting Equation (57) into Equation (55).

$$\rho_l \cancel{A_s} \left(\frac{dH}{dt}\right) h'_{fg} = k_l \cancel{A_s} \left(\frac{T_{sat} - T_s}{H(t)}\right) \tag{58}$$

Rearranging Equation (58) , Equation (59) is obtained.

$$H\,dH = \frac{k_l\,(T_{sat} - T_s)}{h'_{lv}\,\rho_l}\,dt \tag{59}$$

Integrate Equation (59) to obtain Equation (61).

$$\int_{\delta_i}^{\delta_i+\delta} H\,dH = \frac{k_l\,(T_{sat} - T_s)}{h'_{lv}\,\rho_l}\int_0^t dt \tag{60}$$

$$\left[\frac{1}{2}(\delta_i + \delta)^2 - \frac{1}{2}(\delta_i)^2\right] = \frac{k_l\,(T_{sat} - T_s)}{h'_{lv}\,\rho_l}\,(t - 0) \tag{61}$$

Rearrange Equation (61) to obtain Equation (67).

$$\frac{1}{2}\left[\left(\delta_i{}^2 + 2\delta_i\delta + \delta^2\right) - (\delta_i)^2\right] = \frac{k_l\,(T_{sat} - T_s)}{h'_{lv}\,\rho_l}\,t \tag{62}$$

$$\left(2\delta_i\delta + \delta^2\right) + \delta_i^2 = \frac{2\,k_l\,(T_{sat} - T_s)}{h'_{lv}\,\rho_l}\,t + \delta_i^2 \tag{63}$$

$$(\delta_i + \delta)^2 = \frac{2\,k_l\,(T_{sat} - T_s)}{h'_{lv}\,\rho_l}\,t + \delta_i^2 \tag{64}$$

$$\delta_i + \delta = \sqrt{\frac{2\,k_l\,(T_{sat} - T_s)\,t}{h'_{lv}\,\rho_l} + \delta_i^2} \tag{65}$$

$$\delta = \sqrt{\frac{2\,k_l\,(T_{sat} - T_s)\,t}{h'_{lv}\,\rho_l} + \delta_i^2} - \delta_i \tag{66}$$

$$\delta = \sqrt{\frac{2\,k_l\,(T_{sat} - T_s)\,t + \delta_i^2\,h_{lv}\,\rho_l}{h_{lv}\,\rho_l}} - \delta_i \tag{67}$$

The general definition of the heat transfer coefficient is given by Equation (68).

$$h = \frac{k_l}{H(t)} = \frac{k_l}{\delta(t) + \delta_i} \tag{68}$$

Substitute Equation (67) into Equation (68) to obtain Equation (69), the derived heat transfer coefficient for condensation on flat, horizontal cold plate.

$$h = \frac{k_l}{\left[\sqrt{\frac{2\,k_l\,(T_{sat} - T_s)\,t + \delta_i^2\,h_{lv}\,\rho_l}{h_{lv}\,\rho_l}} - \delta_i\right] + \delta_i} \tag{69}$$

$$\boxed{h = k_l \sqrt{\frac{h_{lv}\,\rho_l}{2\,k_l\,(T_{sat} - T_s)\,t + \delta_i^2\,h_{lv}\,\rho_l}}} \tag{70}$$

The condensation mass flux is found by rearranging Equation (55).

$$G_{COND} = \frac{\dot{m}_{COND}}{A_s} = \frac{k_l}{h_{lv}}\left(\frac{T_{sat} - T_s}{H(t)}\right) \tag{71}$$

Substituting Equation (67) into Equation (71), gives the condensation mass flux, Equation (72).

$$G_{COND} = \frac{k_l}{h'_{lv}} \frac{(T_{sat} - T_s)}{\left[\sqrt{\frac{2\,k_l\,(T_{sat} - T_s)\,t + \delta_i^2\,h_{lv}\,\rho_l}{h_{lv}\,\rho_l}} - \delta_i\right] + \delta_i} \tag{72}$$

$$G_{COND} = \frac{k_l}{h'_{lv}}(T_{sat} - T_s)\sqrt{\frac{h_{lv}\,\rho_l}{2\,k_l\,(T_{sat} - T_s)\,t + \delta_i^2\,h_{lv}\,\rho_l}} \tag{73}$$

$$\boxed{G_{COND} = k_l(T_{sat} - T_s)\sqrt{\frac{\rho_l}{h_{lv}\left[2\,k_l\,(T_{sat} - T_s)\,t + \delta_i^2\,h_{lv}\,\rho_l\right]}}} \tag{74}$$

Direct Contact Condensation by Bubble Collapse

Bubble Departure Frequency Derivation

$$f_{b,d} = \frac{\dot{m}_{GO_2}}{m_{b,d}} \tag{75}$$

$$f_{b,d} = \frac{\dot{m}_{GO_2}}{\rho_v V_{b,d}} \tag{76}$$

$$f_{b,d} = \frac{\dot{m}_{GO_2}}{\rho_v \left[\frac{4}{3}\pi\left(\frac{D_{b,d}}{2}\right)^3\right]} \tag{77}$$

$$\boxed{f_{b,d} = \frac{6\,\dot{m}_{GO_2}}{\pi\,\rho_v\,D_{b,d}^3}} \tag{78}$$

Mass Condensation Rate of Bubble

$$\dot{m}_{b,cond} = [m_{b,cond}][f_{b,d}] \tag{79}$$

$$\dot{m}_{b,cond} = \left[\frac{6\,\dot{m}_{GO_2}}{\pi\,\rho_v\,D_{b,d}^3}\right]\left[\rho_v\frac{4\pi}{3}\left(\frac{D_{b,d}}{2}\right)^3 - \rho_v\frac{4\pi}{3}\left(\frac{D_{t_r}}{2}\right)^3\right] \tag{80}$$

$$\dot{m}_{b,cond} = \left[\frac{\cancel{6}\,\dot{m}_{GO_2}}{\cancel{\pi}\,\cancel{\rho_v}\,D_{b,d}^3}\right]\left[\cancel{\rho_v}\frac{\cancel{\pi}}{\cancel{6}}\left({D_{b,d}}^3 - {D_{t_r}}^3\right)\right] \tag{81}$$

$$\dot{m}_{b,cond} = \dot{m}_{GO_2}\left(\frac{{D_{b,d}}^3 - {D_{t_r}}^3}{{D_{b,d}}^3}\right) \tag{82}$$

$$\dot{m}_{b,cond} = \dot{m}_{GO_2}\left[\left(\frac{D_{b,d}}{D_{b,d}}\right)^3 - \left(\frac{D_{t_r}}{D_{b,d}}\right)^3\right] \tag{83}$$

$$\boxed{\dot{m}_{b,cond} = \dot{m}_{GO_2}\left(1 - {\beta_{t_r}}^3\right)} \quad \text{where } \frac{D_{b,t_r}}{D_{b,d}} = \beta_{t_r} \tag{84}$$

$$\dot{m}_{COND} = \dot{m}_{b,COND} + \dot{m}_{ULL,COND} \tag{85}$$

$$\dot{m}_{COND} = \dot{m}_{COND}\left(1 - {\beta_{t_r}}^3\right) + G_{COND}A_{CS-IRAS} \tag{86}$$

$$\dot{m}_{COND} - \dot{m}_{COND}\left(1 - {\beta_{t_r}}^3\right) = \dot{m}_{COND}\left[1 - \left(1 - {\beta_{t_r}}^3\right)\right] = G_{COND}A_{CS} \tag{87}$$

$$\dot{m}_{COND}\left({\beta_{t_r}}^3\right) = G_{COND}A_{CS} \tag{88}$$

$$\boxed{\dot{m}_{COND} = \frac{G_{COND}A_{CS}}{{\beta_{t_r}}^3}} \tag{89}$$

Transient Conduction Heat Transfer Analysis Above Heat Exchanger

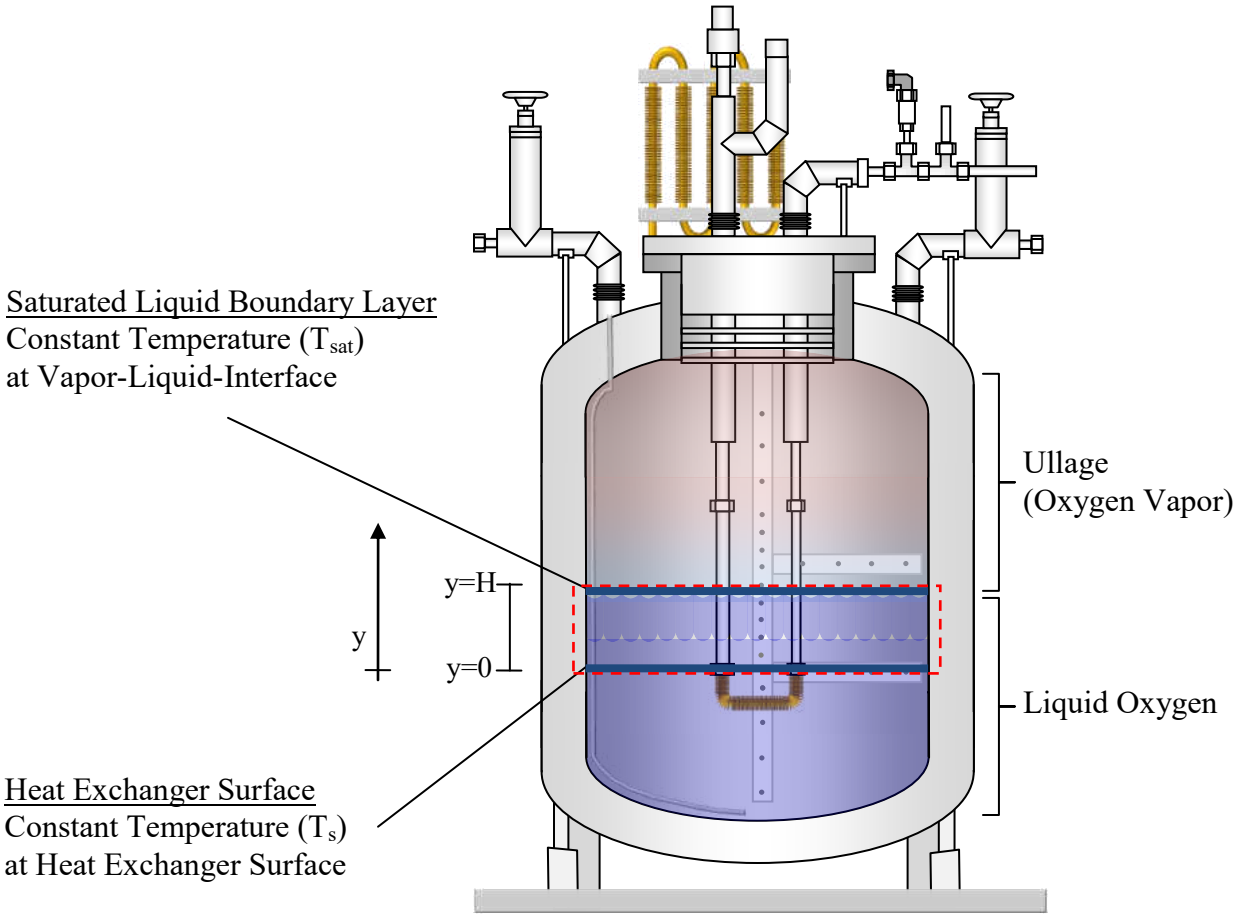

Figure 45: Heat Transfer Model in Liquid Above Heat Exchanger

Figure 45 represents heat transfer analysis for the liquid above the heat exchanger. The heat transfer analysis assumes transient conduction bounded by the constant temperatures of the saturated liquid temperature and heat exchanger surface temperature at the upper and lower boundaries, respectively. The initial temperature condition of the liquid within the bounded region is the saturation temperature. The saturation temperature is greater than the heat exchanger surface temperature, and the density is directly proportional to the temperature within the temperature range of the bounded region. Thus, the liquid within the bounded region is stable and the heat transfer is conduction dominant within the bounded region.

Equation (90) is the non-homogeneous form of the heat equation, while Equation (91) through Equation (93) represent the boundary conditions. Equation (94) shows the solution to the boundary value problem [32].

$$\alpha \frac{\partial^2 \theta(y,t)}{\partial y^2} + r = \frac{\partial \theta(y,t)}{\partial t} \tag{90}$$

$$\theta(H,t) = \theta_i = T_{sat} - T_s \tag{91}$$

$$\theta(0,t) = 0 = T_s - T_s \tag{92}$$

$$\theta(y,0) = \theta_i = T_{sat} - T_s \tag{93}$$

$$\theta(y,t) = -\frac{r}{2\alpha}y^2 + \left(\frac{\theta_i}{H} + \frac{r\,H}{2\alpha}\right)y + \sum_{n=1}^{\infty} \frac{2\theta_i}{n\pi} \sin\left(\frac{n\pi y}{H}\right) e^{-\alpha\left(\frac{n\pi}{H}\right)^2 t} \tag{94}$$

Equation (95) shows Equation (94) when r is set to 0. Equation (96) is the temperature profile of the Equation (95).

$$\theta(y,t) = \frac{\theta_i}{H}y + \sum_{n=1}^{\infty} \frac{2\theta_i}{n\pi} \sin\left(\frac{n\pi y}{H}\right) e^{-\alpha\left(\frac{n\pi}{H}\right)^2 t} \tag{95}$$

$$\boxed{T(y,t) = \theta(y,t) + T_s = \frac{\theta_i}{H}y + \sum_{n=1}^{\infty} \frac{2\theta_i}{n\pi} \sin\left(\frac{n\pi y}{H}\right) e^{-\alpha\left(\frac{n\pi}{H}\right)^2 t} + T_s} \tag{96}$$

Transient Conduction Heat Transfer Analysis Below Heat Exchanger

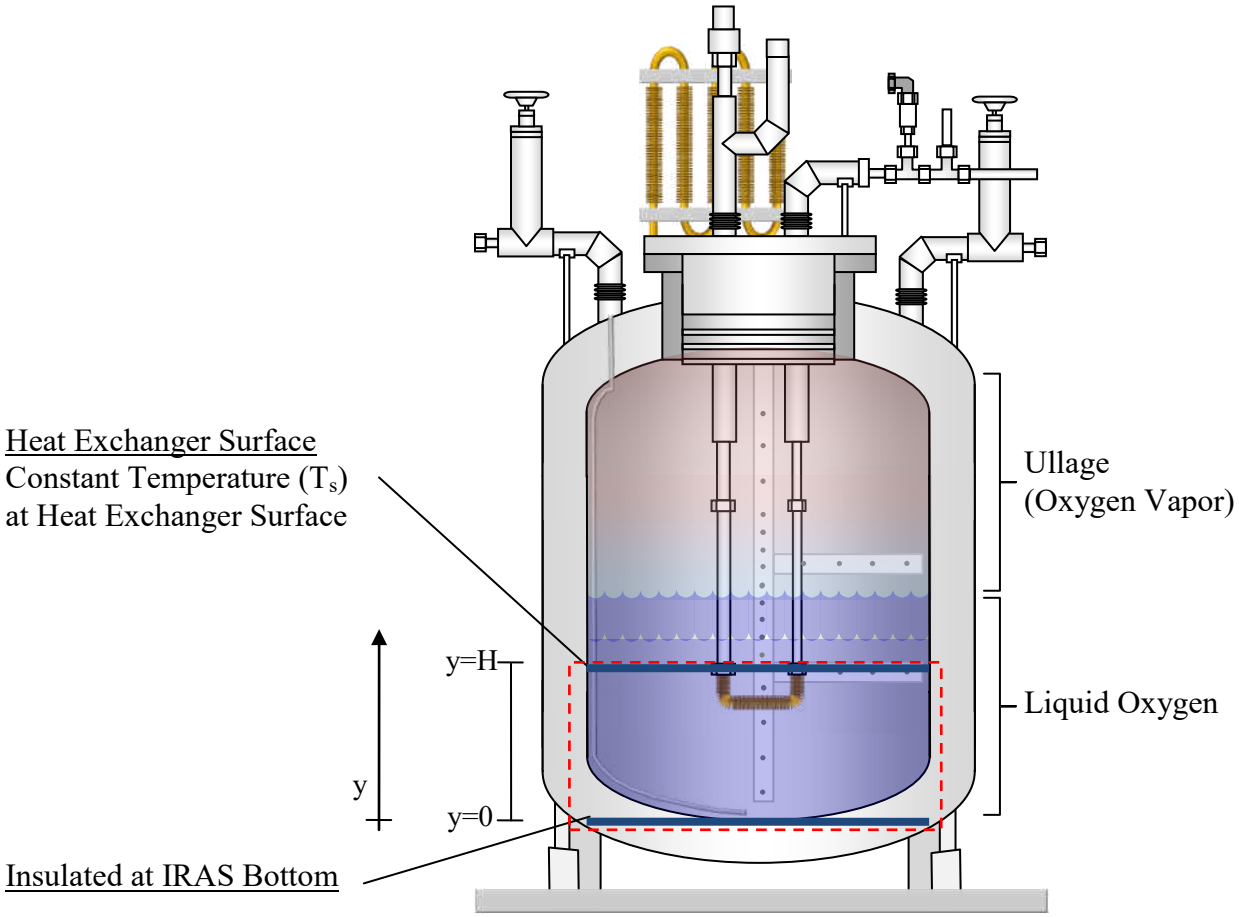

Figure 46: Heat Transfer Model for Liquid Below Heat Exchanger

Figure 46 represents heat transfer analysis for the liquid below the heat exchanger. The heat transfer analysis assumes transient conduction bounded by the constant temperature of the heat exchanger surface temperature at the upper boundary and an insulated condition at the lower boundary. The initial temperature condition of the liquid within the bounded region is the saturation temperature.

Convection occurs within the bounded region because the liquid density is greater at the top of the bounded region, which is kept constant at a lower temperature than the bulk fluid

temperature. Nevertheless, the bounded region below the heat exchanger is modeled as using transient conduction heat transfer analysis. The results of the conduction heat transfer is averaged with respect to depth below the heat exchanger (y-coordinate) to provide the prediction for the cooling rate of the bulk liquid oxygen below the heat exchanger.

Equation (97) is the heat equation, while Equation (98) through Equation (100) represent the boundary conditions. Equation (101) shows the solution to the boundary value problem.

$$\alpha \frac{\partial^2 \theta(y,t)}{\partial y^2} = \frac{\partial \theta(y,t)}{\partial t} \tag{97}$$

$$\theta(y,t) = T(y,t) - T_s \tag{98}$$

$$\theta(H,t) = 0 = T_s - T_s \tag{99}$$

$$\left.\frac{\partial \theta}{\partial y}\right|_{y=0} = 0 \tag{100}$$

$$\theta(y,0) = \theta_i = T_{sat} - T_s \tag{101}$$

$$\theta(y,t) = \sum_{n=1}^{\infty} \frac{4\theta_i}{(2n-1)\pi} \sin\left(\frac{(2n-1)\pi\, y}{2\, H}\right) e^{-\alpha\left[\left(\frac{2n-1}{2}\right)\frac{\pi}{H}\right]^2 t} \tag{102}$$

Equation (103) is the temperature profile of the Equation (102).

$$\boxed{T(y,t) = \theta(y,t) + T_s = \sum_{n=1}^{\infty} \frac{4\theta_i}{(2n-1)\pi} \sin\left(\frac{(2n-1)\pi\, y}{2\, H}\right) e^{-\alpha\left[\left(\frac{2n-1}{2}\right)\frac{\pi}{H}\right]^2 t} + T_s} \tag{103}$$

APPENDIX E: IRAS ANALYSIS AND METHODS

Determination of Liquid Height

The vapor-liquid interface remains at the saturated temperature as determined by the IRAS dewar pressure and Equation (112) and Equation (113). For the instance that the saturated temperature falls between two position temperature sensors, thus, the vapor-liquid interface is between the heights represented by the two temperature sensors, as represented in Figure 47.

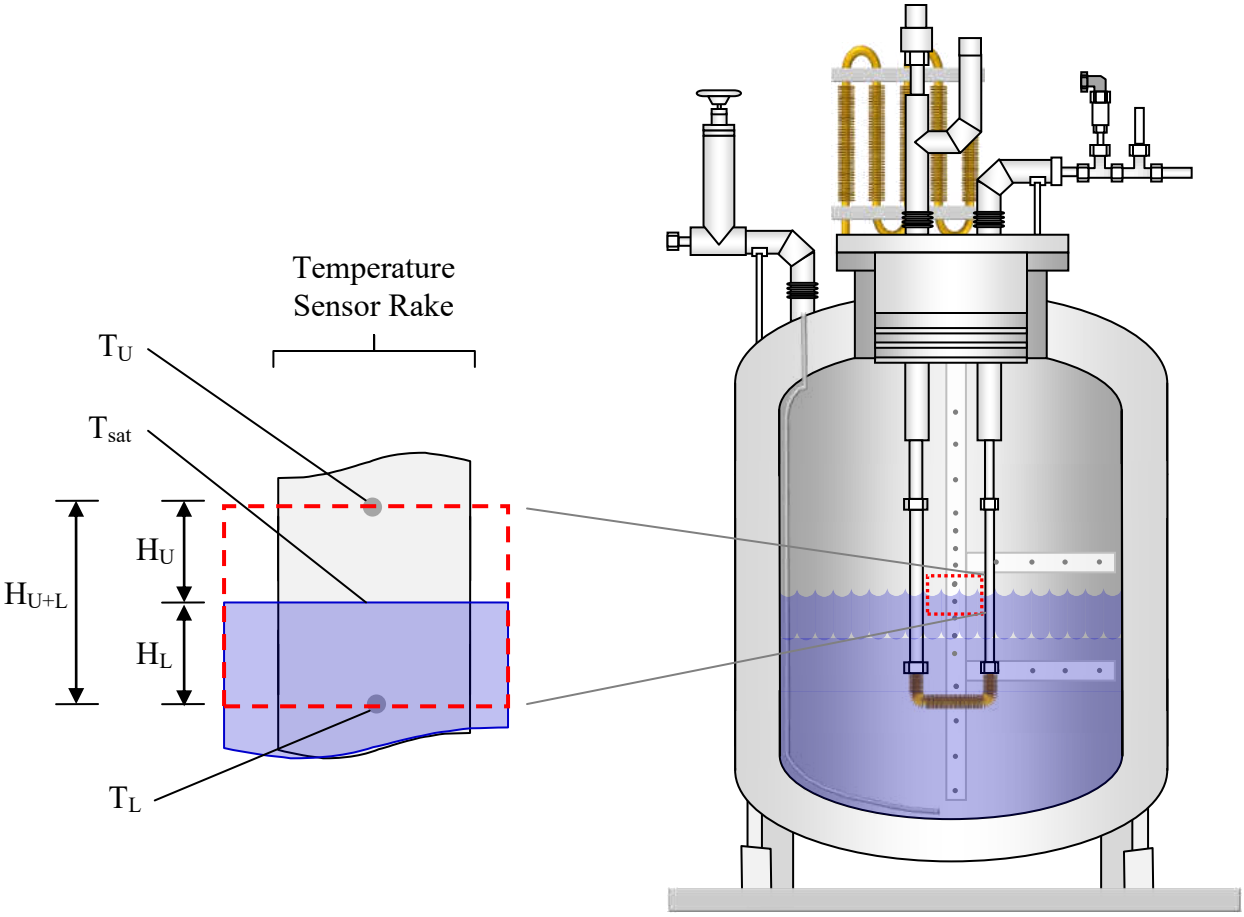

Figure 47: Determination of Vapor-Liquid Interface Between Two Temperature Sensors

An energy balance around the vapor-liquid interface, represented by the red dotted line in Figure 47, is shown in Equation (104) with heat conduction analysis in Equation (105). Finally, Equation (107) is added to the overall height of the position temperature sensor to obtain the

overall liquid height. The thermal conductivity, k_L and k_U, are determined by Equation (122) and Equation (118), respectively.

$$Q_L = Q_U \tag{104}$$

$$k_L \frac{A}{H_L}(T_{sat} - T_L) = k_U \frac{A}{H_U}(T_U - T_{sat}) \tag{105}$$

$$H_{U+L} = H_U + H_L \tag{106}$$

$$\frac{k_U(T_U - T_{sat})}{k_L(T_{sat} - T_L)} = \frac{H_{U+L} - H_L}{H_L} = \frac{H_{U+L}}{H_L} - 1 \tag{107}$$

$$H_L = \frac{H_{U+L}}{\left(\frac{k_U(T_U - T_{sat})}{k_L(T_{sat} - T_L)} + 1\right)} = \frac{H_{U+L}\, k_L(T_{sat} - T_L)}{\left(k_U(T_U - T_{sat}) + k_L(T_{sat} - T_L)\right)} \tag{108}$$

Mass Accumulation by Ullage Pressure and Temperature Variation

The mass liquefaction rate was measured by the CV-18 and MCV-19, assumes that the gaseous oxygen flow rate into the IRAS dewar is liquefied, or that no gaseous oxygen accumulates in the ullage. The liquefaction and densification tests were intended to run at a constant pressure, however, small variations within the operation of the liquid nitrogen flow controller, CV-8, resulted in small variations in the IRAS dewar pressure. These small variations in the IRAS dewar pressure, coupled with small variations in ullage temperature, affected the density of the vapor within the ullage of the IRAS dewar and allowed accumulation of gaseous oxygen within the ullage. The density at each position temperature location can be estimated by Equation (115). The product of the density and volume at each position temperature provides the mass at each location. If the position temperature sensor is below the IRAS dewar head, Equation (109) calculates the volume. If the position temperature sensor is within the IRAS dewar head, Equation (110) calculates the volume of the spherical cap.

$$V = \frac{\pi}{4} D^2 \left(H_{T_i} - H_{T_{i-1}} \right) \tag{109}$$

$$V = \frac{\pi H^2}{3} (3D - H) \tag{110}$$

The use of the trapezoidal rule provides a mass estimate of the gaseous oxygen within the ullage. Calculating the density between two time periods provides an estimate of a mass accumulation rate within the ullage.

Energy Accumulation by Heat Capacitance Variation

Figure 44 shows heat conduction through the liquid oxygen from the vapor-liquid interface to the theoretical cold plate at the bottom of the liquid layer. However, the model neglects any energy accumulation within the liquid layer as heat capacitance. Nevertheless, energy accumulation occurs within the liquid layer due to the temperature variations within the liquid, and Equation (111) accounts for any variations within the liquid layer. The liquid oxygen density and liquid oxygen heat capacity is determined by Equation (121) and Equation (120), respectively. As with the above methods, the trapezoidal rule is used to provide the change in overall heat capacitance.

$$Q = \rho_{LO_2}\, c_p\, H\, A_{CS}\, \frac{\Delta T}{\Delta t} \tag{111}$$

APPENDIX F: DATA REFERENCES

The data that support the Test Matrices in CHAPTER THREE are presented below as a reference to results presented in Figure 10 through Figure 17, Figure 23 through Figure 27, and Figure 28 through Figure 32.

Table 9: Data Reference for Test 2 Matrix

Test Run	Pressure	GO_2 Flow Rate	Date	Start Time	Stop Time
2a	3 psig	0 sLm	8/19/10	11:02:10	11:41:10
2b	5 psig	0 sLm	8/19/10	13:08:10	13:43:10
2c	7 psig	0 sLm	8/19/10	14:50:13	15:00:10

Table 10: Data Reference for Test 3 Matrix - Top Fill Liquefaction

Test Run	Pressure	GO_2 Flow Rate	Date	Start Time	Stop Time
3a	3 psig	2.5 sLm	8/20/10	10:10:37	10:23:37
3b		5.0 sLm	8/20/10	10:34:17	10:45:37
3c		7.5 sLm	8/20/10	10:56:28	11:05:37
3d		10.0 sLm	8/20/10	13:01:00	13:12:37
3e		15.0 sLm	9/2/10	11:45:29	12:17:52
3f		20.0 sLm			
3g	5 psig	2.5 sLm	8/19/10	16:16:10	16:22:10
3h		5.0 sLm	8/19/10	16:25:10	16:35:10
3i		7.5 sLm	8/19/10	16:41:10	16:49:10
3j		10.0 sLm	8/19/10	16:51:10	17:05:10
3k		15.0 sLm	9/1/10	15:04:57	15:14:57
3l		20.0 sLm	9/15/10	15:09:31	15:32:31
3m	7 psig	2.5 sLm	8/19/10	15:43:10	15:57:10
3n		5.0 sLm	8/19/10	15:06:10	15:20:10
3o		7.5 sLm	8/19/10	15:22:10	15:31:10
3p		10.0 sLm	8/19/10	15:32:10	15:42:10
3q		15.0 sLm	9/2/10	14:26:09	14:33:09
3r		20.0 sLm	9/2/10	14:12:09	14:22:09

Table 11: Data Reference for Test 3 Matrix - Bottom Fill Liquefaction

Test Run	Pressure	GO_2 Flow Rate	Date	Start Time	Stop Time
3aa	3 psig	2.5sLm	8/20/10	13:57:44	14:07:45
3bb		5.0sLm	8/20/10	15:32:45	15:43:45
3cc		7.5sLm	8/20/10	15:47:45	16:05:45
3dd		10.0sLm	8/20/10	16:06:45	16:31:45
3ee		15.0sLm	9/14/10	13:05:59	13:26:59
3ff		20.0sLm	9/14/10	13:44:59	13:56:59
3gg	5 psig	2.5sLm	8/23/10	10:40:27	11:00:27
3hh		5.0sLm	8/23/10	11:07:27	11:23:27
3ii		7.5sLm	8/23/10	12:11:27	12:25:27
3jj		10.0sLm			
3kk		15.0sLm	9/7/10	14:20:00	14:31:00
3ll		20.0sLm	9/7/10	14:56:00	15:23:00
3mm	7 psig	2.5sLm	8/23/10	13:07:30	13:32:27
3nn		5.0sLm	8/23/10	13:33:11	14:09:27
3oo		7.5sLm	8/23/10	14:09:34	14:31:27
3pp		10.0sLm	8/23/10	14:54:27	15:13:27
3qq		15.0sLm	9/13/10	12:48:15	13:07:15
3rr		20.0sLm	9/14/10	15:14:59	15:40:59

APPENDIX G: OXYGEN AND NITROGEN PROPERTY CORRELATIONS

Oxygen Vapor Pressure

Equation (112) and Equation (113) calculate the vapor pressure of oxygen at a given temperature [31]. The units for temperature and pressure are Kelvin and bar, respectively.

$$\ln\left(\frac{P}{P_t}\right) = A\chi + B\chi^2 + C\chi^3 + D\chi(1-\chi)^{\varepsilon} \tag{112}$$

$$\chi = \frac{\left(1-\frac{T_t}{T}\right)}{\left(1-\frac{T_t}{T_c}\right)} \tag{113}$$

Where,

A = 7.7977723
B = 4.5773000
C = -1.9281264
D = 3.2931232
ε = 1.5
P_t = 0.001464 bar
T_t = 54.359 K
T_c = 154.581 K

Oxygen Vapor Heat Capacity

Equation (114) calculates the heat capacity of oxygen vapor [31]. The units for heat capacity, universal gas constant, and temperature are J/kg·K, J/mol·K, and K, respectively.

$$\frac{c_{P,O_2}}{R} = \frac{A_1}{T^3} + \frac{A_2}{T^2} + \frac{A_3}{T} + A_4 + A_5 T + A_6 T^2 + A_7 T^3 + \frac{A_8 \left(\frac{A_9}{T}\right)^2 e^{\frac{A_9}{T}}}{\left(e^{\frac{A_9}{T}} - 1\right)^2} \quad (114)$$

Where,

A_1 =	$-1.86442361 \times 10^{2}$	K^3
A_2 =	2.07840241×10^{1}	K^2
A_3 =	$-3.42642911 \times 10^{-1}$	K
A_4 =	3.50297163×10^{0}	
A_5 =	$2.05866482 \times 10^{-7}$	K^{-1}
A_6 =	$-1.11035799 \times 10^{-8}$	K^{-2}
A_7 =	$2.08612876 \times 10^{-11}$	K^{-3}
A_8 =	1.01894691×10^{0}	
A_9 =	2.23918105×10^{3}	K

Oxygen Vapor Density

Equation (115), Equation (116), and Equation (117) calculate the vapor density of oxygen at a given temperature and pressure [31]. The units for pressure, temperature, and density are bar, Kelvin, and grams per cubic centimeter.

$$P = T\,R\,\rho_{GO_2}\left(1 + B\,\rho_{GO_2} + C\,\rho_{GO_2}{}^2\right) \tag{115}$$

$$B = \sum_{j}^{5} B_j\,T^{\frac{1-j}{4}} \tag{116}$$

Where,

B_1 = -8.638001288 x 10^2
B_2 = 1.733064315 x 10^4
B_3 = -1.241961054 x 10^5
B_4 = 3.956609285 x 10^5
B_5 = -4.904475356 x 10^5

$$C = \sum_{j}^{6} C_j\,T^{\frac{1-j}{2}} \tag{117}$$

Where,

C_1 = 3.569552013 x 10^5
C_2 = -2.696578423 x 10^7
C_3 = 8.152809009 x 10^8
C_4 = -1.229796911 x 10^{10}
C_5 = 9.252345993 x 10^{10}
C_6 = -2.771904509 x 10^{11}

Oxygen Vapor Thermal Conductivity

A fifth order polynomial curve was applied to data for oxygen vapor thermal conductivity obtained from Barron [32]. Equation (118) shows the third order polynomial curve from Microsoft Excel. The constants, A, B, C, D, E and F, within Equation (118) contain 15 decimals to reduce error for data fit to 0.5%. The result of Equation (118) shall include only four significant digits. Figure 48 shows the thermal conductivity data with the plot of Equation (118).

$$k_{GO_2} = A + BT + CT^2 + DT^3 + ET^4 + FT^5 \quad (118)$$

Where,

A = - 0.001223076523818 W/m·K
B = 0.000117232490577 W/m·K^2
C = - 0.000000263079458 W/m·K^3
D = 0.000000001644465 W/m·K^4
E = - 0.000000000005347 W/m·K^5
F = 0.000000000000006 W/m·K^6

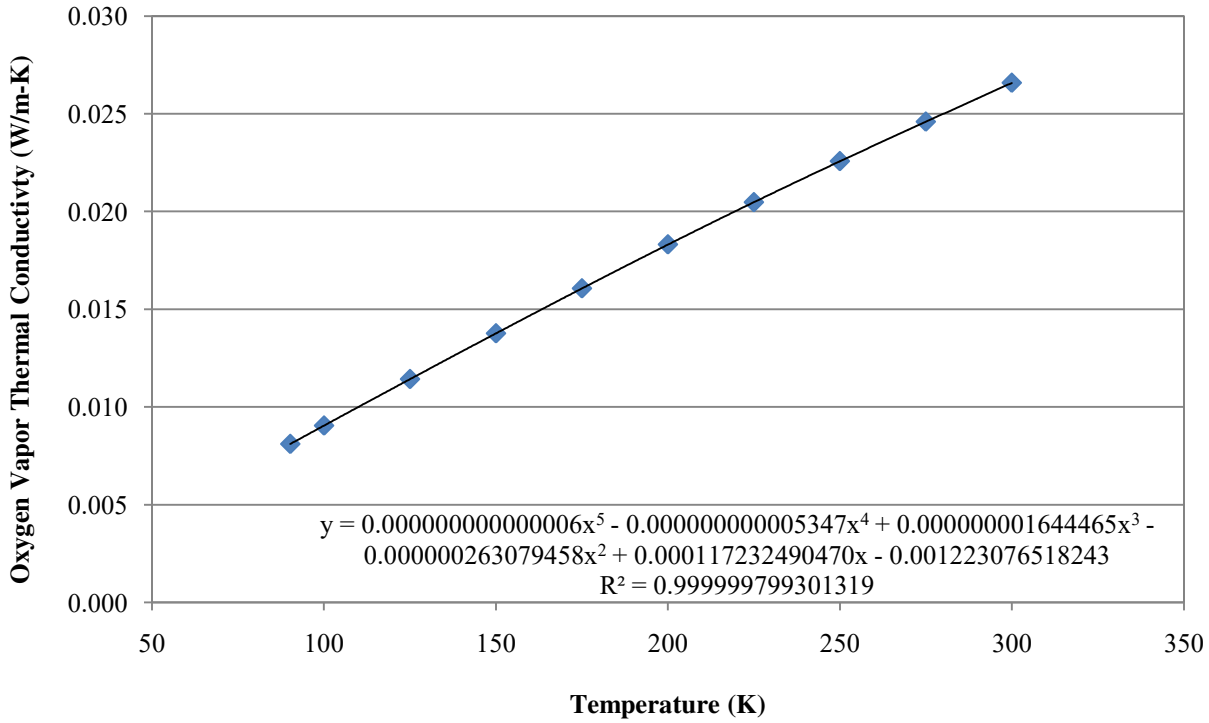

Figure 48: Oxygen Vapor Thermal Conductivity

Oxygen Latent Heat

A third order polynomial curve was applied to data for oxygen latent heat obtained from Weber [31]. Equation (119) shows the third order polynomial curve from Microsoft Excel. The constants, A, B, C, and D, within Equation (119) contain 15 decimals to reduce error for data fit to 0.03%. The result of Equation (119) shall only include significant digits to the tenth's place. Figure 49 shows the thermal conductivity data with the plot of Equation (119).

$$h_{lv} = A + BT + CT^2 + DT^3 \quad (119)$$

Where,

A = -0.000081397422873 kJ/kg
B = 0.014733449692986 kJ/kg·K
C = -1.65158600623311 kJ/kg·K²
D = 301.861319160972 kJ/kg·K³

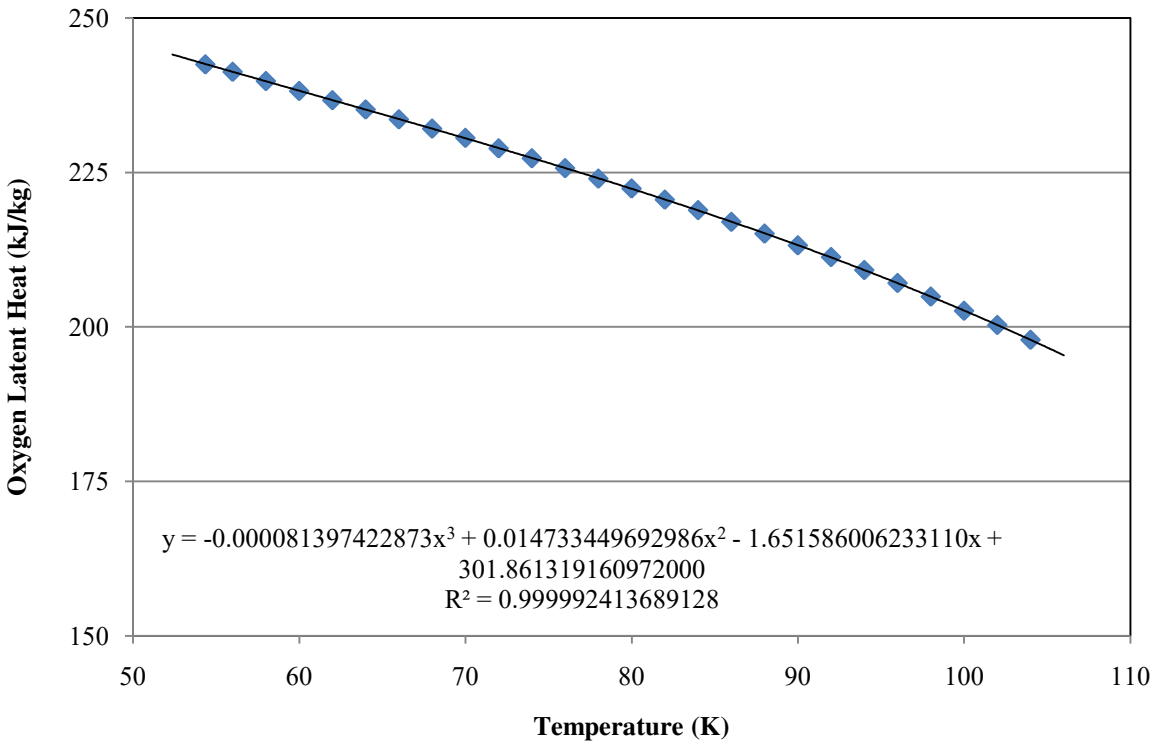

Figure 49: Oxygen Latent Heat

Liquid Oxygen Heat Capacity

A fifth order curve was applied to data for liquid oxygen density obtained from Barron [33]. Equation (120) shows the sixth order curve from Microsoft Excel. The constants, A, B, C, D, E, and F, within Equation (120) contain 15 decimals to reduce error for data fit to 0.11%. The result of Equation (120) shall include only four significant digits. Figure 50 shows the liquid oxygen density data with the plot of Equation (120).

$$c_{P,LO_2} = A + BT + CT^2 + DT^3 + ET^4 + FT^5 \quad (120)$$

Where,

A =	-804.941841795574	J/kg·K
B =	157.662398397089	J/kg·K^2
C =	-3.98909926785794	J/kg·K^3
D =	0.049706461920543	J/kg·K^4
E =	-0.000304345673485	J/kg·K^5
F =	0.000000737635884	J/kg·K^6

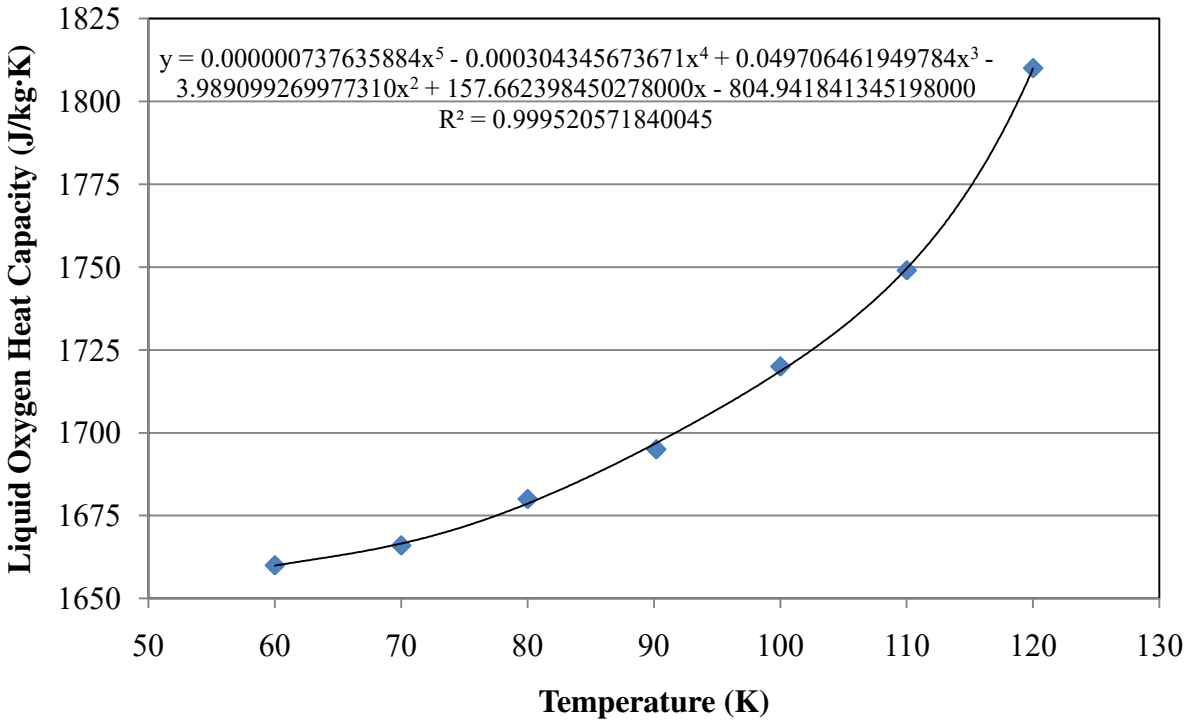

Figure 50: Liquid Oxygen Heat Capacity

Liquid Oxygen Density

A sixth order curve was applied to data for liquid oxygen density obtained from Weber [31]. Equation (121) shows the sixth order curve from Microsoft Excel. The constants, A, B, C, D, E, F, and G, within Equation (121) contain 15 decimals to reduce error for data fit to 0.005%. The result of Equation (121) shall include only six significant digits. Figure 51 shows the liquid oxygen density data with the plot of Equation (121).

$$\rho_{LO_2} = A + BT + CT^2 + DT^3 + ET^4 + FT^5 + GT^6 \quad (121)$$

Where,

A =	1,828.14835415939	kg/m³
B =	-24.4327054318406	kg/m³·K
C =	0.601754991149983	kg/m³·K²
D =	-0.009840755672421	kg/m³·K³
E =	0.000092502281069	kg/m³·K⁴
F =	-0.000000472160225	kg/m³·K⁵
G =	0.000000001000684	kg/m³·K⁶

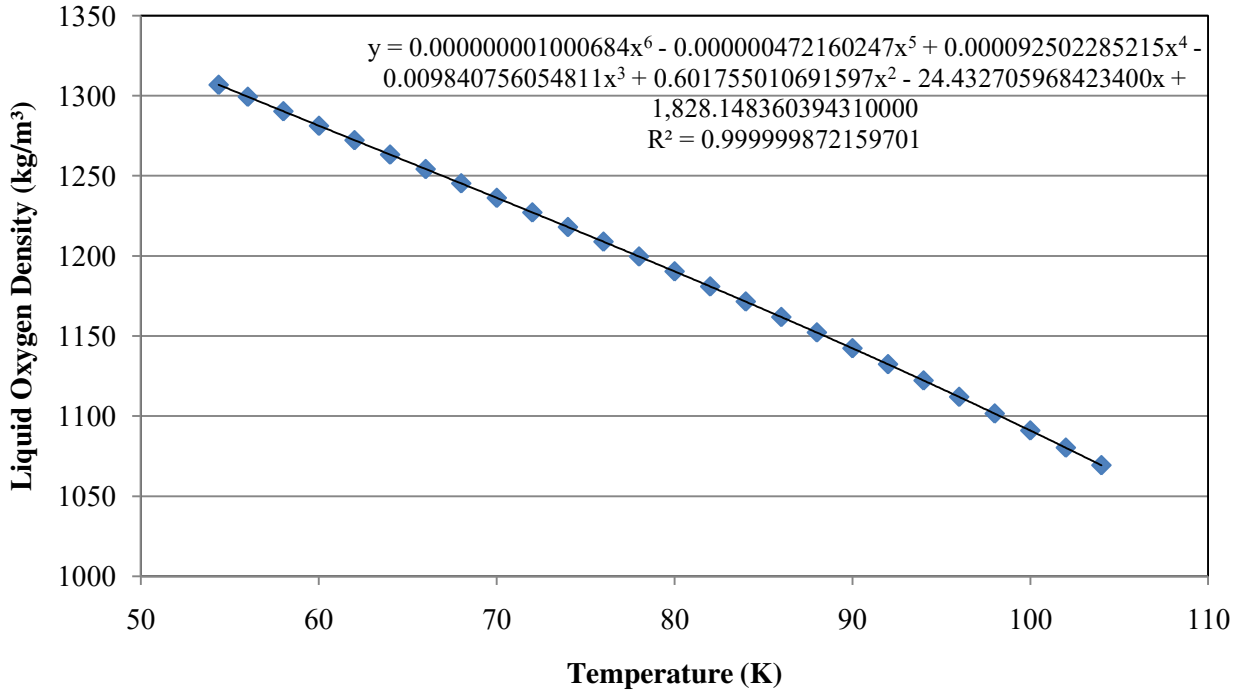

Figure 51: Liquid Oxygen Density

Liquid Oxygen Thermal Conductivity

A third order polynomial curve was applied to data for liquid oxygen thermal conductivity obtained from Barron [32]. Equation (122) shows the third order polynomial curve from Microsoft Excel. The constants, A, B, C, and D, within Equation (122) contain 15 decimals to reduce error for data fit to 0.06%. The result of Equation (122) shall include only four significant digits. Figure 52 shows the thermal conductivity data with the plot of Equation (122).

$$k_L = A + BT + CT^2 + DT^3 \quad (122)$$

Where,

A = 0.213338803988351 W/m·K
B = 0.000289487448988 W/m·K^2
C = - 0.000014585678268 W/m·K^3
D = 0.000000041651737 W/m·K^4

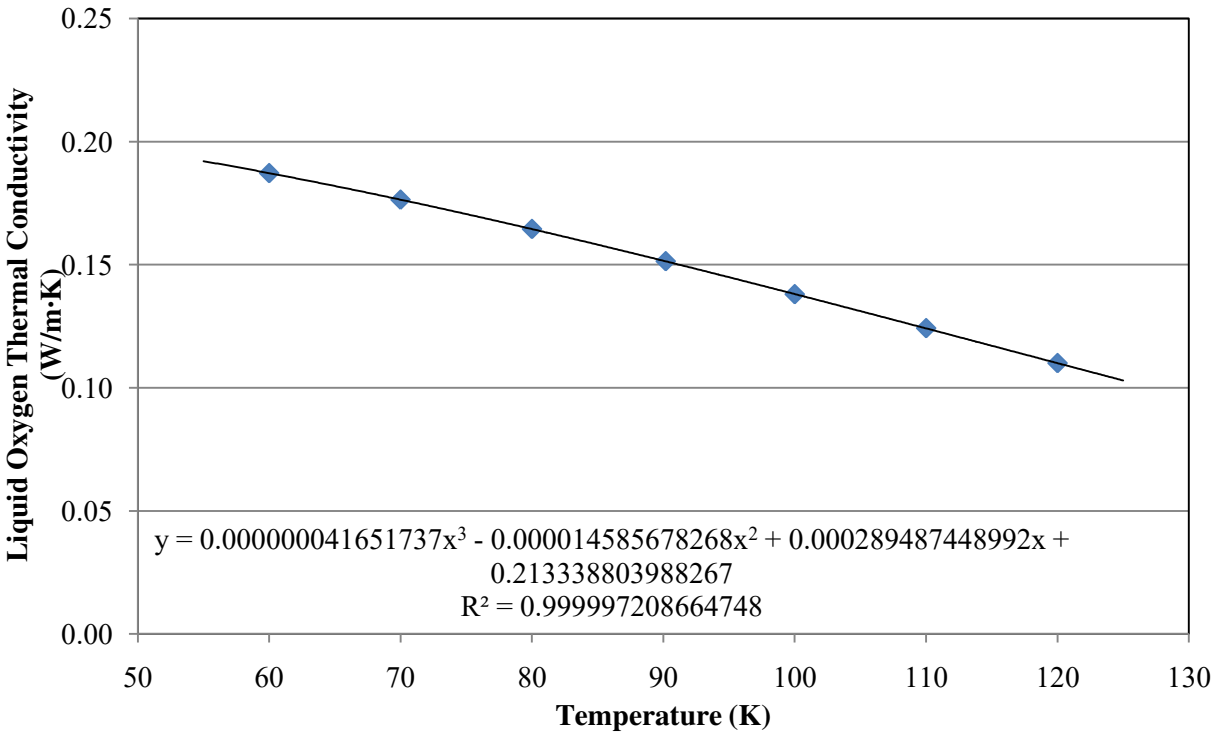

Figure 52: Liquid Oxygen Thermal Conductivity

Liquid Oxygen Viscosity

A fifth order polynomial curve was applied to data for liquid oxygen viscosity obtained from Barron [32]. Equation (123) shows the third order polynomial curve from Microsoft Excel. The constants, A, B, C, D, E, and F, within Equation (123) contain 25 decimals to reduce error for data fit to 0.4%. The result of Equation (123) shall include only three significant digits. Figure 53 shows the thermal conductivity data with the plot of Equation (123).

$$\mu_{LO_2} = A + BT + CT^2 + DT^3 + ET^4 + FT^5 \quad (123)$$

Where,

A =	0.014715060173857	kg/m·s
B =	- 0.000654848991496395	kg/m·s·K
C =	0.0000120104628576337	kg/m·s·K^2
D =	- 0.000000111227943528256	kg/m·s·K^3
E =	0.000000000515819966482693	kg/m·s·K^4
F =	-0.000000000000095362943927 49	kg/m·s·K^5

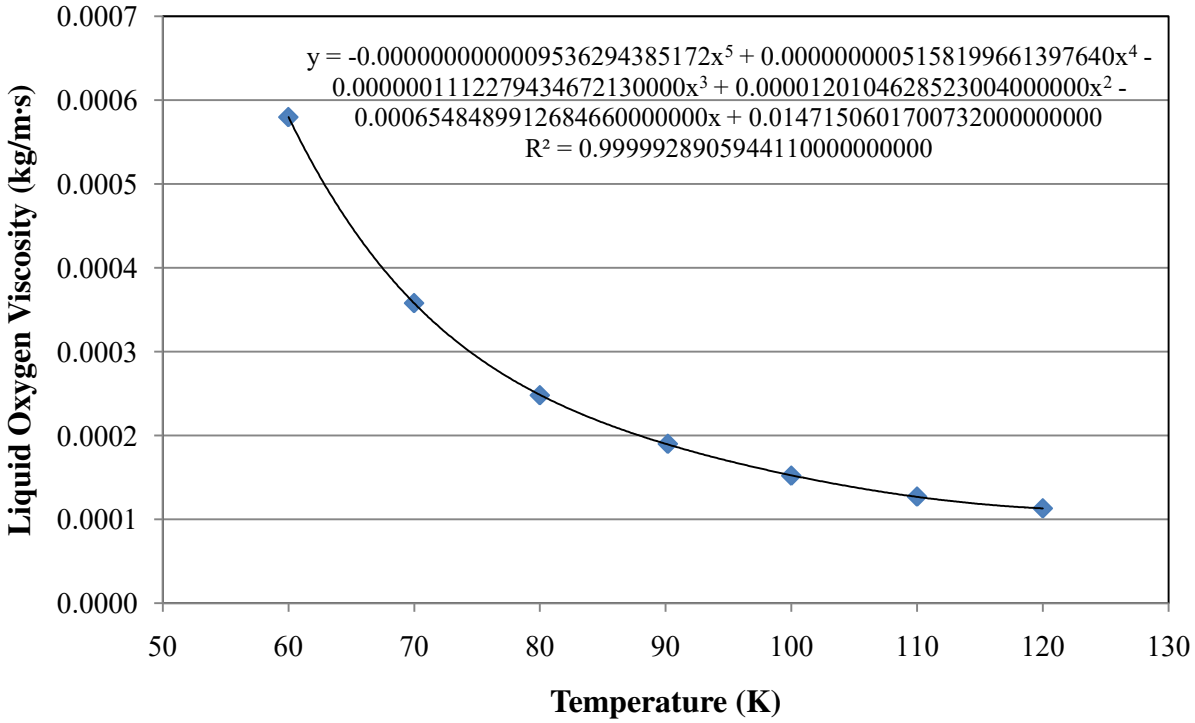

Figure 53: Liquid Oxygen Viscosity

Liquid Oxygen Surface Tension

A third order polynomial curve was applied to data for liquid oxygen surface tension obtained from Barron [32]. Equation (124) shows the third order polynomial curve from Microsoft Excel. The constants, A, B, C, and D, within Equation (124) contain 25 decimals to reduce error for data fit to 0.07%. The result of Equation (124) shall include only three significant digits. Figure 54 shows the surface tension data with Equation (124).

$$\sigma_L = A + BT + CT^2 + DT^3 \quad (124)$$

Where,

A =	0.0378427336225679	N/m
B =	- 0.000280199822845628	N/m·K
C =	- 0.00000009855225489719	N/m·K^2
D =	0.00000000194328853049	N/m·K^3

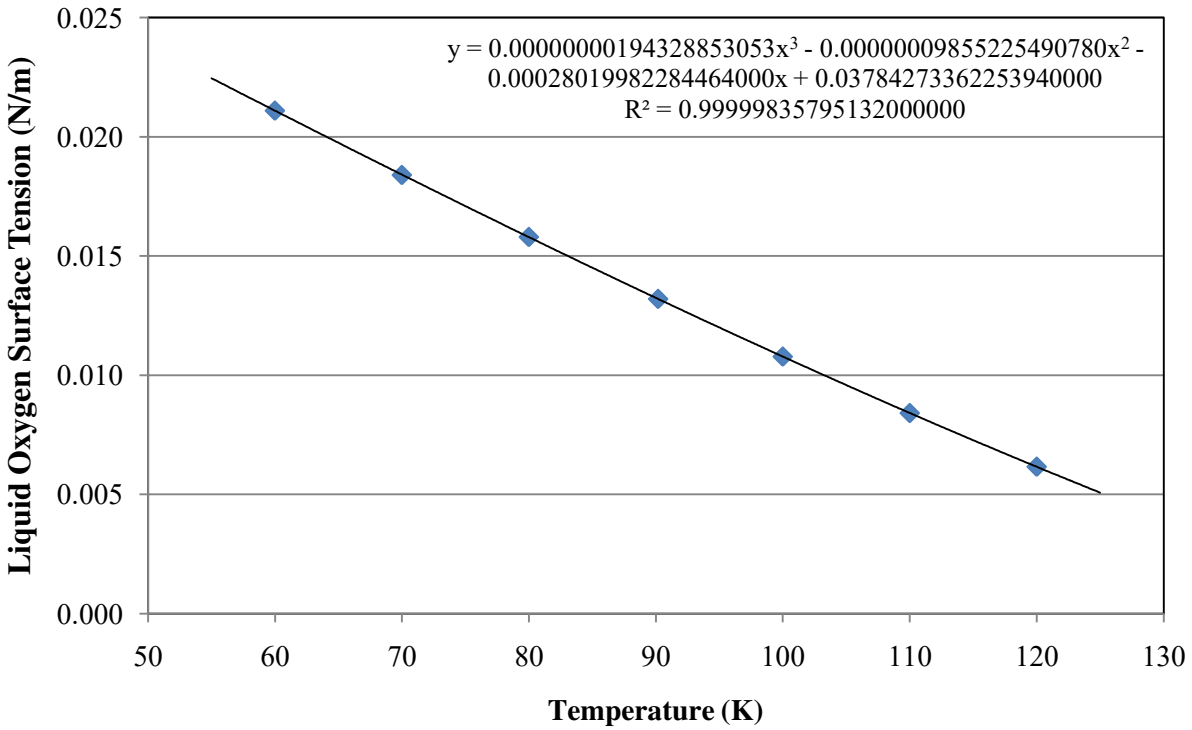

Figure 54: Liquid Oxygen Surface Tension

Nitrogen Vapor Pressure

Equation (125) calculates the vapor pressure of nitrogen at a given temperature [33].

$$\ln(P) = \frac{N_1}{T} + N_2 + N_3 T + N_4 (T_c - T)^{1.95} + N_5 T^3 + N_6 T^4 + N_7 T^5 + N_8 T^6 + N_9 \ln(T) \quad (125)$$

Where,

$N_1 = 0.8394409444 \times 10^4$
$N_2 = -0.1890045259 \times 10^4$
$N_3 = -0.7282229165 \times 10^1$
$N_4 = 0.1022850966 \times 10^{-1}$
$N_5 = 0.5556063825 \times 10^{-3}$
$N_6 = -0.5944544662 \times 10^{-5}$
$N_7 = 0.2715433932 \times 10^{-7}$
$N_8 = -0.4879535901 \times 10^{-10}$
$N_9 = 0.5095360824 \times 10^3$

Nitrogen Vapor Heat Capacity

Equation (126) calculates the heat capacity of nitrogen vapor [33]. The units for heat capacity, universal gas constant, and temperature are J/kg·K, J/mol·K, and K, respectively.

$$\frac{c_{P,N_2}}{R} = \frac{N_1}{T^3} + \frac{N_2}{T^2} + \frac{N_3}{T} + N_4 + N_5 T + N_6 T^2 + N_7 T^3 + \frac{N_8 \left(\frac{N_9}{T}\right)^2 e^{\frac{N_9}{T}}}{\left(e^{\frac{N_9}{T}} - 1\right)^2} \qquad (126)$$

Where,

N_1 =	$-0.7352104012 \times 10^{3}$	K^2
N_2 =	$0.3422399804 \times 10^{2}$	K
N_3 =	$-0.5576482846 \times 10^{0}$	
N_4 =	$0.3504042283 \times 10^{1}$	K^{-1}
N_5 =	$-0.1733901851 \times 10^{-4}$	K^{-2}
N_6 =	$0.1746508498 \times 10^{-7}$	K^{-3}
N_7 =	$-0.3568920335 \times 10^{-11}$	K^{-4}
N_8 =	$0.1005387228 \times 10^{1}$	K^{-1}
N_9 =	3353.4061	K

Nitrogen Latent Heat

A sixth order polynomial curve was applied to data for nitrogen latent heat obtained from Jacobsen and Stewart [33]. Equation (127) shows the sixth order polynomial curve from Excel. Figure 55 shows the thermal conductivity data with the plot of Equation (127).

$$h_{lv} = A + BT + CT^2 + DT^3 + ET^4 + FT^5 + GT^6 \quad (127)$$

Where,

A =	-2948.43396606397	kJ/kg
B =	227.92849346218	kJ/kg·K
C =	-6.72893704038077	kJ/kg·K^2
D =	0.104914396711496	kJ/kg·K^3
E =	-0.000915160992150	kJ/kg·K^4
F =	0.000004235559605	kJ/kg·K^5
G =	-0.000000008148664	kJ/kg·K^6

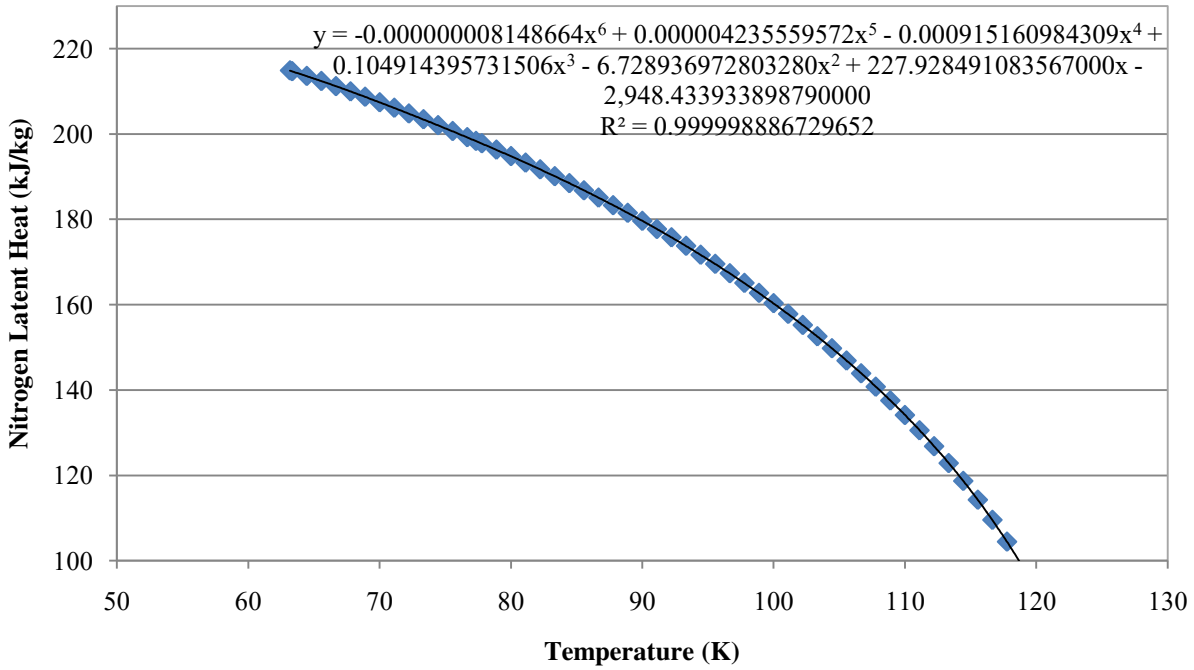

Figure 55: Nitrogen Latent Heat

Liquid Nitrogen Density

A sixth order polynomial curve was applied to data for liquid nitrogen density obtained from Jacobsen and Stewart [33]. Equation (128) shows the sixth order polynomial curve from Excel. Figure 56 shows the thermal conductivity data with the plot of Equation (128).

$$\rho_{LN_2} = A + BT + CT^2 + DT^3 + ET^4 + FT^5 + GT^6 \quad (128)$$

Where,

A =	-5,400.66873037872	kg/m^3
B =	454.403865170203	$kg/m^3 \cdot K$
C =	- 13.4124118295119	$kg/m^3 \cdot K^2$
D =	0.208986234251856	$kg/m^3 \cdot K^3$
E =	- 0.001826834840131	$kg/m^3 \cdot K^4$
F =	0.000008485691357	$kg/m^3 \cdot K^5$
G =	-0.000000016386729	$kg/m^3 \cdot K^6$

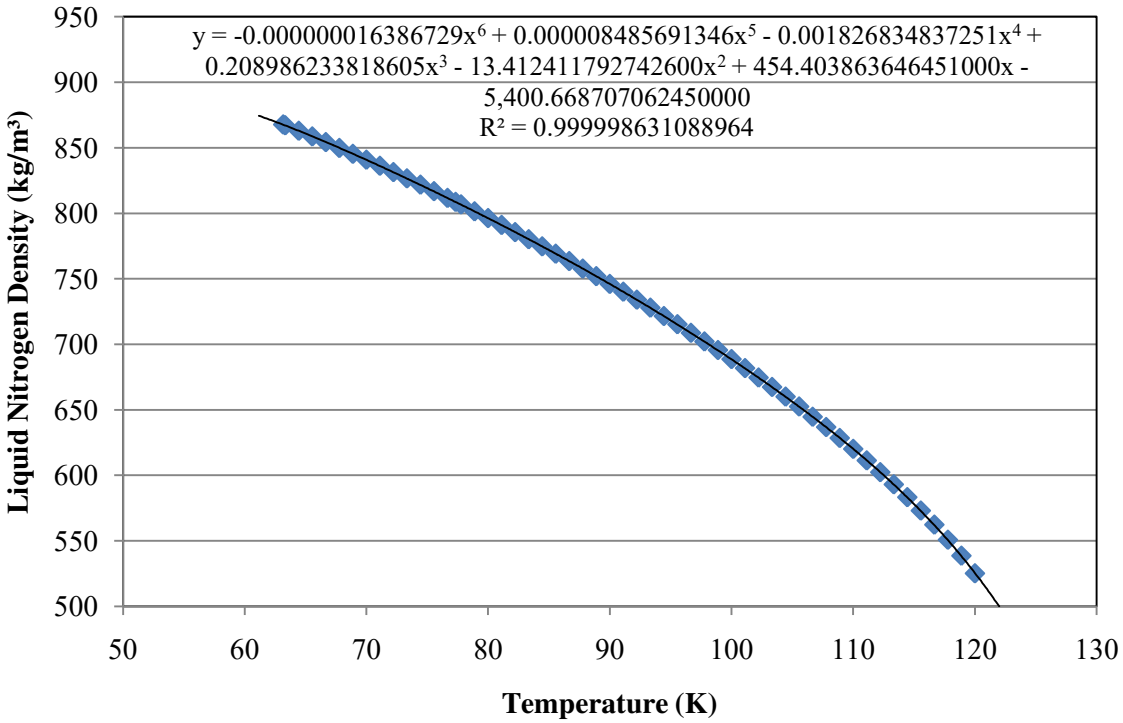

Figure 56: Liquid Nitrogen Density

APPENDIX H: ERROR ANALYSIS

Error Analysis for Equation (1)

$$\Delta G_{COND} = G_{COND} \sqrt{\left(-\frac{\Delta T}{2T}\right)^2 + \left(\frac{\sqrt{(\Delta[P_{sat}])^2 + \left(\Delta[P_g]\right)^2}}{[P_{sat} - P_g]}\right)^2} \tag{129}$$

$$\Delta P_{sat} = P_{sat}\left[A(\Delta\chi) + 2B\chi(\Delta\chi) + 3C\chi^2(\Delta\chi) + D^2\chi(1-\chi)^{\varepsilon}\sqrt{\left(\frac{\Delta\chi}{\chi}\right)^2 + \left(\frac{\varepsilon\,\Delta\chi}{1-\chi}\right)^2}\right] \tag{130}$$

The constants, A, B, C, D, and ε are provided by the constants used in Equation (112).

$$\Delta\chi = \frac{T_t\,\Delta T}{T^2\left(1 - \frac{T_t}{T_c}\right)} \tag{131}$$

The constants T_t and T_c are provided by the same constants in Equation (113).

Error Analysis for Equation (6)

$$\Delta G_{COND} = G_{COND}\left[\left(\frac{\Delta k_l}{k_l}\right)^2 + \left(\frac{\sqrt{(\Delta T_{sat})^2 + (\Delta T_s)^2}}{(T_{sat} - T_s)}\right)^2 + \left(\frac{\Delta \rho_l}{4\rho_l}\right)^2 + \left(\frac{\Delta h_{lv}}{4h_{lv}}\right)^2 + \frac{[2\, k_l\, (T_{sat} - T_s)\, t]^2 \left[4\left(\frac{\Delta k_l}{k_l}\right)^2 + 4\left(\frac{\sqrt{(\Delta T_{sat})^2 + (\Delta T_s)^2}}{T_{sat} - T_s}\right)^2 + 4\left(\frac{2\Delta t}{t}\right)^2\right]}{4\left[2\, k_l\, (T_{sat} - T_s)\, t + \delta_i^2\, h_{lv}\, \rho_l\right]^2} + \frac{\left[\delta_i^2\, h_{lv}\, \rho_l\right]^2 \left[2\left(\frac{\Delta \delta_i}{\delta_i}\right)^2 + \left(\frac{\Delta h_{lv}}{h_{lv}}\right)^2 + \left(\frac{\Delta \rho_l}{\rho_l}\right)^2\right]}{4\left[2\, k_l\, (T_{sat} - T_s)\, t + \delta_i^2\, h_{lv}\, \rho_l\right]^2}\right]^{\frac{1}{2}} \quad (132)$$

$$\Delta \rho_l = \sqrt{(B\, \Delta T)^2 + (2C\, T\, \Delta T)^2 + (3D\, T^2\, \Delta T)^2 + (4E\, T^3\, \Delta T)^2 + (5F\, T^4\, \Delta T)^2 + (6G\, T^5\, \Delta T)^2} \quad (133)$$

The constants, B, C, D, E, F, and G are provided by the constants used in Equation (121).

$$\Delta k_l = \sqrt{(B\, \Delta T)^2 + (2C\, T\, \Delta T)^2 + (3D\, T^2\, \Delta T)^2} \quad (134)$$

The constants, B, C, and D are provided by the constants used in Equation (122).

$$\Delta h_{lv} = \sqrt{(B\, \Delta T)^2 + (2C\, T\, \Delta T)^2 + (3D\, T^2\, \Delta T)^2} \quad (135)$$

The constants, B, C, and D are provided by the constants used in Equation (119).

APPENDIX I: SAMPLE CALCULATIONS

Equation (1)

$$G_{COND} = \left(\frac{M}{2\pi R_u T}\right)^{\frac{1}{2}} [P_g - P_{sat}]$$

The molecular weight of oxygen is 0.032 kg/mol. The universal gas constant is 8.314 J/mol·K. The sample calculation for Equation (1) uses a liquid temperature of 94K at an IRAS system pressure of 7 psig. Equation (112) estimates the saturated pressure at a temperature of 94K.

$$G_{COND} = \left(\frac{0.032\frac{kg}{mol}}{2\pi\left(8.314\frac{J}{mol\cdot K}\right)94K}\right)^{\frac{1}{2}} [149{,}588Pa - 148{,}353Pa]$$

$$\boxed{G_{COND} = 3.153\frac{kg}{s\cdot m^2}}$$

Equation (2)

$$h = \left(\frac{M}{2\pi R_u T}\right)^{\frac{1}{2}} \frac{h_{lv}^2}{T\, v_{lv}}$$

The components inside the parenthesis have been addressed in the Equation (1) sample calculation. Equation (119) estimates the latent heat at a temperature of 94K, while the difference between the reciprocals of Equation (115) and Equation (121) provides the specific volume change from vapor to liquid.

$$h = \left(\frac{0.032\frac{kg}{mol}}{2\pi\left(8.314\frac{J}{mol\cdot K}\right)94K}\right)^{\frac{1}{2}} \frac{\left[209{,}190\frac{J}{kg}\right]^2}{(94K)\left[\frac{1}{4.127\frac{kg}{m^3}} - \frac{1}{1122.252\frac{kg}{m^3}}\right]}$$

$$\boxed{h = 5{,}097\frac{kW}{m^2\cdot K}}$$

Equation (3)

$$G_{COND} = \left(\frac{M}{2\pi R_u T}\right)^{\frac{1}{2}} [\Gamma(a)\sigma_c P_v - \sigma_e P_g]$$

The components inside the parenthesis and the two pressures were determined in the two above sample calculations. The condensation coefficient, σ_c, and evaporation coefficient, σ_e, are set equal to 1. The function, $\Gamma(a)$, is determined by Equation (4) and Equation (5) by iterative calculation with Equation (3) using Microsoft Excel. For this sample calculation, assume G_{COND} equals 0.24 kg/m²·s.

Equation (5)

$$a = \frac{G_{COND}}{P_g}\sqrt{\frac{R\,T}{2\,M}} = \frac{0.24\,\frac{kg}{m^2 \cdot s}}{149{,}588Pa}\sqrt{\frac{\left(8.314\,\frac{J}{mol \cdot K}\right)\,(94K)}{2\,\left(0.032\,\frac{kg}{mol}\right)}} = 0.005$$

Equation (4)

$$\Gamma(a) = \exp(-a^2) + a\sqrt{\pi}[1 + \mathrm{erf}(a)] = \exp(-(0.005)^2)(0.005)\sqrt{\pi}[1 + \mathrm{erf}(0.005)]$$

$$\Gamma(a) = 1.0089$$

$$G_{COND} = \left(\frac{0.032\,\frac{kg}{mol}}{2\pi\left(8.314\,\frac{J}{mol \cdot K}\right)94K}\right)^{\frac{1}{2}} [(1.0089)(1)149{,}588Pa - (1)148{,}353Pa]$$

$$\boxed{G_{COND} = 0.24\,\frac{kg}{m^2 \cdot s}}$$

No need to continue with iterations, since condensation mass flux agrees with assumption.

Equation (6)

$$G_{COND} = k_l(T_{sat} - T_s)\sqrt{\frac{\rho_l}{h_{lv}\left[2\,k_l\,(T_{sat} - T_s)\,t + \delta_i^2\,h_{lv}\,\rho_l\right]}}$$

The latent heat (h_{lv}), liquid oxygen density (ρ_l), and thermal conductivity (k_l) are determined by Equation (119), Equation (121), and Equation (122). For the purposes of this sample calculation, the saturated temperature is 94K, with an IRAS heat exchanger surface of temperature of 85K, a liquid height of 12 inches above the heat exchanger, and an elapsed time of 10 seconds.

$$G_{COND} = k_l(T_{sat} - T_s)\sqrt{\frac{\rho_l}{h_{lv}\left[2\,k_l\,(T_{sat} - T_s)\,t + \delta_i^2\,h_{lv}\,\rho_l\right]}}$$

$$G_{COND} = \left(0.1463\frac{W}{m \cdot K}\right)(94K - 85K) \cdot \sqrt{\frac{1122\frac{kg}{m^3}}{\left(209{,}190\frac{J}{kg}\right)\left[2\left(0.1463\frac{W}{m \cdot K}\right)(94K - 85K)(10s) + (0.305m)^2\left(209{,}190\frac{J}{kg}\right)\left(1122\frac{kg}{m^3}\right)\right]}}$$

$$\boxed{G_{COND} = 3.215x10^{-5}\frac{kg}{m^2 \cdot s}}$$

Equation (7)

$$h = k_l\sqrt{\frac{h_{lv}\,\rho_l}{2\,k_l\,(T_{sat} - T_s)\,t + \delta_i^2\,h_{lv}\,\rho_l}}$$

The sample calculation for Equation (6) provides the values for each of the components in Equation (7).

$$h = \left(0.1463 \frac{W}{m \cdot K}\right) \cdot \sqrt{\frac{\left(209{,}190 \frac{J}{kg}\right)\left(1122 \frac{kg}{m^3}\right)}{\left[2\left(0.1463 \frac{W}{m \cdot K}\right)(94K - 85K)(10s) + (0.305m)^2\left(209{,}190 \frac{J}{kg}\right)\left(1122 \frac{kg}{m^3}\right)\right]}}$$

$$\boxed{h = 5.75 \frac{W}{m^2 \cdot s}}$$

Equation (8)

$$D_d = \sqrt[3]{\frac{6\,\sigma\,D_n}{\rho_{lv}\,g}}$$

The sample calculation below uses Equation (124) to estimate the liquid oxygen surface tension. The nozzle diameter is the inner diameter of the liquid oxygen fill tube, which is a 0.500" x 0.049" and downstream of HV-1. The difference between the liquid density and vapor density is obtained from Equation (114) and Equation (115), respectively, at a liquid oxygen temperature of 94K.

$$D_d = \sqrt[3]{\frac{6\left[0.01225 \frac{N}{m}\right][0.010211m]}{\left[1122.2 \frac{kg}{m^3} - 4.273 \frac{kg}{m^3}\right]\left[9.81 \frac{m}{s^2}\right]}}$$

$$\boxed{D_d = 0.00409m}$$

Equation (9)

$$\beta = \left(1 - \frac{3}{\sqrt{\pi}}\,Ja\sqrt{Re_{bo}}\,Pr^{\frac{1}{3}}\,Fo_o\right)^{\frac{2}{3}} = \left(1 - \frac{3}{\sqrt{\pi}}\,\frac{\rho_f c_p (T_{sat} - T_f)}{\rho_g h_{fg}}\sqrt{\frac{\rho_l u_b D_d}{\mu_l}}\,Pr^{\frac{1}{3}}\,\frac{\alpha\,t_r}{D_d^2}\right)^{\frac{2}{3}}$$

The sample calculation below uses Equation (121), Equation (120), Equation (112), Equation (115), Equation (119), and Equation (123) to estimate the liquid density, liquid specific heat capacity, saturation temperature, vapor density, latent heat, liquid viscosity, respectively, evaluated at a temperature of 94K and a pressure of 7 psig. The bubble velocity, u_b, and departure diameter, D_d, are determined by the sample calculations for Equation (8) and Equation (10).

$$Ja = \frac{\rho_f c_p (T_{sat} - T_f)}{\rho_g h_{fg}} = \frac{\left(1122.2 \frac{kg}{m^3}\right)\left(1.705 \frac{kJ}{kg \cdot K}\right)(94.09K - 94K)}{\left(4.273 \frac{kg}{m^3}\right)\left(209.2 \frac{kJ}{kg}\right)} = 0.1291$$

$$Re_{bo} = \frac{\rho_l u_b D_d}{\mu_l} = \frac{\left(1122.2 \frac{kg}{m^3}\right)\left(0.1554 \frac{m}{s}\right)(0.003615m)}{\left(0.000173 \frac{kg}{m \cdot s}\right)} = 4115.8$$

$$Pr = \frac{c_{p,l}\mu_l}{k_l} = \frac{\left(1704.8 \frac{J}{kg \cdot K}\right)\left(0.000173 \frac{kg}{m \cdot s}\right)}{\left(0.1463 \frac{W}{m \cdot K}\right)} = 2.012$$

$$\beta = \left(1 - \frac{3}{\sqrt{\pi}}(0.1291)\sqrt{(4115.8)}\,(2.012)^{\frac{1}{3}}\,\frac{\left(7.645x10^{-8}\frac{m^2}{s}\right)(5.88s)}{(0.003615m)^2}\right)^{\frac{2}{3}}$$

$$\boxed{\beta = 0.65}$$

Equation (10)

$$U_b = \frac{C_z}{1-\alpha}\left(\frac{g\,\sigma\,\rho_{fg}}{\rho_f^2}\right)^{\frac{1}{4}} = \frac{1.53}{1-0}\left(\frac{\left[9.81 \frac{m}{s^2}\right]\left[0.01225 \frac{N}{m}\right]\left[1122.2 \frac{kg}{m^3} - 4.273 \frac{kg}{m^3}\right]}{\left[1122.2 \frac{kg}{m^3}\right]^2}\right)^{\frac{1}{4}} =$$

$$\boxed{U_b = 0.1554 \frac{m}{s}}$$

Equation (11)

$$t_r = \frac{H}{u_b} = \frac{0.9144\text{m}}{0.1554\,\frac{\text{m}}{\text{s}}}$$

Assume H = 36 inches or 0.9144 m and the upward velocity, u_b, is provided by the result of Equation (10) sample calculation.

$$\boxed{t_r = 5.88\text{s}}$$

Equation (13)

$$f_{b,d} = \frac{6\,\dot{m}_{GO_2}}{\pi\,\rho_v\,D_{b,d}^3}$$

Assume the gaseous oxygen mass flow rate is 2 sLm. The oxygen vapor density is estimated by Equation (115) , assuming a vapor temperature of 200 K. Although the oxygen vapor originates in k-bottle at ambient temperature, the oxygen vapor flows through ½" stainless steel tubing through the IRAS dewar to the bottom of the IRAS dewar. As the gaseous oxygen flows through the tubing, the oxygen cools. Sample calculation of gives the value for the bubble departure diameter, $D_{b,d}$.

$$f_{b,d} = \frac{6\,(2\text{ sLm})\left(\frac{0.001326\text{ kg}}{\text{sL}}\right)\left(\frac{\text{min}}{60\text{s}}\right)}{\pi\left(1.955\,\frac{\text{kg}}{\text{m}^3}\right)(0.00409\text{m})^3}$$

$$\boxed{f_{b,d} = \frac{631.24}{\text{s}}}$$

Equation (21)

$$\frac{P}{P_i} = \left[1 + \left(\frac{\gamma-1}{2}\right)\left(\frac{2}{\gamma+1}\right)^{\frac{(\gamma+1)}{2(\gamma-1)}}\sqrt{\frac{\gamma\,g_0 P_i}{\rho_i}}\;\frac{A\,t}{V}\right]^{\frac{-2\gamma}{(\gamma-1)}}$$

Rearrange to solve for the area (A).

$$A = \left(\frac{2}{\gamma - 1}\right)\left(\frac{\gamma + 1}{2}\right)^{\frac{(\gamma+1)}{2(\gamma-1)}} \sqrt{\frac{\rho_i}{\gamma\, g_0\, P_i}}\, \frac{V}{t} \left[\left(\frac{P}{P_i}\right)^{\frac{-(\gamma-1)}{2\gamma}} - 1\right]$$

For IRAS heat exchanger leak check, gaseous helium at an initial pressure of 25.2378 psig (275,333 Pa) decayed to a final pressure of 24.7485 psig (271,959 Pa) in 1,110 seconds. The specific heat ratio of helium is 1.67 and the initial density of gaseous helium is 2.226 kg/m³. The gaseous helium occupies approximately 0.000445 m³ inside the IRAS heat exchanger.

$$A = \left(\frac{2}{1.67 - 1}\right)\left(\frac{1.67 + 1}{2}\right)^{\frac{(1.67+1)}{2(1.67-1)}} \sqrt{\frac{2.226\frac{kg}{m^3}}{1.67(275{,}333Pa)}}\, \frac{4.45x10^{-4}m^3}{1110\ s} \left[\left(\frac{271{,}959Pa}{275{,}333Pa}\right)^{\frac{-(1.67-1)}{2(1.67)}} - 1\right]$$

$$\boxed{A = 5.43x10^{-12}m^2}$$

Equation (22)

$$\frac{P}{P_i} = \exp\left[-\left(\frac{\gamma - 1}{2}\right)\left(\frac{2}{\gamma + 1}\right)^{\frac{(\gamma+1)}{2(\gamma-1)}} \sqrt{\frac{\gamma\, g_0 P_i}{\rho_i}}\ \frac{A\, t}{V}\right]$$

Rearrange to solve for area (A).

$$A = -\left(\frac{2}{\gamma - 1}\right)\left(\frac{\gamma + 1}{2}\right)^{\frac{(\gamma+1)}{2(\gamma-1)}} \sqrt{\frac{\rho_i}{\gamma\, g_0\, P_i}}\, \frac{V}{t}\ \ln\left(\frac{P}{P_i}\right)$$

$$A = -\left(\frac{2}{1.67 - 1}\right)\left(\frac{1.67 + 1}{2}\right)^{\frac{(1.67+1)}{2(1.67-1)}} \sqrt{\frac{2.226\frac{kg}{m^3}}{1.67(275{,}333Pa)}}\, \frac{4.45x10^{-4}m^3}{1110\ s}\ \ln\left[\frac{271{,}959Pa}{275{,}333Pa}\right]$$

$$\boxed{A = 2.70x10^{-11}m^2}$$

Equation (23)

$$\dot{m} = C_D\, A \sqrt{2\, \Delta P\, \rho\, g_c}$$

The below sample calculation uses the Isentropic Blowdown area result from Equation (21) the liquid nitrogen mass flow rate through the leak. From orifice flow calculations, C_D ranges from

a minimum of 0.54 to a maximum of unity [29], thus, the below sample calculation uses C_D equal to 1.00 to represent a maximum liquid nitrogen flowing through the leak in place of an uncertain C_D. The pressure difference (ΔP) is from the pressure of the liquid nitrogen flowing through the IRAS heat exchanger at 45 psia (411,588Paa) to the pressure within the IRAS dewar of 3 psia (122,588 Paa). The density of the liquid nitrogen is estimated from Equation (128) at a temperature of 80K.

$$\dot{m} = (1.00)\,(5.43\text{x}10^{-12}\text{m}^2)\sqrt{2\,(411{,}588\,\cancel{\text{Pa}} - 122{,}010\,\cancel{\text{Pa}})\left(796.23\,\frac{\text{kg}}{\text{m}^3}\right)\left(\frac{\frac{\cancel{\text{N}}}{\text{m}^2}}{\cancel{\text{Pa}}}\right)\left(\frac{\text{kg}\,\frac{\text{m}}{\text{s}^2}}{\cancel{\text{N}}}\right)}$$

$$\boxed{\dot{m} = 1.40\text{x}10^{-7}\,\frac{\text{kg}}{\text{s}} = 0.0072\text{sLm}}$$

Equation (24)

$$Q_{EVAP} = \dot{m}\left[\int_{T_i}^{T_{BP}} c_{P,L}dT + h_{LV} + \int_{T_{BP}}^{T_f} c_{P,V}dT\right]$$

From Equation (127), $h_{LV}(T) = h_{LV}(77.3\text{K}) = 85.44\,\frac{\text{J}}{\text{g}}$

From Equation (126),

$$\int_{T_{BP}}^{T_f} c_{P,V}dT = \int_{77.3\text{K}}^{160\text{K}} R\left[\frac{N_1}{T^3} + \frac{N_2}{T^2} + \frac{N_3}{T} + N_4 + N_5T + N_6T^2 + N_7T^3 + \frac{N_8\left(\frac{N_9}{T}\right)^2 e^{\frac{N_9}{T}}}{\left(e^{\frac{N_9}{T}} - 1\right)^2}\right]dT$$

$$= R\left[-\frac{N_1}{4T^4} - \frac{N_2}{3T^3} + N_3\ln T + N_4T + \frac{N_5T^2}{2} + \frac{N_6T^3}{3} + \frac{N_7T^4}{4} + \frac{N_8N_9}{\left(e^{\frac{N_9}{T}} - 1\right)}\right]$$

$$= 85.79\,\frac{\text{J}}{\text{g}}$$

$$Q_{EVAP} = \dot{m}\left[\int_{T_i}^{T_{BP}} c_{P,L}dT + h_{LV} + \int_{T_{BP}}^{T_f} c_{P,V}dT\right] = \dot{m}\left[h_{LV} + \int_{T_{BP}}^{T_f} c_{P,V}dT\right]$$

$$= \dot{m}\left[h_{LV} + \int_{T_{BP}}^{T_f} c_{P,V}dT\right] = 5.3\text{sLm}\left(\frac{1.1614\text{ g}}{\text{sL}}\right)\left(\frac{\text{min}}{60\text{s}}\right)\left[85.44\,\frac{\text{J}}{\text{g}} + 85.79\,\frac{\text{J}}{\text{g}}\right]$$

$$\boxed{Q_{EVAP} = 17.57\text{W}}$$

REFERENCES

[1] Thomas M. Flynn, Cryogenic Engineering, Marcel Dekker, New York, NY, 2005.

[2] Jerry Jon Sellers, Williams J. Astore, et al., Understanding Space, McGraw-Hill, Boston, MA, 2004.

[3] Pratt & Whitney Press Releases, Renowned Rocket Engine Celebrates 40 Years of Flight, Accessed: August 2, 2010, Published: November 24, 2003, http://www.pratt-whitney.com/vgn-ext-templating/v/index.jsp?vgnextoid=cabbe002c2f3c010VgnVCM1000000881000aRCRD&vgnextchannel=7dfc34890cb06110VgnVCM1000004601000aRCRD&vgnextfmt=default.

[4] Frank G. Kerry, Industrial Gas Handbook: Gas Separation and Purification, CRC Press, Boca Raton. FL, 2007.

[5] Conceptual Design of a Lunar Oxygen Pilot Plant, NASA Contract Number NA9-17878 EEI Report 88-182, NASA Johnson Space Center, Houston, TX, 1988.

[6] L.J. Hastings, D. W. Plachta, et al., An Overview of NASA Efforts on Zero Boiloff of Cryogenic Propellants, Cryogenics () (2002) 833-839.

[7] Charles Panzarella, David Plachta, et al., Pressure Control of Large Cryogenic Tanks in Microgravity, Cryogenics (2004) 475-483.

[8] R. Hendricks, Paramagnetic Propellant Orientation, AIAA-91-2325, AIAA, Washington, D.C., 1991.

[9] Reduction of Liquid Hydrogen Boiloff Reliquefaction Cycle Analysis (MCR-76-229), Final Report, Martin Marietta, Denver, CO, 1976.

[10] Reduction of Liquid Hydrogen Boiloff: Optimal Reliquefaction System Design and Cost Study (MCR-77-136), Final Report, Martin Marietta, Denver, CO, 1978.

[11] J. R. Feller, Study of Large-Scale Zero Boil-Off Options for Launch Pad Storage of Cryogenic Propellants, Final Report, NASA-Ames Research Center, Moffet Field, CA, 2006.

[12] D.W. Plachta, R.J. Christie, et al., Passive ZBO Storage of Liquid Hydrogen and Liquid Oxygen Applied to Space Science Mission Concepts, Cryogenics (2006) 89-97.

[13] NASA, The James Webb Space Telescope, Accessed: June 7, 2010, Published: http://www.jwst.nasa.gov/observatory.html.

[14] R.G. Ross Jr., R. F. Boyle, An Overview of NASA Space Cryocooler Programs - 2006, International Cryocooler Conference, Annapolis, MD, 2006.

[15] Thomas M. Tomsik, Performance Tests of a Liquid Hydrogen Propellant Densification Ground Support System for the X33/RLV, AIAA (1997) 2976-2992.

[16] T.I. Lak, M.E. Lozano, et al., Propellant Densification Without Use of Rotating Machinery, AIAA (2002) 3599-3608.

[17] M. M. Fazah, STS Propellant Densification Feasibility Study Data Book, NASA Technical Memorandum 108467, NASA, Marshall Space Flight Center, AL, 1994.

[18] Frank P. Incropera, David P. Dewitt, Fundamentals of Heat and Mass Transfer, John Wiley & Sons, Hoboken, NJ, 2002.

[19] John G. Collier, Convective Boiling and Condensation, McGraw-Hill, Maidenhead, England, 1981.

[20] Y.M Chen, F. Mayinger, Measurement of Heat Transfer at the Phase Interface of Condensing Bubbles, International Journal of Multiphase Flow (1992) 877-890.

[21] Jerrold Isenberg, David Moalem, et al., Direct Contact Heat Transfer with Change of Phase: Bubble Collapse with Translatory Motion in Single and Two Component Systems, International Journal of Heat Transfer (1970) 997-1011.

[22] Y. Lerner, H. Kalman, et al., Condensation of an Accelerating-Decelerating Bubble: Experimental and Phenomenological Analysis, Journal of Heat Transfer (1987) 509-517.

[23] O. Zeitoun, M. Shoukri, et al., Interfacial Heat Transfer Between Steam Bubbles and Subcooled Water in Vertical Upward Flow, Journal of Heat Transfer (1995) 402-407.

[24] William U. Notardonato, Wesley L. Johnson, et al., Experimental Results of Integrated Refrigeration and Storage System Testing, in: Advances in Cryogenic Engineering, American Institute of Physics, Melville, NY, 2009, pp. 1369-1376.

[25] William U. Notardonato, Wesley L. Johnson, et al.,Integrated Refrigeration and Storage System - Heat Exchanger Characterization, Final Report, NASA, Kennedy Space Center, 2009.

[26] Fredrick J. Moody, Introduction to Unsteady Thermofluid Mechanics, John Wiley & Sons, Inc., New York, 1990.

[27] Micheal R. Lindeburg, Mechanical Engineering Reference Manual, Ninth Edition, Professional Publications, Inc., Belmont, CA, 1995, pp. 3-22 - 3-23.

[28] Van P. Carey, Boiling and Condensation Heat Transfer, Taylor & Francis Group, New York, NY, 2008.

[29] Warren M. Rohsenow, James P. Hartnett, et al., Handbook of Heat Transfer, Third Edition, McGraw-Hill, New York, 1998, pp. 14.26-14.27, 14.44-14.45.

[30] Dennis G. Zill, Michael R. Cullen, Differential Equations with Boundary-Value Problems, Brooks/Cole, Pacific Grove, CA, 2001, pp. 527-551.

[31] L.A. Weber, Thermodynamic and Related Properties of Oxygen from the Triple Point to 300K at Pressures to 1000 Bar, NASA Reference Publication 1011, National Bureau of Standards, Boulder, CO, 1977.

[32] Randall F. Barron, Cryogenic Systems, 2nd Edition, Oxford University Press, Oxford, 1985.

[33] R.T. Jacobsen, R.B. Stewart, Thermophysical Properties of Nitrogen From The Fusion Line To 3500 R For Pressures To 150,000 PSIA, NBS Technical Note 648, National Bureau of Standards, Boulder, Colorado, 1973.